WHISPERING-GALLERY MODES IN QUANTUM DOT EMBEDDED MICROSPHERES FOR SENSING APPLICATIONS

A Dissertation

by

HOPE THOMAS BEIER

Submitted to the Office of Graduate Studies of
Texas A&M University
in partial fulfillment of the requirements for the degree of

DOCTOR OF PHILOSOPHY

December 2009

Major Subject: Biomedical Engineering

WHISPERING-GALLERY MODES IN QUANTUM DOT EMBEDDED MICROSPHERES FOR SENSING APPLICATIONS

A Dissertation

by

HOPE THOMAS BEIER

Submitted to the Office of Graduate Studies of
Texas A&M University
in partial fulfillment of the requirements for the degree of

DOCTOR OF PHILOSOPHY

Approved by:

Co-Chairs of Committee,	Kenith E. Meissner
	Gerard L. Coté
Committee Members,	Michael J. McShane
	Michael V. Pishko
Head of Department,	Gerard L. Coté

December 2009

Major Subject: Biomedical Engineering

ABSTRACT

Whispering-Gallery Modes in Quantum Dot Embedded Microspheres for Sensing Applications. (December 2009)

Hope Thomas Beier, B.S., Texas A&M University

Co-Chairs of Advisory Committee: Dr. Kenith E. Meissner
Dr. Gerard L. Coté

New methods of biological analyte sensing are needed for development of miniature biosensors that are highly sensitive and require minimal sample preparation. One novel technique employs optical resonances known as Whispering Gallery Modes (WGMs). These modes arise from total internal reflection of light at the internal surface of a high index microsphere within a low index medium and produce an evanescent field that extends into the surrounding medium. The WGMs produce multiple narrow spectral peaks that shift position with variations in the local index of refraction sampled by the evanescent tail of the WGMs.

To excite these WGMs, we embed quantum dots (QDs) in the periphery of polystyrene microspheres to serve as local light sources. By coupling emission from the QDs to the WGMs, the sensors can be excited and interrogated remotely and, by monitoring the shift of multiple resonance modes, may provide higher sensitivity and accuracy compared with similar techniques. The high refractometric sensitivity of the WGMs offers potential for trace detection of molecules adsorbed onto or bound to the microsphere sensor elements.

The sensitivity of these sensors is demonstrated by monitoring the wavelength shift of multiple resonant modes as bulk index of refraction is changed. The potential for targeted biosensing is explored through addition of a protein that adsorbs to the microsphere surface, thrombin. Microsensor response in all cases demonstrated increased sensitivity over theoretical predictions. Models based on Mie theory and continuity of the radial functions across the sphere-media interface were used to model the location, Q-factor, and sensitivity of the WGMs in microspheres by considering the embedded QDs as a high index outer layer. This model was used, along with estimates of the QD-layer index and penetration depth, to relate the locations and sensitivities of the modes to our experimental results with strong agreement between the two. In all, these microspheres demonstrate feasibility for use as remote microsensors with sensitivities rivaling current techniques.

DEDICATION

To my husband, Eric.

ACKNOWLEDGEMENTS

This dissertation would not have been possible without Dr. Kenith Meissner. I would like to thank you for allowing me to work with you on this project; I could not have asked for a better advisor. Thank you for always having an open door, no matter how busy you were, and allowing me to explore ideas, seek advice, or simply gain a new perspective. Your insight, energy and enthusiasm are inspiring; I hope that someday I may have the same impact on others that you had on me. I would like to show my appreciation to Dr. Gerard Coté for keeping me relatively well funded when my fellowships ran out, providing me with a place to work and allowing me to explore a variety of projects to gain a diverse set of skills. I am grateful for the multiple opportunities to present my research and discover other research in our field. I would also like to thank Dr. Mike McShane and Dr. Michael Pishko for serving on my committee and helping me with various projects throughout the years.

I would like to thank Bennett Ibey for our endless conversations, candid advice and allowing me to voice my frustrations. Thank you for your continued emotional support and for being an amazing friend over the past six years. I would like to thank my numerous labmates, Becky Gant in particular, for your help and support throughout graduate school and the interesting lunchtime conversations. I would also like to express my appreciation to the National Science Foundation for their fellowship support.

Thank you to my sister Rachel and brother-in-law Robert for your personal support and to my nephew and niece, Riley and Reagan, for the joy you bring. Most

importantly, I would like to thank my husband Eric for always being there for me. Even after 10 years, I find myself growing more fond of you everyday. I cannot wait to see what the future will bring.

TABLE OF CONTENTS

CHAPTER Page

CHAPTER Page

Page

LIST OF TABLES

LIST OF FIGURES

FIGURE Page

LIST OF SYMBOLS

SYMBOL	
a	Radius (of the microsphere)
a_l	Mie Coefficient (TM)
A_l, B_l, C_l, D_l,	Resonance Coefficients
b_l	Mie Coefficient (TE)
$\chi_l(mkr)$	Ricatti-Neumann Function
E	Electric Field
i	Radial Mode Order
j	Imaginary Number
j_l	Spherical Bessel Function
k	Wavevector
l	Angular Mode Number
λ	Wavelength (in vacuum)
m(r)	Refractive Index (as a function of radius)
m	Relative Refractive Index (m_1/m_2)
m_1	Refractive Index of the Microsphere
m_2	Refractive Index of the Medium
m_3	Refractive Index of the Layer
$\mathbf{M}_{l,i}$	TE Electric Field
$\mathbf{N}_{l,i}$	TM Electric Field
n_l	Spherical Neumann Function

SYMBOL	
ω	Angular Frequency
$\psi_l(mkr)$	Ricatti-Bessel Function
Q	Quality Factor (Q-factor)
r	Radius (varying)
$S_l(r,k)$	TE Scalar Radial Function
t	Layer Thickness
$T_l(r,k)$	TM Scalar Radial Function
τ	Average Recirculation Time
x	Dimensionless Size Parameter

CHAPTER I

INTRODUCTION

Motivation

Recent advances in biomedical technology have necessitated development of biosensors that are highly sensitive and require minimal sample preparation. A growing number of biomarkers have been indentified for specific disease states enabling screening technologies for early diagnosis.[1-3] Additionally, drug discovery,[4] point-of-care monitoring,[5] and rapid detection of possible biological or environmental threats,[2] require incredibly sensitive methods of analyte sensing. Ideally, these methods should be label-free, work with small sample volumes, and possess multiplexing capabilities.

Optical Sensors

Typically, optical biosensors come in two forms: fluorescent and label-free.[1, 6-8] In fluorescent biosensors the target analyte or biorecognition molecule is labeled with a fluorophore. The intensity of a fluorescent signal provides a means to detect the presence of the analyte. Although the signal may be very sensitive, it suffers from the labeling procedure, which may require labeling ratios that are difficult to control.

This dissertation follows the style of Journal of the Optical Society of America B.

Additionally, these methods often detect changes in fluorescence lifetime or intensity, which may suffer from high fluorescence background from the unperturbed targets. Finally, the intensity of the fluorescent signal is often dependent on the number of analytes, potentially limiting the minimum detectable signal.

In contrast, label-free methods are typically based on a refractive index change induced by the target molecule interacting with the sensor. These signals are often dependent on the sample concentration or density on the surface of the sensor, thus, detection limit may be decreased with decreased sensor size. Label-free methods allow the analyte to be detected rapidly without chemical modification.[6] Common forms of label-free detection refractive index techniques include surface plasmon resonance (SPR), waveguide, interferometric, and optical resonator techniques.[6, 9-11]

Surface Plasmon Resonance Sensing

In SPR sensing, as demonstrated in Figure 1.1, light is internally reflected at the interface of a dielectric material and a thin metal surface.[12-15] The total internal reflection generates an evanescent field in the metal film that becomes resonant with the surface plasmons along the metal surface at certain angles or wavelengths. This resonance is sensitive to the local index of the medium on the outside of the metal surface and is seen as a dip in the reflected intensity at a specific wavelength (if the incident angle remains fixed) or at a specific angle (if monochromatic light is used and the incident angle is varied). SPR sensors have been commercialized and may obtain

sensitivities up to 10^{-6} to 10^{-7} RIU or 1 pg/mm^2 of analyte.[6, 9, 14] Signals have been obtained from areas as small as 0.02 mm^2 with a reported sensitivity of ~500 fg.[16] Localized SPR (LSPR) sensing approaches in which the plasmon originates from a metal nanoparticle have been shown to have refractive index sensitivities of ~200 nm/RIU; however the linewidth is ~50 nm.[17] Detection with SPR is based on the interaction of the evanescent field with the surrounding solution on only one occurrence, thus limiting the sensitivity.

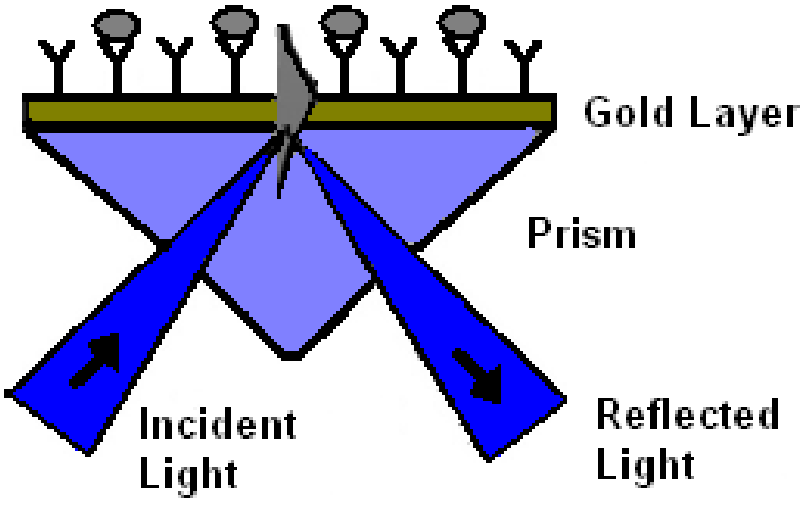

Figure 1.1: Surface Plasmon Resonance Sensor Set-up (adapted from Hoa, X.D, et al.[12]).

Interferometric Sensing Techniques

In typical interferometric techniques, as demonstrated in Figure 1.2, coherent light is split among two branches in a waveguide.[6] One arm remains protected to serve as a reference, while the other is allowed to interact evanescently with the sample. For a Mach-Zehndel interferometer, the two arms are recombined to produce an interference between the two signal and the intensity is detected.[18-20] In Young's interferometers the two signals produce an interference pattern on a detector such as a CCD array and the spacing between the interference fringes is measured.[21, 22] Interferometric-based sensing may also be achieved by focusing a coherent laser onto a sensing area and detecting the reflected light for an intensity change or shift in the interference signal.[23] These methods have been demonstrated to provide very sensitive detection of biomolecules, to 10^{-7} RIU and 20 pg/mm^2.[6, 22, 24] Like SPR, the detection is based on the interaction of the evanescent field with the surrounding solution on only one occurrence, but may be improved by increasing the sample interaction length.[25] Thus, the total mass sensitivity is limited by the length of the waveguide exposed to the sample. While the sensitivity per area was shown to be 20 pg/mm^2, the exposed portion of the waveguide was 2 µm wide by 15 mm long, producing a total mass sensitivity of only 600 fg.[24]

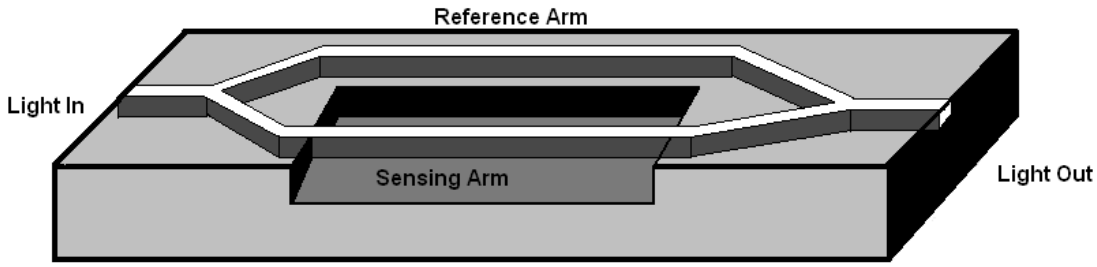

Figure 1.2: Typical Interferometric Biosensor (adapted from Fan, X.D. et al.[6]).

Whispering Gallery Mode Sensors

Whispering Gallery Modes (WGMs), as demonstrated in Figure 1.3, arise from the confinement of light within a ring resonator or microsphere due to total internal reflection of light at its internal surface, creating resonances at specific wavelengths.[26, 27] The WGMs produce narrow spectral peaks with evanescent tails that extend into the medium surrounding the resonator and shift position due to changes in the surrounding index, or addition of molecules adsorbed onto or bound to the sensor elements. WGM based sensors improve upon the sampling ability by allowing the light in the resonator to be recirculated many times; thus increasing the total sampling distance without increasing the sensor size. In these systems, the light is typically coupled to the WGM through evanescent waves from the side of an eroded optical fiber or the end of an angle polished fiber.[28-33] For remote sensing, dye-doped microspheres may be used.[34, 35] Here, emission from the dye in the outer portion of the microsphere couples to the WGMs.

However, organic dyes are highly susceptible to photobleaching and thus limit the usefulness of this sensor design when continuous or repeated interrogation of the sensor is required.

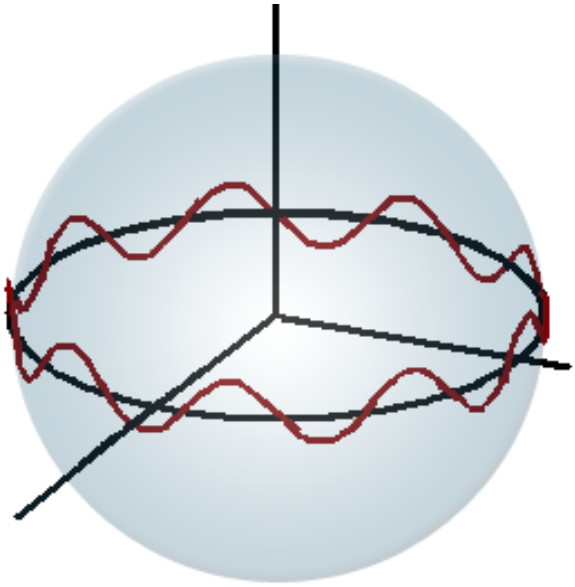

Figure 1.3: WGM in a Microsphere (adapted from Arnold, S. et al.[36]).

Quantum Dots

Due to their unique optical properties, quantum dots are an excellent choice for a local light source to mitigate the photobleaching problem observed with dye-doped microspheres. QDs are colloidal semiconductor nanocrystals in which the electron-hole

pair is confined in all three spatial dimensions. QDs are characterized by the following properties:[37]

(i) High quantum yield. Relatively low excitation powers may achieve a detectable signal; thus allowing for a broader excitation area (lower focusing power) for excitation of multiple spheres simultaneously.

(ii) Resistance to photobleaching. Spheres may be excited for longer or more continuous periods; thus increasing the viable lifetime of the sensors.

(iii) Relatively narrow emission spectrum that is dependent on particle size. This feature allows the particles to be size-tuned through the visible and into the near infrared.

(iv) Broad absorption spectrum that extends into the UV. This absorption spectrum allows the excitation source to be spectrally separated from the emission wavelength, creating a large effective Stoke's shift and simplifying detection.

(v) Ideal characteristics for spectral multiplexing applications. The tunability of the emission and the broad absorption spectrum are ideal for exciting multiple QD populations with a single excitation source and identifying the individual populations based on their emission wavelength.

My Approach for WGM-Based Sensing

As a solution to the biosensor challenge, I have developed QD-embedded polystyrene microspheres as microscale WGM biosensors for remote detection of

bioanalytes. By coupling emission from the QDs in or on the microsphere to the WGMs, the sensors can be excited and interrogated remotely. The optical system for these microspheres will rely on remote, free space coupling of excitation and emission light; thus enabling remote operation in turbid media and facilitate the simultaneous use of multiple microspheres with a single excitation source. Following excitation, luminescence from the QDs couples to multiple narrow WGM peaks across the relatively broad luminescence spectrum of the local light sources. Thus, multiple modes may be monitored simultaneously, potentially improving sensitivity and accuracy. The WGM scheme observes the shifts in the peaks, meaning it is not as susceptible to changes in optical pathlength or delivered power when compared to intensity-based techniques. By using QDs as the sources of luminescence, the sensors are less susceptible to photobleaching than dye-based sources. Thus, the overall useful lifetime of the sensor is extended and the possibility for continuous measurements is improved, increasing the viability of real-time measurements.

These microspheres will be label-free, meaning that binding of the analyte of interest to specific surface chemistry is directly detected. Each WGM sensor will be designed for specific analytes of interest and functionalized with capture agents for those analytes. Thus, analyte detection can be performed rapidly by using microspheres pre-functionalized for the analyte of interest with little pre-processing of the biological media before exposure to the microsensors. The sensors should be capable of being regenerated for repeated or reversible use. Assuming the binding events, such as antigen-

antibody are competitive and reversible, the analytes can be removed from the system via a series of washing steps to reuse the sensors.

The sensors are also very small (~10 μm), limiting the amount of required sample volume and increasing the ability to use multiple sensors over a limited area. The small area may also improve sensitivity; the wavelength shift due to adsorbed proteins has been shown to display a 1/R dependence on microsphere radius, thus increasing the mass sensitivity with smaller size.[35, 38] Since these sensors are small, only the first radial order WGM peaks are visible. The lack of a complex WGM structure allows for easier identification of specific peaks, especially after shifting.

Conclusion

This dissertation will focus on the development of these WGM-presenting microspheres for biosensing applications. Previous formulations of WGM-based biosensors will be discussed in Chapter II, followed by a general discussion of the WGM resonance theory in Chapter III. Following a methods section in Chapter IV, the use of continuous wave excitation and the characteristics of the experimental WGMs sensors will be explored in Chapter V. Chapter VI will describe WGM theory involving both shape resonances and Mie scattering to theoretically explain our experimental results and provide a basis for modeling the sensitivity of the WGM sensors. Finally, biological sensing will be examined through the detection of protein adsorption and targeted detection of myoglobin.

CHAPTER II

WHISPERING GALLERY MODE BASED SENSING

Introduction

The narrow resonance structure provided by microsphere WGMs offers an excellent platform for sensor development. The high refractometric sensitivity of the WGMs offers potential for trace detection of molecules adsorbed onto or bound to the microsphere sensor elements. Unlike other refractometric approaches, the interaction length between the light and the analytes is not determined by the sensor size but by the total time that the light remains resonant in the cavity. Because the light circulates in the sensor multiple times, it may react with the same analyte on multiple occasions, increasing the potential for single molecule or very low mass detection. Sensor configurations for WGM-based sensor development have included micro-fabricated sensors in the form of micro-rings, micro-disks, and micro-toroids, capillary-based ring resonators and microspheres.

Micro-Fabricated Resonators

Arrays of optical resonators such as micro-toroids, [39, 40] micro-rings, [41-47] and micro-disks[48-50] have been demonstrated for sensing applications. These devices often use the same photolithographic techniques developed for the manufacture of integrated

circuits. Planar polymer resonators may be created using nanoimprinting by creating a silicon mold of the micro-ring and imprinting it into a thin polymer, such as polystyrene, film.[41] Glass micro-rings may be manufactured by vapor-deposition of the glass material.[44] Waveguides or optical fibers are coupled to the resonators either vertically, where the waveguides are buried beneath the resonator, or laterally, where the waveguides are coplanar with the resonators.[44] These sensors are advantageous in that arrays of the devices may be mass produced with many sensor elements on a single chip for low cost and that the optical coupling may be integrated into the design.[6] However, these devices must be mounted to separate fluidics for most biosensing applications and typically have lower Q-factors than other approaches, due to the roughness of the manufactured surface. These micro-fabricated sensors have been used successfully for refractive index,[44] deuterium oxide,[40] protein,[44, 46] bacteria[47] and nucleic acid detection.[47]

Capillary-Based Resonators

Capillary-based opto-fluidic ring resonators, also known as liquid-core optical ring resonators (LCORR), have also been demonstrated for WGM sensing applications. Capillary tubes are pulled under heat to produce tubes with micrometer thick walls and diameters of 50 – 100 μm. Light from a tunable laser diode is coupled into the sensor from a stripped single mode fiber place in contact with the outside of the tube. Transmission through the fiber is monitored for dips in the intensity, indicative of WGMs. Analyte solutions may be flowed through the capillary to interact with the

evanescent field inside the tube. This design allows for simultaneous use of the capillary tubes as microfluidic channels and sensor elements; however the sensitivity may be somewhat less than spherical resonators. These sensors have been used for refractive index sensing, with a sensitivity of ~3-15 nm/RIU (refractive index units),[51-53] and for proteins (BSA) with a sensitivity of ~0.5-30 pg/mm^2.[52, 54] DNA,[55] viruses,[56, 57] and chemical vapors[58-60] have also be detected. These sensors can be multiplexed by coupling the resonators to multiple waveguides[52, 61] and can be used for capillary electrophoresis devices.[62]

Evanescently-Coupled Microspherical WGM Sensors

WGM-based sensors using microspherical cavities typically have larger Q-factors than other approaches due to the high surface tension of the microsphere surface; however, refractive index sensitivity has been somewhat limited by their relatively large size. Initial investigations into WGM-based sensors used "bare" microspherical cavities in which a spectrally scanned optical source probed the WGM structure.[31, 63] Generally, microspheres with a diameter of 100 μm or larger are used as the resonant cavity to provide a high Q-factor for sensitivity to spectral shift. Due to the narrow mode structure, the source must have a narrow linewidth to differentiate modes and interrogates a single WGM. In these systems, the light is coupled to the WGM through evanescent waves from the side of an eroded optical fiber[31] or the end of an angle polished fiber.[63]

Protein Detection with Silica Microspheres

Protein sensing using spherical WGM-based sensors was first demonstrated by Vollmer, et al. in 2002.[31] A ~150 μm radius silica microsphere, made by melting the end of a single mode fiber, was coupled to an eroded optical fiber for excitation. A laser diode with an emission of ~1340 nm was current scanned to shift the wavelength. The light transmitted through the optical fiber was monitored for dips in the intensity, indicative of resonant modes. A shift in the position of these modes of ~20 pm was observed with the addition of biotinylated BSA and then again with the subsequent addition of streptavidin. These protein results were then compared to a perturbation theory to model the empirical data and calculate the size dependence of the microsphere on the sensitivity.[36] The model was shown to fit the experimental data well and allow for the calculation of the surface density and thickness of the protein layer. The experimental approach and model were then further extended to investigate the dependence of protein molecular weight on the shift of the WGMs.[64] Shifts of proteins ranging from 5 to 700 kDa were monitored and it was discovered that the sensitivity had a dependence of $MW^{1/3}$. Differences in WGM shifts for both TE and TM modes due to the adsorption of BSA were also observed by changing the polarization of the light in the excitation fiber.[65] The angle of the laser mount in relation to the single mode excitation fiber was adjusted to produce vertical polarization to excite the tangentially polarized TE modes in the microsphere. The laser mount was then rotated to produce horizontal polarization to excite the radially polarized TM modes. A difference in shifts between

the two polarizations was observed and confirmed with the addition of NaCl to change the bulk index surrounding the microspheres.

Additional Sensing with Silica Microspheres

Multiplexed DNA detection was demonstrated using two microspheres with detection limits of ~6 pg/mm.[30] Microspheres, fabricated from the end of an optical fiber, were coated in dextran-biotin to form a hydrogel then functionalized with streptavidin-couple biotinylated oligonucleotides. Two microspheres, with different oligonucleotide sequences, were coupled to the same optical fiber and identified by their specific resonances. Two hybridization events could then be monitored simultaneously.

Ren et al. demonstrated theoretical and experimental detection of rod-shaped bacteria.[66] A ~340 μm diameter fiber was exposed to a bacteria solution. Microscope images were used to determine the number of bound bacteria and were compared to the WGM resonances before and after exposure. Minimum sensitivity was determined to be 44 bacteria or 34 pg/mm^2.

Temperature detection was demonstrated using the ~100 μm silica microspheres in both water and air.[67] Increasing the temperature of the silica microspheres produces an increase in both the microsphere radius and refractive index that results in a shift in the resonance positions. This shift was used to calculate the temperature surrounding the microspheres, which was shown to follow the temperature changes measured by a thermistor or a thermocouple to within 1^{o}C in air.

Particles undergoing Brownian motion near microspheres were also examined using ~200 μm silica microspheres in buffer solutions containing nanometer sized polystyrene microspheres.[68] The noise in the WGM signal of the solutions containing the particle and filter buffer were compared to produce an autocorrelation function. This function was compared with diffusion theory to estimate the particle size. Good agreement was demonstrated for small particles (37 nm) with a decrease in accuracy as the particle size increased.

Specific virus detection was demonstrated by functionalizing the silica microspheres with antibodies specific to a target virus.[69] Detection of the target virus was demonstrated and non-specific binding of a negative control virus was found; however, the non-specific virus was removed with a PBS rinse. Single virus detection was also demonstrated for silica microspheres.[70] Microspheres from the melted ends of optical fibers ranging in size from 44 to 105 μm in radius were exposed to 250 nm radius polystyrene particles to determine the optimum sensor size. Sensitivity was shown to scale with radius by a factor of $R^{-2.67}$. Virions with an average radius of ~50 nm were allowed to adsorb to a 39 μm microsphere excited at 763 nm. Steps in the WGM resonance, related to single binding events, were observed.

Microsphere Sensors with Prism Coupling

Refractive index sensitivity by a fused silica microsphere was demonstrated by Hanumegowda et. al in 2005.[71] Like the silica WGM sensors made by Arnold's group,

the silica microsphere was made by melting the end of an optical fiber. However, instead of evanescent coupling from an eroded optical fiber, light was coupled into the microsphere at the end of an angle-polished fiber prism, and the reflected light was monitored for dips in the intensity, indicative of the resonances. Sensitivity of these microspheres was ~30 nm/RIU (refractive index units) for a detection limit of 10^{-7} RIU. Small molecule detection was then demonstrated for these microspheres by monitoring the shift of the WGMs due to removal of silica molecules by etching the microsphere with hydrofluoric acid.[32] This etching approach was also shown to be capable of tuning the location of the WGMs with only negligible degradation of the Q-factors due to surface roughness.[72]

Biosensing was employed by this group for the detection of the protease, trypsin.[29] The microsphere sensors used in the previous work were coated with BSA and the shift in the WGM resonance due to the cleavage of the BSA by trypsin was used as a measure of the proteolytic activity. Heavy metal detection was further shown through the specific detection of mercuric ions in water.[28] Protein sensing and the feasibility of using aptamers was also demonstrated by functionalizing the microspheres with aptamers specific to thrombin.[33]

Theoretical Investigations

Theoretical work has used a first-order perturbation theory to describe microsphere sensitivity in response to bulk refractive index changes, adsorption of small

particles and refractive index depletion near the sensor surface.[73] This theory has been extended for both TE and TM modes to describe the differences in the shift of the two polarizations for single and packed layers of spherical and cylindrical particles.[74] The ratio between the shifts may be used to gain information about the shape of the absorbed particles. A dipolar approximation was then used to describe the interaction between spherical particles adsorbed on a surface as a function of the packing density and to relate this interaction to the shift of the WGMs.[75] The work was then extended for the TM to TE shift ratios to obtain values for the expected shifts for several different geometries and orientations of particles of low density on a surface.[65] Shifts of TM and TE modes in conjunction were further examined to theoretically estimate the surface density and orientation of adsorbing anisotropic molecules.[76]

Addition of a High Index Layer

Teraoka and Arnold have theoretically demonstrated the ability to increase the WGM mode sensitivity by coating a microsphere with a thin layer of a high refractive index material.[77] This layer moves the field of the WGM closer to the surface of the microspheres, exposing more energy to the outside. The theory was expanded for TM modes, which were found to potentially display higher sensitivity than the TE modes.[78] It was also demonstrated that, with specific layer thicknesses and refractive indices, the TE and TM shifts due to perturbations could be equal and that the positions of the resonances could possibly overlap.

The high refractive index layer theory was demonstrated empirically by the group Gaathon et al. An ~8 fold enhancement in the refractive index sensitivity of a ~200 μm fluorine doped silica microsphere (m=1.43) was obtained by coating the resonator with a 340 nm polystyrene layer (m=1.58).[79] This work was then expanded theoretically for a three-layer system.[80] By placing a low refractive index layer between two high index layers, two separate modes, each centered on one of the high index layers, were shown to appear.

Remotely Excited and Interrogated Microspheres

Thus far, the WGM-based microsphere sensors have been excited by evanescently coupling light from a tuned laser diode into the microsphere from an optical fiber or prism. This approach obtains WGMs with high Q-factors and resolution limited to the tuning range of the laser diode. However, remote excitation and interrogation are precluded, and precise coupling of the sensor to the excitation source is required, which may be difficult. If the WGMs are excited from local light sources, such as fluorophores or QDs on the surface or embedded within the actual microspheres, remote operation is feasible. Additionally, since the luminescence from the fluorophores or QDs is significantly broader than the free-spectral range and linewidth of the WGMs, multiple WGM peaks with both TE and TM polarizations may be excited and detected simultaneously.

WGMs in Dye-Doped Microspheres

One approach for remote WGM sensing uses dye-doped microspheres.[34, 35, 81] Here, emission from the dye in the outer portion of the microsphere couples to the WGMs. WGMs were first experimentally observed by Benner et al. from 9.92 μm diameter polystyrene microspheres.[82] The microspheres were suspended in water and excited by an argon laser. Multiple WGMs from individual microspheres were observed as they moved into and out of the excitation spot. Kuwata-Gonokami et al. reported lasing in polystyrene microspheres, ranging in size from 10 to 92 μm, doped with Nile Red dye.[83] The microspheres were placed on a glass slide in a microscope and excited with 5 ns pulses at 520 nm. Evidence for lasing was given as the appearance of sharp peaks at higher powers compared with no WGM structure at lower powers. Enhanced emission was later reported from Schiro and Kwok in 9.8 μm polystyrene microspheres coated with Alexa Fluor 488 fluorescent dye.[84] Individual microspheres were trapped by a near infrared laser and excited by a separate Argon laser to avoid damaging the microsphere with a visible wavelength optical trap. Enhanced emission, and potential lasing, was evidenced by the WGMs having smaller linewidths than the estimated cold-cavity linewidths for the microspheres.

Sensing with Dye-Doped Microspheres

Biosensing was demonstrated in dyed microspheres through the detection of DNA by Nuhiji and Mulvaney.[85] Oligonucleotide bases were labeled with tetramethyl rhodamine and then coupled to thiol-functionalized silica microspheres (7.5 µm in diameter). After immobilization onto a silica grid plate and drying, WGMs were observed from the microsphere before and after hybridization with target DNA strands. Shifts of up to 1.5 nm were observed after hybridization; however, all spectra were recorded in air.

Weller et al. examined the possibility of using small dye-doped polystyrene microspheres for WGM sensing to take advantage of the theoretical 1/R sensitivity dependence on microsphere size.[35] Nile red dyed microspheres ranging from 1.5 to 20 µm in diameter were observed in air for their WGMs. WGM spectra were recorded before and after BSA was coated onto dry 2 µm particles. A 0.86 nm shift was observed due to the BSA coating, which was found to be similar to the theoretical shift predicted by previous perturbation theory.[36] Shifts were also observed as a function of polyelectrolyte layers to obtain a minimum detection limit of 3 fg.

Stimulated emission was observed by Francois and Himmelhaus from 15 µm Nile red doped-microspheres in PBS.[34] An increase in the slope of the peak area as a function of laser power was observed above the stimulated emission threshold that resulted in an eightfold increase in signal-to-noise and a threefold increase in Q-factor. An increase in the adsorption kinetics of BSA to the microspheres was also observed for

the microspheres operating above the stimulated emission threshold, as compared to the kinetics below threshold and with SPR.

Quantum-Dot Labeled or Embedded Microspheres

The previous dye-doped microspheres demonstrated remote, spectral detection of WGMs with the possibility for sensing applications. However, organic dyes are highly susceptible to photobleaching and thus limit the usefulness of this sensor design when continuous or repeated interrogation of the sensor is required. To overcome this problem, QDs may be used as the local light source.

Quantum Dots

As discussed in the introductory chapter, QDs possess a number of unique optical properties that make them an excellent choice for local excitation of WGMs. QDs are colloidal semiconductor nanocrystals in which the electron-hole pair is confined in all three spatial dimensions.[86] Semiconductors possess completely filled valence bands and completely empty conduction bands at low temperatures.[87] The energy separation between these two bands is termed the band gap energy, E_{bg}. When the semiconductor absorbs energy greater than E_{bg}, an electron is promoted from the valence band to the conduction band, leaving behind a hole in the valence band. Emission typically occurs close to E_{bg} when the electron and hole recombine.

The density of states (DOS) for a given energy is the possible number of electron-hole transitions that may take place.[87] As shown in Figure 2.1, in a bulk semiconductor material, the DOS is continuous for energy levels greater than E_{bg}. The confinement of a thin layer of semiconductor in one dimension, as in a quantum well, between two layers of higher band gap materials, is comparable to a potential well with finite barrier potentials. A particle trapped in this well may tunnel to the outside as long as the energies are continuous across the boundaries of the well. Since only specific energies will solve these boundary conditions, the energy is quantized in the dimension of confinement. The DOS for a quantum well becomes a series of subbands, with the edge of each subband shifted to higher energies. This shift in energy is due to an additional confinement energy, which is proportional to $1/d^2$. In QDs, the semiconductor material is confined in all three dimensions. Thus, the energy is quantized in all three dimensions, limiting the DOS to a series of discrete energies, as shown in Figure 2.1.

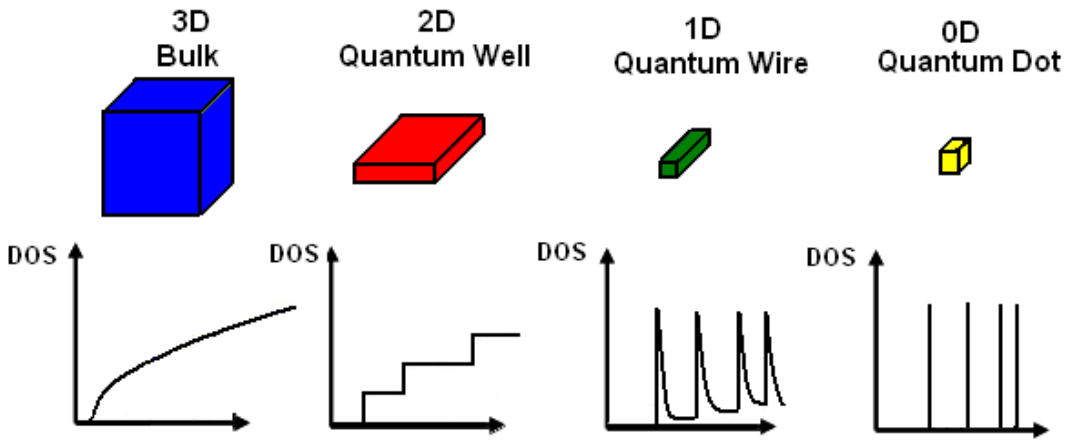

Figure 2.1: Density of States. Density of states for a semiconductor material as it is reduced from a 3D to 0D material (adapted from Bryant, G. W. and Solomon, G. S.[87]).

WGMs in QD-Coated Microspheres

Fan et al. demonstrated WGMs in fused silica spheres coated with CdSe/ZnS QDs ranging in size from 20 to a few hundred micrometers. The microspheres were made by melting the tip of an optical fiber; QDs in chloroform were deposited onto the microsphere surface using a solution deposition method. These microspheres demonstrated multiple WGMs with Q-factors of up to 10^8 and a decrease in Q-factor for modes within the absorption band of the QDs.[88] Rakovich et al. demonstrated WGMs in high refractive index melamine formaldehyde (m = 1.68) microspheres of ~5 μm coated with CdTe QDs.[89] Layer by layer deposition of negatively charged polystyrenesulfonate sodium salt (PSS) followed by positively charged poly(allylamine hydrochloride) (PAH)

was used to increase the positive charge of the microspheres to bind to the negatively-charged QDs. WGMs with Q-factors of ~2600 were observed from the microspheres in water, and a nonlinear increase in the peak power of select modes was observed with increased excitation power. Layer by layer deposition was also used by Gomez et al. to demonstrate the possibility of tuning the WGM positions from 5 μm silica microspheres coated with CdSe/ZnS QDs. Silica particles were coated with polyethylenime (PEI) followed by PSS and a second layer of PEI to bind to the negatively-charged QDs. To improve the stability of the QDs, the microspheres were overcoated with a thin silica shell. This deposition was shown to produce a blue shift in the overall WGM spectra from the microsphere.

QDs Embedded into Polystyrene Microspheres

Quantum dots embedded into polystyrene microspheres have previously been examined for biological assays. Han et al. embedded controlled-intensity levels of different colors of CdSe/ZnS QDs into polystyrene microspheres to create a wide array of different codes for multiplexing applications.[90] By identifying the various colors and intensity levels of each color embedded in each microspheres, a specific tag could be identified. Function of these microbeads was demonstrated using three-color beads bound to strands of probe DNA. When fluorescently-labeled target DNA hybridized to the probe DNA on the microbeads, the signals from the fluorescent label and three colors of QDs in the microbeads was detected to identify the target. Similar microspheres

were also tagged with polyvalent immunoglobulins to detect p-glycoprotein on adenocarcinoma cells.[91] Studies were also performed to examine the penetration of the QDs into the microspheres. It was determined that for non-porous polystyrene microspheres with limited swelling that the penetration of the QDs is limited to just the peripheries of the microspheres.[92, 93]

WGMs in QD-Embedded Microspheres

Directed laser emission was claimed by Zhang et al. in QD embedded polystyrene microspheres with diameters ranging from 6 to 9 μm.[94] Optical tweezers were used to both trap and excite the microspheres. A threshold for lasing was apparent from the nonlinear dependence of peak intensity on excitation power. Ellipsoidal particles demonstrated both WGMs and directed laser emission that was believed to stem from select WGM resonances.

Pang et al. demonstrated the sensing capabilities of QD-embedded polystyrene microspheres excited with two-photon excitation.[95] Microspheres were swollen in 20% chloroform in butanol, and QDs were allowed to passively diffuse into the exteriors. QD-embedded microspheres in water were excited within the two-photon excitation volume at the equator of the microsphere to improve visibility. The surrounding fluid was changed from water to various ethanol/water mixtures to demonstrate the refractive index sensitivity of the microspheres. The sensitivity was found to be approximately

five times greater than the asymptotically approximated shift for a homogeneous microsphere.

Summary

As outlined above, WGMs have been used for sensing applications in resonators including micro-fabricated array devices, capillary-based resonators and microspheres. Microsphere-based WGM biosensors have evolved from relatively large silica microspheres excited through evanescent coupling to smaller, remotely excited microspheres with dye or QDs as local light sources. The large silica microspheres continue to maintain their advantage of having much larger Q-factors to allow for better shift resolution, but suffer from the required coupling mechanism. Dye-doped microspheres have shown greater overall refractive index sensitivity, simpler WGM spectra to allow for easier detection of specific peaks, and the ability to monitor multiple WGMs simultaneously. However, thus far many of these sensors have required detection in air, which is problematic for many biosensing applications, and suffer from high susceptibility to photobleaching. WGMs have recently been observed in QD-embedded microspheres but thus far have only been used in sensing to detect bulk index changes with costly two-photon excitation.

CHAPTER III

WHISPERING GALLERY MODE THEORY

Theory of WGMs

Whispering Gallery Modes (WGMs) were originally studied for acoustic waves by Lord Rayleigh to explain the "whispering gallery" at St. Paul's cathedral in London, England.[26] The theoretical framework for elastic (scattering) interaction between plane waves and spherical objects was originally studied by Mie and subsequently extended to a wide range of objects.[96-99] However, it was not until 1978 that the fine Mie scattering structure was fully resolved when Chylek and co-workers theoretically recognized, the existence of very narrow optical morphology-dependent resonances by reducing the increment of the size parameter $x=2\pi r/\lambda$ from 10^{-3} to 10^{-5}.

Physically, as shown in Figure 3.1, these modes can be viewed as a ray propagating around the internal surface of a microsphere, striking the surface at an angle greater than the critical angle so it is confined to the microsphere sphere by total internal reflection. After traveling one complete circumference, the wave returns to the starting position in phase to produces a standing wave as shown in Figure 3.2.

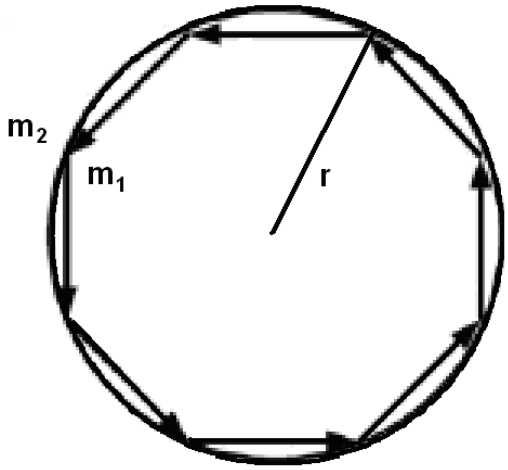

Figure 3.1: Geometric Optics View of WGMs. WGM in a microsphere viewed as a ray propagating around the internal surface of a microsphere (modified from [69]).

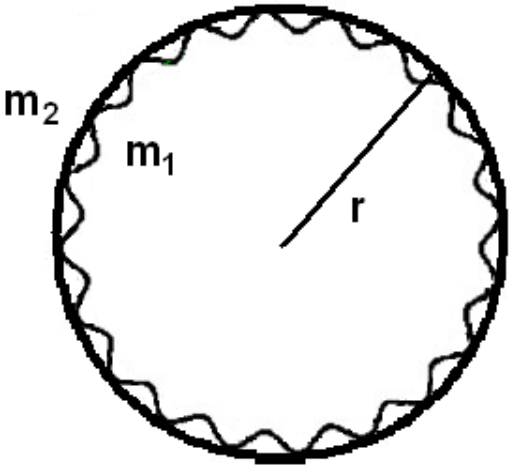

Figure 3.2: Standing Wave View of WGMs. WGM in a microsphere viewed standing wave around the internal surface of a microsphere (modified from [69]).

Mie Scattering Theory

WGMs are often theoretically described using Mie scattering theory, which decomposes an incident plane wave into an infinite number of spherical modes in order to solve the vector wave equation:

$$\nabla \times \nabla \times \mathbf{E} - k^2 m^2(r)\mathbf{E} = 0 \qquad (3.1)$$

In this equation, **E** is the electric field, k is the wavevector and m(r) is the refractive index as a function of the radial distance, r. These spherical modes are either transverse electric (TE) or transverse magnetic (TM) and have electric fields $\mathbf{M}_{l,i}(r,\theta,\varphi)$ and $\mathbf{N}_{l,i}(r,\theta,\varphi)$, respectively. The electric fields are described by an angular mode number, *l*, the number of wavelengths around the circumference of the particle and radial mode order, *i*, the number of maxima in the radial direction. The frequency of the resonance is described by the wavevector, $k=2\pi/\lambda$, where λ is the vacuum wavelength. The spherical vector equations for these electric fields are functions of the scalar radial functions $S_l(r,k)$ and $T_l(r,k)$, for TE and TM modes respectively, and angular functions $\mathbf{X}_{l,i}(\theta)$, $\mathbf{Y}_{l,i}(\theta)$ and $\mathbf{Z}_{l,i}(\theta)$. These equations are given below:[99]

$$\mathbf{M}_{l,i}(r,\theta,\varphi) = \frac{\exp(ji\varphi)}{kr} S_l(r,k)\mathbf{X}_{l,i}(\theta) \qquad (3.2a)$$

$$\mathbf{N}_{l,i}(r,\theta,\varphi) = \frac{\exp(ji\varphi)}{k^2 m^2(r)}\left[\frac{1}{r}\frac{\partial}{\partial r} T_l(r,k)\mathbf{Y}_{l,i}(\theta) + \frac{T_l(r,k)}{r^2}\mathbf{Z}_{l,i}(\theta)\right] \qquad (3.2b)$$

Radial Functions to Describe the WGMs

Of particular interest for WGMs is the radial distribution of the electric fields, which can be described by the following Schrödinger-type differential equations:[99]

$$\frac{d^2 S_l(r)}{dr^2} + \left[k^2 m^2(r) - \frac{l(l+1)}{r^2} \right] S_l(r) = 0 \qquad (3.3a)$$

$$\frac{d^2 T_l(r)}{dr^2} - \frac{2}{m(r)} \frac{dm(r)}{dr} \frac{dT_l(r)}{dr} + \left[k^2 m^2(r) - \frac{l(l+1)}{r^2} \right] T_l(r) = 0 \qquad (3.3b)$$

Using these differential equations, the WGMs may be thought of as quantum-mechanical shape resonances as described by Johnson.[27] In this analogy, a dielectric potential well traps the electromagnetic energy near the surface of the microsphere. This equation includes a potential function, $V_l(r) = k^2[1 - m^2(r)]$, and a centrifugal potential, $\frac{l(l+1)}{r^2}$ for a total potential of:

$$V_l(r) = k^2[1 - m^2(r)] + \frac{l(l+1)}{r^2} \qquad (3.4)$$

The solutions to this differential equation for the radial functions $S_l(r,k)$ and $T_l(r,k)$ depend on the spherical Ricatti-Bessel and Ricatti-Neumann functions,

$$\psi_l(mkr) = mkrj_l(mkr) \qquad (3.5a)$$

$$\chi_l(mkr) = mrkn_l(mkr) \qquad (3.5b)$$

respectively, where $j_l(mkr)$ is the spherical Bessel function and $n_l(mkr)$ is the spherical Neumann function.[27, 73] Inside the microsphere:

$$S_l(r) = T_l(r) = \psi(m_1 kr) \tag{3.6}$$

and outside the microsphere:

$$S_l(r) = B_l[\chi_l(m_2 kr) + \beta_l \psi(m_2 kr)] \tag{3.7a}$$

$$T_l(r) = A_l[\chi_l(m_2 kr) + \alpha_l \psi(m_2 kr)] \tag{3.7b}$$

Here, m_1 and m_2 are the indices of refraction for the microsphere and the surrounding medium, respectively. Since the electromagnetic energy is confined to the potential well on the inside of the microsphere, and may only tunnel outside of this well in the form of an evanescent field, the wavefunction on the outside of the microsphere must be decreasing.[27] Thus, at the resonance, the coefficients for the increasing $\psi(m_2 kr)$ must be equal to zero. Outside of the microsphere, at resonance, the equations become:

$$S_l(r) = B_l \chi_l(m_2 kr) \tag{3.8a}$$

$$T_l(r) = A_l \chi_l(m_2 kr) \tag{3.8b}$$

In quantum mechanics, the only allowed energies in a potential well are those that satisfy the boundary conditions.[27] Likewise, as shape resonances, the WGMs must also satisfy their boundary conditions. Thus, by applying these conditions, the specific resonances may be calculated. The boundary conditions for TE modes state that $S_l(r)$ and $S_l'(r)$ must be continuous across the microsphere/medium interface. By combining these two boundary conditions, the resonance conditions for TE modes, in a given microsphere radius of a, may be specified as:

$$m_1 \frac{\psi_l'(m_1 ka)}{\psi_l(m_1 ka)} = m_2 \frac{\chi_l'(m_2 ka)}{\chi_l(m_2 ka)} \tag{3.9a}$$

For TM modes, $T_l(r)$ and $T_l'(r)/[m(r)]^2$ must be continuous, so the resonance conditions are specified as:

$$\frac{1}{m_1}\frac{\psi_l'(m_1 ka)}{\psi_l(m_1 ka)} = \frac{1}{m_2}\frac{\chi_l'(m_2 ka)}{\chi_l(m_2 ka)} \tag{3.9b}$$

The prime in each case indicates the derivative of the function, which is solved using the recurrence relations:

$$\psi'_l(x) = \psi_{l-1}(x) - \frac{l\psi_l(x)}{x} \tag{3.10a}$$

$$\chi'_l(x) = \chi_{l-1}(x) - \frac{l\chi_l(x)}{x} \tag{3.10b}$$

For each angular mode number, multiple values of k satisfy this equation and correspond to the various radial mode numbers. The minimum value of k that satisfies the resonance condition corresponds to a first-order radial mode. Increasing solutions for k correspond to increasingly higher orders. Figure 3.3 shows the first, second, and third order radial functions (blue) and their corresponding potential functions (red) for a 4.8 μm in radius polystyrene microsphere in air.

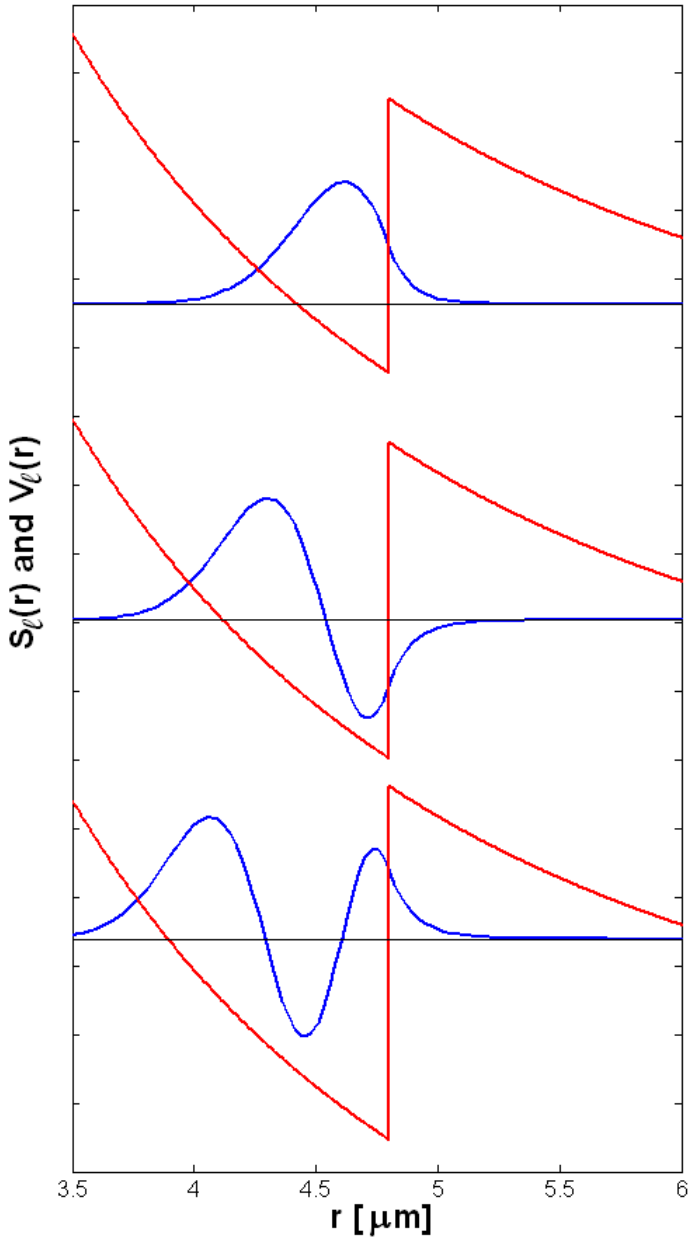

Figure 3.3: Potential Well and WGM Radial Functions. Potential well (red) and TE radial functions (blue) for a 4.8 μm radius polystyrene microsphere in air. First, second and third order functions are shown from top to bottom.

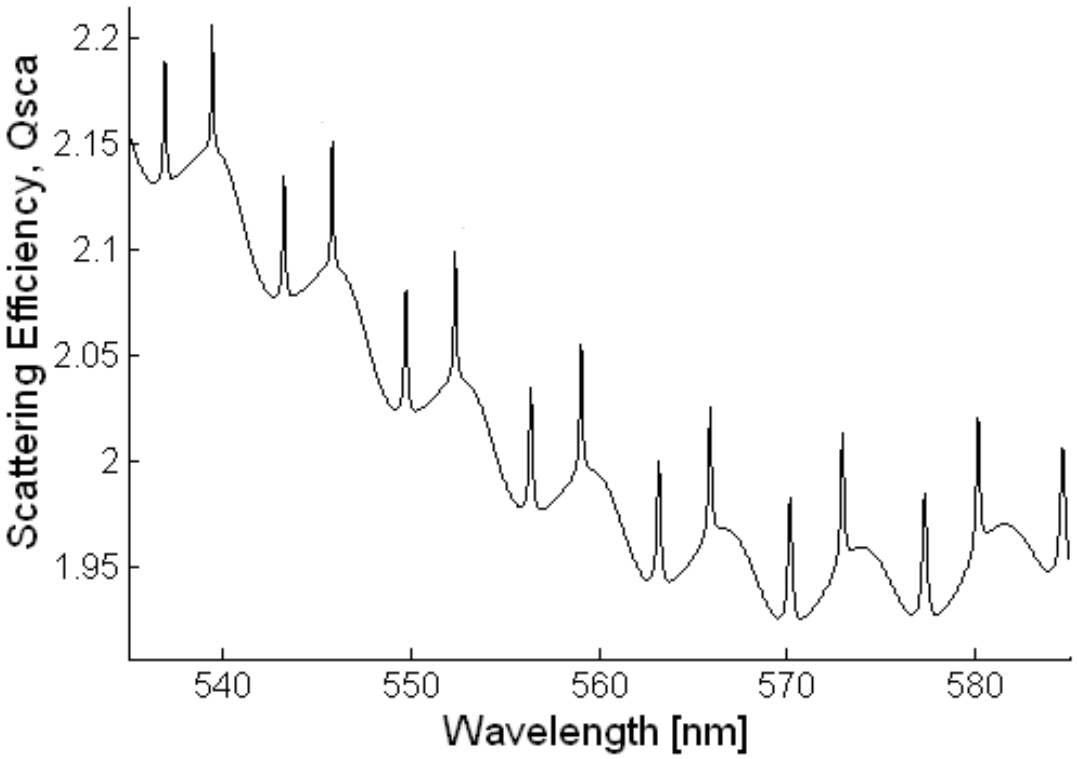

Figure 3.4: Mie Scattering Efficiency. Mie scattering efficiency for a 4.8 μm polystyrene microsphere in water.

Comparison to Mie Scattering Coefficients

The resonance equation for a homogeneous microsphere can be directly related to Mie scattering theory. The scattering efficiency is defined, with a_l and b_l defined as the Mie coefficients and x as the dimensionless size parameter $x = \frac{2\pi}{\lambda} m_2 a$, as:[99]

$$Q_{sca} = \frac{2}{x^2} \sum_{l=1}^{\infty} (2l+1)(|a_l|^2 + |b_l|^2) \qquad (3.11)$$

The Mie scattering efficiency of a 4.8 μm polystyrene microsphere in water is shown in Figure 3.4. The Mie scattering coefficients are defined by Bohren and Huffman using the Riccatti-Bessel functions as:[99]

$$a_l = \frac{\psi_l(x)\psi_l'(mx) - m\psi_l(mx)\psi_l'(x)}{\xi_l(x)\psi_l'(mx) - m\psi_l(mx)\xi_l'(x)} \qquad (3.12a)$$

$$b_l = \frac{m\psi_l(x)\psi_l'(mx) - \psi_l(mx)\psi_l'(x)}{m\xi_l(x)\psi_l'(mx) - \psi_l(mx)\xi_l'(x)} \qquad (3.12b)$$

$\xi_l(x)$ is defined as $\xi_l(x) = \psi_l(x) + i\chi_l(x)$, and m is the ratio of the relative refractive index m_2/m_1. $\xi_l(x)$ can be eliminated from the Mie coefficients by defining the following functions in terms of $\psi_l(x)$ and $\chi_l(x)$ only:[100]

$$p_{TM} = \psi_l(x)\psi_l'(mx) - m\psi_l(mx)\psi_l'(x) \qquad (3.13a)$$

$$q_{TM} = \chi_l(x)\psi_l'(mx) - m\psi_l(mx)\chi_l'(x) \qquad (3.13b)$$

$$p_{TE} = m\psi_l(x)\psi_l'(mx) - \psi_l(mx)\psi_l'(x) \qquad (3.13c)$$

$$q_{TE} = m\chi_l(x)\psi_l'(mx) - \psi_l(mx)\chi_l'(x) \qquad (3.13d)$$

Thus, the Mie coefficients are now:

$$a_l = \frac{p_{TM}}{p_{TM} + iq_{TM}} = \frac{{p_{TM}}^2}{{p_{TM}}^2 + {q_{TM}}^2} - j\frac{p_{TM}q_{TM}}{{p_{TM}}^2 + {q_{TM}}^2} \qquad (3.14a)$$

$$b_l = \frac{p_{TE}}{p_{TE} + iq_{TE}} = \frac{{p_{TE}}^2}{{p_{TE}}^2 + {q_{TE}}^2} - j\frac{p_{TE}q_{TE}}{{p_{TE}}^2 + {q_{TE}}^2} \qquad (3.14b)$$

The real and imaginary portions of these coefficients are plotted in Figure 3.5 for a 5 μm microsphere with an refractive index of 1.59 in water (m_2=1.333). The angular mode number is 84. As demonstrated in this figure, when the imaginary portion of the a_l and b_l coefficients approach 0 (changes sign), the real portion of these coefficients is at its maximum value. This spike in the real portion of the coefficient is seen as a spike in the scattering spectrum, indicative of an optical resonance. Thus, by setting the q_{TM} and q_{TE} equations to 0, we can calculate the resonance conditions for a given value of *l*. Conveniently, these equations are identical to the resonance conditions described earlier for a homogenous sphere of relative index m.

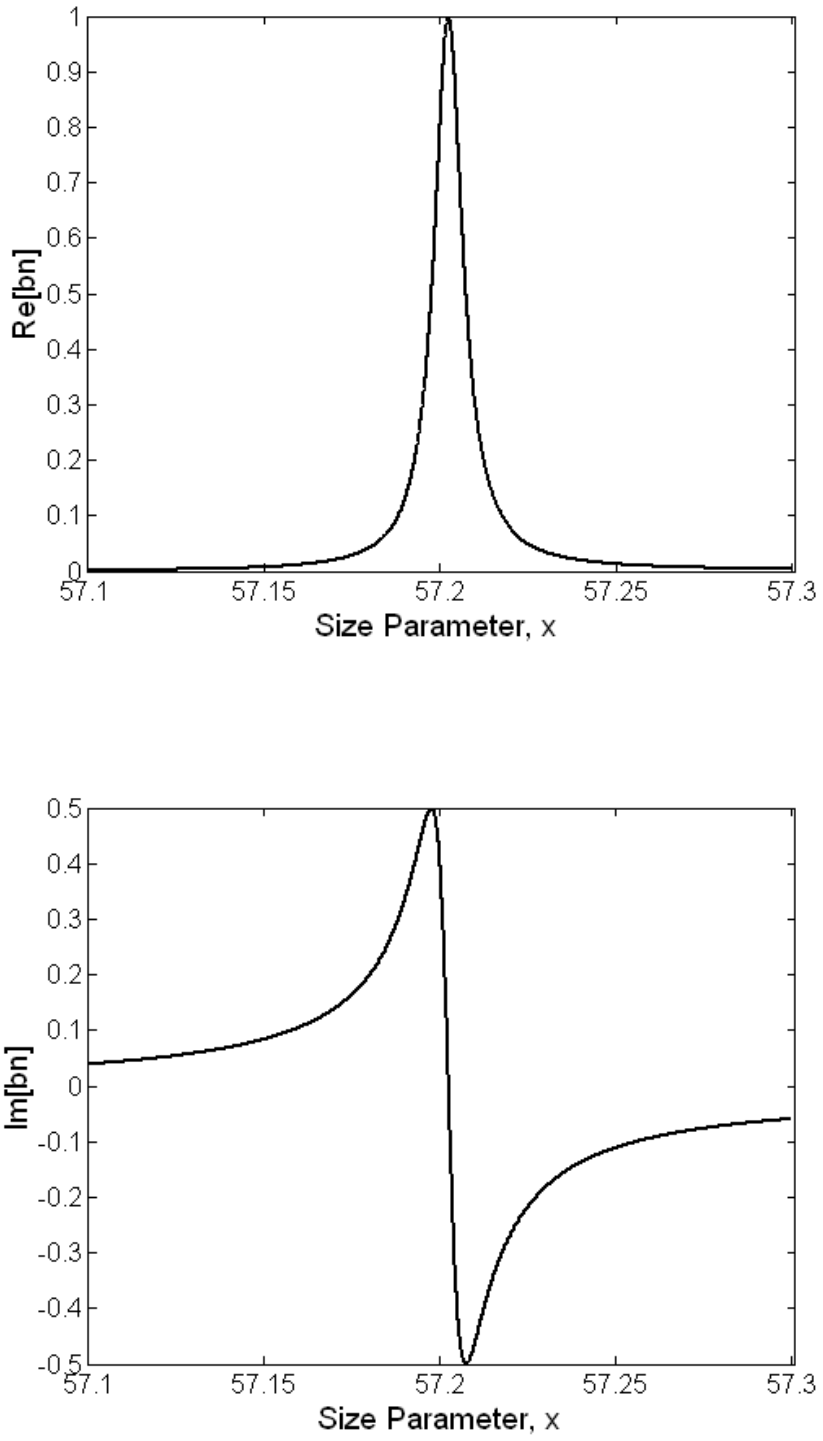

Figure 3.5: Real and Imaginary Portions of b_l. The real and imaginary portions of b_l for a 5 μm microsphere (m=1.59) in water with l = 84.

Linewidth and Q-factor

In most WGM theory papers, the linewidth is defined for TE modes as:[27, 77]

$$\omega_l(x_0) = \frac{2}{\beta_l'(x_o)} \tag{3.15}$$

Where x_o, is the resonance in terms the unitless size parameter, where $\beta_l(x_0) = 0$ and the real part of b_l:

$$\mathrm{Re}[b_l(x)] = \frac{1}{1+\beta_l^{\,2}(x)} \tag{3.16}$$

The linewidth can also be more accurately calculated directly from the Mie coefficients The Mie resonances are at half of their maximum intensity when the real portion of the scattering coefficients is equal to 1/2. Thus, the linewidth can easily be determined by calculating the space between these two points on each side of the resonance. The Q-factor, $Q = \frac{\Delta\omega}{\omega}$, can then be calculated from the linewidth, Δω, and corresponding resonance frequency, ω. The average time a photon remains circulating within the resonator, τ, is determined from the Q-factor as $\tau = Q/\omega$.[25]

High Index Outer Layer

Adding a high index layer to the outside of the microsphere has been demonstrated to push the radial distributions, $S_l(r)$ and $T_l(r)$, outward, intensifying the evanescent field and causing the WGM to become more sensitive to changes in

refractive index.[77, 78] This high index layer is described by a thickness, t, and refractive index, m_3, while keeping the total microsphere radius, a, consistent, as shown in Figure 3.6.

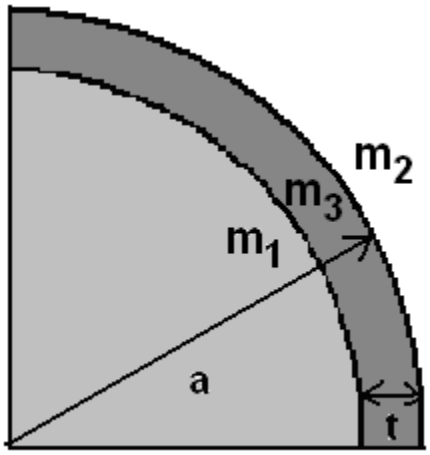

Figure 3.6: High Index Layer on a Microsphere.

Inside the high index layer, the radial distribution is expressed as the linear combination of the Riccatti-Bessel and Riccatti-Neumann functions. Thus:

$$S_l(r) = \begin{cases} A_l \psi_l(m_1 kr) & r < a - t \\ C_l \psi_l(m_3 kr) + D_l \chi_l(m_3 kr) & a - t < r < a \\ B_l \chi_l(m_2 kr) & a < r \end{cases} \qquad (3.17)$$

Using the same method as with a homogeneous sphere of requiring the equations for $S_l(r)$ and $S_l'(r)$ to be continuous across each boundary, the resonance conditions for TE modes can be calculated from the following equations:

$$\frac{m_2\chi_l'(m_2ka)}{m_3\chi_l(m_2ka)} = \frac{(C_l/D_l)\psi_l'(m_3ka)+\chi_l'(m_3ka)}{(C_l/D_l)\psi_l(m_3ka)+\chi_l(m_2ka)} \qquad (3.18a)$$

and

$$\frac{C_l}{D_l} = \frac{m_3\psi_l(m_1k(a-t))\chi_l'(m_3k(a-t))-m_1\psi_l'(m_1k(a-t))\chi_l(m_3k(a-t))}{-m_3\psi_l(m_1k(a-t))\psi_l'(m_3k(a-t))+m_1\psi_l'(m_1k(a-t))\psi_l(m_3k(a-t))} \qquad (3.18b)$$

Likewise, using the boundary conditions of $T_l(r)$ and $T_l'(r)/[m(r)]^2$ for TM modes, the boundary conditions are found from:

$$\frac{m_3\chi_l'(m_2ka)}{m_2\chi_l(m_2ka)} = \frac{(C_l/D_l)\psi_l'(m_3ka)+\chi_l'(m_3ka)}{(C_l/D_l)\psi_l(m_3ka)+\chi_l(m_2ka)} \qquad (3.19a)$$

and

$$\frac{C_l}{D_l} = \frac{m_1\psi_l(m_1k(a-t))\chi_l'(m_3k(a-t))-m_3\psi_l'(m_1k(a-t))\chi_l(m_3k(a-t))}{-m_1\psi_l(m_1k(a-t))\psi_l'(m_3k(a-t))+m_{31}\psi_l'(m_1k(a-t))\psi_l(m_3k(a-t))} \qquad (3.19b)$$

As with the homogenous microsphere, multiple values of k satisfy these resonance equations. The minimum value of k that satisfies the resonance condition corresponds to the first radial mode.

CHAPTER IV

METHODOLOGY*

Introduction

The methods used throughout this dissertation are described in this chapter for convenience and to avoid repetition. This section begins with a description of how the quantum dots were made, embedded into microspheres and how the microspheres were immobilized for imaging and recording WGM spectra. Next, the optical systems used for the experimental sections are described. Finally, the experimental methods are detailed.

Preparation of Quantum Dots

QDs are prepared colloidally, via organomettallic synthesis essentially described by Peng et. al.[101] Briefly, cadmium oxide, trioctylphosphine oxide (TOPO) and tetradecylphosphoic acid (TDPA) are heated under argon at approximately 320˚C until the solution becomes colorless. After cooling to 270˚C, a solution of selenium dissolved in trioctyphosphine (TOP) is injected and the reaction continues until the desired size of

---

* Part of this chapter is reprinted from "Whispering Gallery Mode Biosensors Consisting of Quantum Dot-Embedded Microspheres" Beier, H.T., Coté, G.L., Meissner, K.E., 2009, *Annals of Biomedical Engineering* (2009). 37(10), 1974-1983, 2009, with kind permission of Springer Science and Business Media.

CdSe QDs are produced. After cooling to 140˚C, precursor solutions of dimethylzinc and hexamethyldisilathiane in TOP are added to the CdSe to form a ZnS shell. The reaction is quenched and dots are washed in methanol and then chloroform. For our experiments we used QDs with an emission peak of ~550 nm. Absorption and emission spectra of the CdSe/ZnS QDs in chloroform is shown in Figure 4.1.

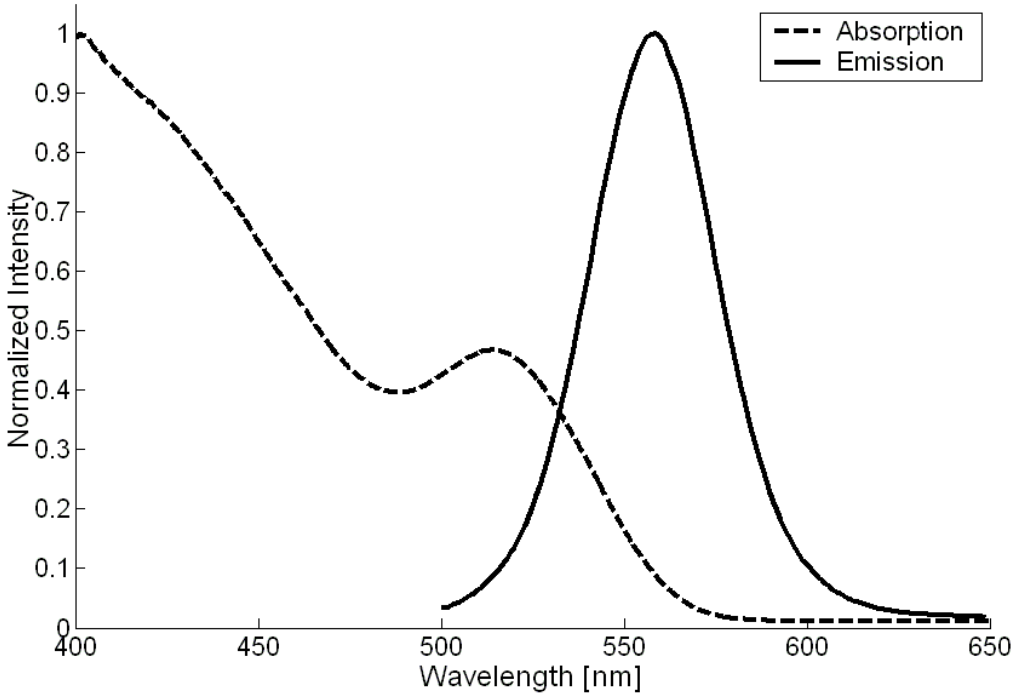

Figure 4.1: Absorption and Emission Spectra of CdSe/ZnS QDs.

Preparation of Quantum Dot Embedded Microspheres

Several versions of polystyrene microspheres were used in these studies. For bulk index and protein adsorption studies, sulfate latex (4.8 µm radius, Interfacial Dynamics Corporation) were chosen for their negative charge to electrostatically bind to a monolayer of polyethyleneimine (PEI) for simple immobilization. For later studies, specifically those involving functionalizing the microspheres with antibodies, carboxyl microspheres (10.941 um diameter, Polysciences) were used for the ability to covalently bind antibodies to their surface. These spheres were immobilized to the substrates using EDC chemistry. Each of the microspheres were embedded with the CdSe/ZnS QDs with an emission maximum of ~550 nm described above.

To embed the QDs in the microspheres, the microspheres are first transferred from water to butanol through ethanol. 25 µL of 4% solids or 50 µL of 2% solids polystyrene microspheres are added to a microcentrifuge tube and diluted to ~1 mL with deionized water. The microspheres are then centrifuged at low speed (~400g) in a mini-microcentrifuge for 10 seconds to pellet. The supernatant is removed and replaced with 1 mL ethanol. The centrifugation procedure is repeated 3X with ethanol and 3X with butanol. After the final butanol wash, the butanol supernatant is removed, leaving ~50 uL of volume. The microcentrifuge tube is shaken slightly to resuspend the pellet in the remaining butanol. In a separate tube, concentrated quantum dots in chloroform are added to enough butanol to have a final chloroform concentration of 10 or 15% by volume (ex. 150 µL $CHCl_3$/ 800 µL BuOH). The $CHCl_3$/BuOH mixture is added to the

microspheres and shaken to mix. The chloroform swells the polystyrene slightly, allowing the QDs to passively diffuse into outer edges of the microspheres. The mixture is agitated for typically 20 minutes at room temperature on a shaker. It is then centrifuged and the QDs/BuOH/$CHCl_3$ supernatant is removed. The pelleted microspheres are then resuspended in ethanol and the centrifugation procedure is repeated 2-3X to remove any free QDs and any remaining chloroform from the mixture. After the final wash, if necessary, water or buffer may be added to the pelleted microspheres, but they should not be centrifuged or the microspheres may be destroyed.

Immobilization of the QDs surprisingly turned out to be a key and somewhat limiting feature of this work. It was found that if the microspheres were embedded with too large a number of QDs that only the luminescent background could be observed with little to no WGM modal structure, whereas too few obviously limited the ability to observe any spectra at all. A key to this issue seemed to be the manufacturer of the polystyrene microspheres. Microspheres from Interfacial Dynamics Corporation (IDC) (Invitrogen) are reported by the manufacturer to not be divinylbenzene (DVB) crosslinked; however, 10 μm and larger microspheres from Polysciences are DVB crosslinked (they did refuse to report the % crosslinker used). All microspheres were ordered as 10 μm microsphere even if their actual measured diameter turned out to be slightly different.

IDC microspheres were easily loaded with high numbers of QDs and required that the diffusion time be controlled to a specific period, and the microspheres transferred to water or ethanol, in order to achieve somewhat consistent results. These

microspheres were beneficial in that they were able to produce a large variety of WGM structures, including overlapping TM and TE modes, with higher values of the QD layer thickness and refractive index as based on the mode spacing. However, the consistency of the microspheres was very difficult to control and the spectra often varied greatly between microspheres, even on the same coverslip. This factor increased experimental times greatly by requiring the repeated searching for a microsphere with modes visible enough to be used for experimentation.

The crosslinked microspheres from Polysciences were overall much more dependable. While the proper concentration of QDs had to be determined empirically for these microspheres, the spectra were significantly more consistent between microspheres once the optimum concentration was found. It did however, seem that the penetration of the QDs was more limited to the very outside of these microspheres than the IDC version. These Polysciences microspheres would also lose much of their luminescence (and visible color) from sitting in ethanol after being embedded with the QDs. To resolve this issue, the microspheres were left in the butanol/chloroform/QD mixture after the initial mixing period until use (up to a month later). Microspheres remained consistent between samples taken on different days and the time sitting in the organic solvents did not seem to have any ill effects. This conclusion is however, purely observational.

It is believed that the tri-*n*-octylphosphine oxide (TOPO) capped QDs should prefer the hydrophobic environment of the polystyrene microspheres and remain embedded indefinitely. However, some possible leaching of QDs from the microspheres

may have occurred. WGMs from embedded microspheres sitting in water for weeks at a time were observed, so it is possible that any leaching was only from the QDs trapped very near the surface of the microspheres.

Immobilization of Microspheres on a Coverslip

A diamond-tip etching pen was used to cut a glass coverslip to fit within a demountable quartz flowcell (Starna Cells). For sulfate microspheres, the coverslip was washed with ethanol and ~100 uL of 5 mg/mL polyethyleneimine (PEI) was added to the slide and then rinsed with DI water after ~30 sec. The coverslip was then dried with N_2 and ~20 uL of QD-embedded microspheres in ethanol were added to the slide and allowed to dry. The coverslip was then adhered to the interior of the flowcell with vacuum grease. The negatively charged microspheres were electrostatically immobilized on the positively charged PEI film and remained stable throughout the experiments.

I had trouble with carboxyl microspheres immobilized to the PEI layer leaving the coverslip when excited with the excitation laser. Thus, the carboxyl-functionalized microspheres were covalently bound to the coverslips. To achieve this immobilization, the coverslips were silianized with terminal amine groups. It was later found that the sulfate microspheres also had better binding to these coverslips than to the PEI.

To silianize the coverslips, the substrates were first cut to the proper size and then cleaned in concentrated sulfuric acid for at least 2 hours. The coverslips were

rinsed extensively with DI water and dried with absolute ethanol. At this point, the surface of the coverslips was very hydrophilic. 5% v/v aminoproplyoxytrimethysilane (APTMS) was added to absolute ethanol with 2% v/v triethylamine. The cleaned coverslips were added to the mixture and incubated at room temperature for several hours. The slips were then rinsed 3X with ethanol and baked in a vacuum oven under vacuum at ~100^0C for 1-2 hours. The slides should now be very hydrophobic.

50 μL of QD-embedded microspheres in ethanol were centrifuged and the ethanol removed. About 4 mg of EDC (Pierce) was added to 500 μL of MES buffer (0.1 M MES, 0.5 M NaCl, pH 6). 200 μL of EDC/MES was added to the microspheres and mixed. An approximate equal weight of Sulfo-NHS was added to the spheres and shaken to mix. After incubating for 20 minutes, 20% of 1 M $NaHCO_3$ was added to the microspheres to raise the pH above 7. The microspheres with activated carboxyl groups were then applied to silianized coverships and allowed to dry. The slides were then rinsed extensively with DI water and examined under a microscope to ensure binding of microspheres to the coverslips.

Care should be taken to ensure that the pH of the MES is close to 6. Even though the NHS esters are more stable at lower pH, it was found that when the pH of the MES was lowered to 5 that the microspheres aggregated, making immobilization difficult. Additionally, better binding was observed when $NaHCO_3$ was added to the microspheres just before adding them to the slides to raise the pH. Centrifuging the microspheres to remove the EDC and replace the MES with a more basic buffer is not recommended as the microspheres may detrimentally aggregate.

EDC quenching agents were also found to not be needed since there is no risk of crosslinking in our procedures.

Optical Systems

Original Continuous Wave Excitation System

Microspheres were imaged individually using the experimental system shown in Figure 4.2. Excitation light from a 488 nm Argon laser (7-50 mW, SpectraPhysics) was filtered through short pass and band pass filters (Chroma, Thorlabs) to remove additional Argon emission lines and focused to an approximately 100 μm diameter spot on the microsphere sample using a microscope objective (10X, N.A = 0.25). Irradiance was adjusted by changing the spot size or the output power of the laser. The excitation spot size was generally kept to at approximately 10x the microsphere diameter to ensure uniform excitation across the microsphere of interest. Luminescent emission was collected by a second microscope objective (20X, N.A = 0.4) and passed through a long pass filter to remove scattered excitation light. A spectrometer (PI-Acton SpectraPro 2300i) with a thermoelectrically cooled charged coupled device (CCD) camera (PI-Acton PIXIS 100) operated for both imaging and spectroscopy modes.

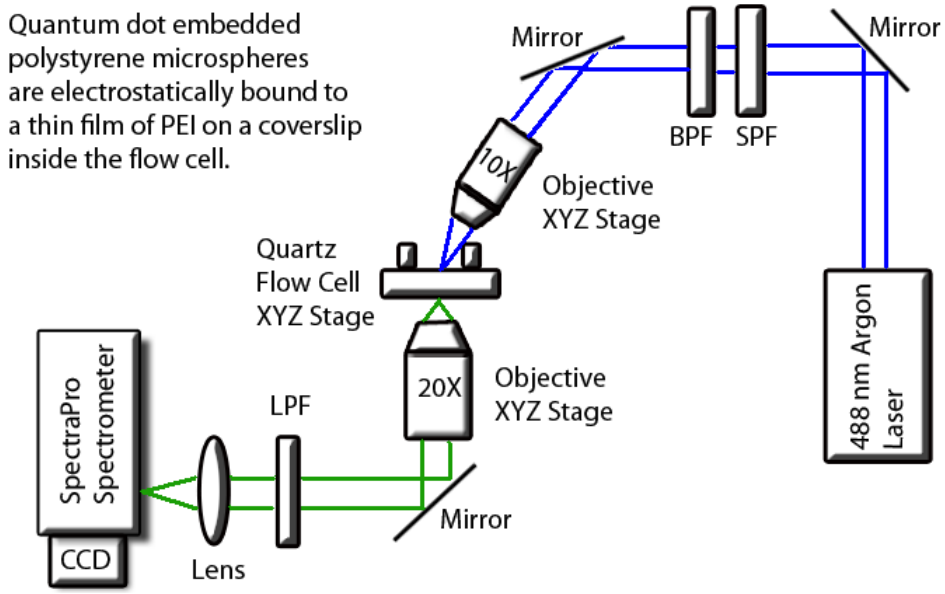

Figure 4.2: Optical Set-Up.

High Resolution Grating

The highest resolution available in the spectrometer in the initial optical setup was 1200 g/mm with a pixel pitch of ~0.04 nm. For biosensing applications, a higher resolution will be required. Thus, for later experiments a 2400 g/mm holographic VIS optimized grating, with a pixel pitch of 0.016 nm, was added to the spectrometer.

Femtosecond System

A doubled femtosecond system was additionally used for later experiments. Laser emission from a Coherent Chameleon (140 fs pulse width) mode-locked

Ti:Sapphire laser was tuned to twice the desired excitation wavelength. After pulse picking with a Coherent 9200 Pulse Picker at 5 MHz, the beam was frequency doubled by an APE SHG tunable second harmonic generator to wavelengths ranging from 400 to 450 nm. Laser light was then coupled into an optical set-up similar to the one used previously.

Experimental Procedures

Bulk Index Experiments

The refractive index of the media surrounding the microspheres was altered by flowing various concentrations of ethanol in water through the flow cell. Approximately ten times the flow cell volume was flowed through the cell with each concentration change to remove the previous sample. Concentrations were changed non-sequentially to ensure the observed shifts are due to refractive index changes and not drift within the system.

Protein Adsorption Experiments

For protein adsorption experiments, 1 mg/mL solutions of bovine serum albumin (BSA) and thrombin from bovine serum (Sigma-Aldrich) in water were slowly injected into the flow cell. Spectra were recorded every ~1 minute while blocking the excitation

beam in between emission scans. After ~20 minutes, solutions containing 10 mg/mL of the proteins were added to the flowcell. WGM spectra were recorded to determine if the surface was saturated at the 1 mg/mL concentration.

Microsphere Functionalization with Antibodies

QD-embedded carboxyl functionalized microspheres were covalently bound to the cover slips using the previously described procedure. The slips were then washed extensively with DI water to remove any remaining coupling reagents and salts. The microspheres were then imaged in the optical set-up and the spectra recorded in water. EDC and Sulfo-NHS were added to 2.5 mL of MES buffer (0.1 M MES, 0.5 M NaCl, pH 6.0), each to final concentrations of ~15-30 mM. 1.5 mL of the buffer solution was added immediately to the flow cell (total volume of flow cell and inlet tubing = 0.5 mL). The remaining 1 mL was added slowly to the flow cell over 20 minutes. After the 20 minutes of incubation, spectra were recorded and the flow cell was then rinsed with 3 mL PBS (0.02 M Na_2HPO_4, 0.15 M NaCl, pH 7.3). Additional spectra were recorded. Rabbit antiserum to human myoglobin (MP Biomedicals) in 2 mL PBS at concentrations ranging from 500 nM to 50 µM, was slowly added to the flow cell. Spectra were recorded every 5-10 minutes for up to two hours.

CHAPTER V

CONTINUOUS WAVE EXCITATION OF QUANTUM DOT EMBEDDED MICROSPHERES*

Introduction

As a first step toward the development of our WGM based sensors for the purpose of biological analyte sensing, we must examine the spectra characteristics of our QD-embedded microspheres using a continuous wave (CW) optical set-up. Using this optical system, these sensors are demonstrated by monitoring the wavelength shift of multiple resonant modes as bulk index of refraction is changed in ethanol-water mixtures. Most likely due to the thin, high index layer of quantum dots, microsensor response demonstrated increased sensitivity over theoretical predictions.

Spectral Characteristics

Spectra Visibility

Figure 5.1(a) shows typical WGM spectra for QD/microsphere sensors at three collection points along the microsphere. Spectra are recorded across the full diameter of

---

* Part of this chapter is reprinted from "Whispering Gallery Mode Biosensors Consisting of Quantum Dot-Embedded Microspheres" Beier, H.T., Coté, G.L., Meissner, K.E., 2009, *Annals of Biomedical Engineering* (2009). 37(10), 1974-1983, 2009, with kind permission of Springer Science and Business Media.

the microsphere, at the upper edge from the center of the microsphere, and on a side edge of the microsphere. All spectra clearly show multiple transverse magnetic (TM) and transverse electric (TE) paired modes. These WGM peak locations remain consistent across the entire microsphere. However, visibility, defined as $V = (I_{peak} - I_{background})/(I_{peak} + I_{background})$,[102] is improved by excluding the center of the microsphere due to elimination of QD luminescence that does not couple to the WGMs. These results indicate that WGM location is independent of the collection point from the microsphere and allow flexible detection schemes using all or just a portion of the sphere: a benefit for remote biosensing applications especially when multiplexed approaches are considered. The visibility of the WGMs in Figure 5.1(a) can be compared with those in Figure 5.1(b) for two microspheres swollen with a higher concentration of QDs for a period of several days, as was used in our previous two-photon excitation work. It is clear that controlling the background luminescence is essential for effectively visualizing the WGM peaks using CW excitation.

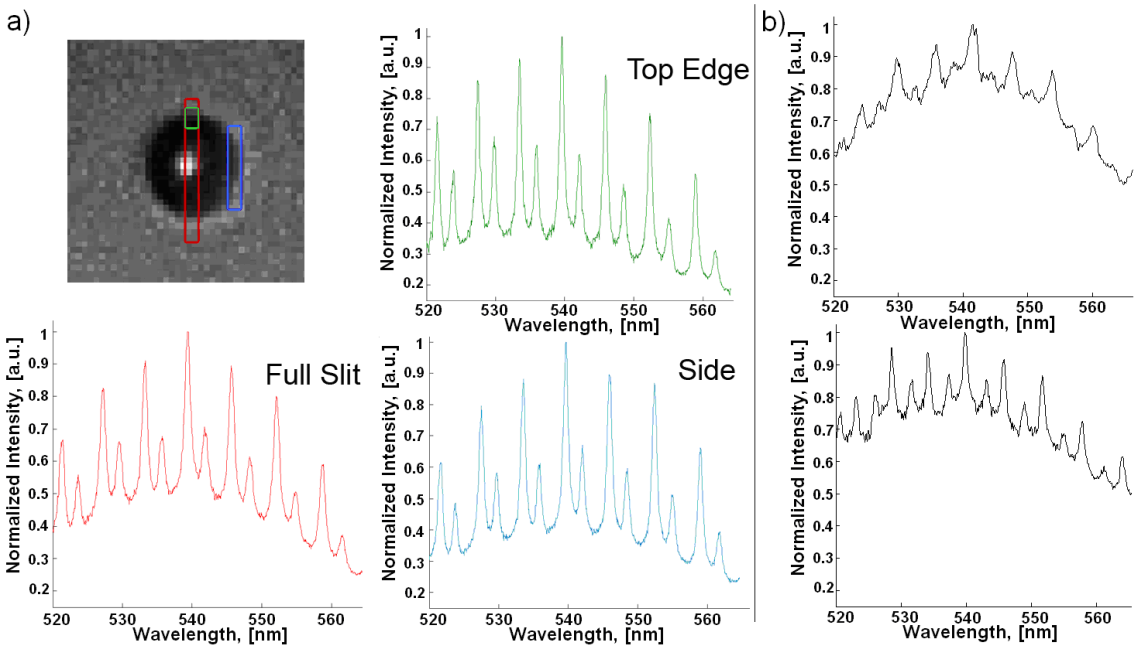

Figure 5.1: WGM Spectra Visibility. a) Brightfield image of the QD-embedded microsphere (upper-left) with collection areas indicated. Spectra were recorded using the center of the microspheres across the full diameter of the microsphere, by selectively looking at just the upper edge from the center of the microsphere, and on a side edge of the microsphere as indicated. b) Spectra of two microspheres swollen with a higher concentration of QDs for a period of several days.

Spectra Stability

A second requirement for developing biosensor technology is the ability for the sensors to be used for extended time periods. Figure 5.2 shows the WGM stability with time and irradiance. At low irradiance (20 W/cm^2) WGM peak location (a) and relative emittance (b) remained stable over 5 minutes of continuous laser excitation. A slight blue-shift in the modes was observed at higher irradiance (c); this result is believed to be due to heating of the microsphere. However, even at the highest irradiance (140 W/cm^2), (d), the blue shifts in the peaks were very slight and remained stable once a thermal equilibrium was reached. These results indicate that by controlling the laser power and spot size, the microspheres may be used for repeatable and robust measurements with limited susceptibility to photobleaching. In normal circumstances, excitation of the microspheres will only be required when data is being collected; thus limiting any photobleaching and slight blue shift of the modes.

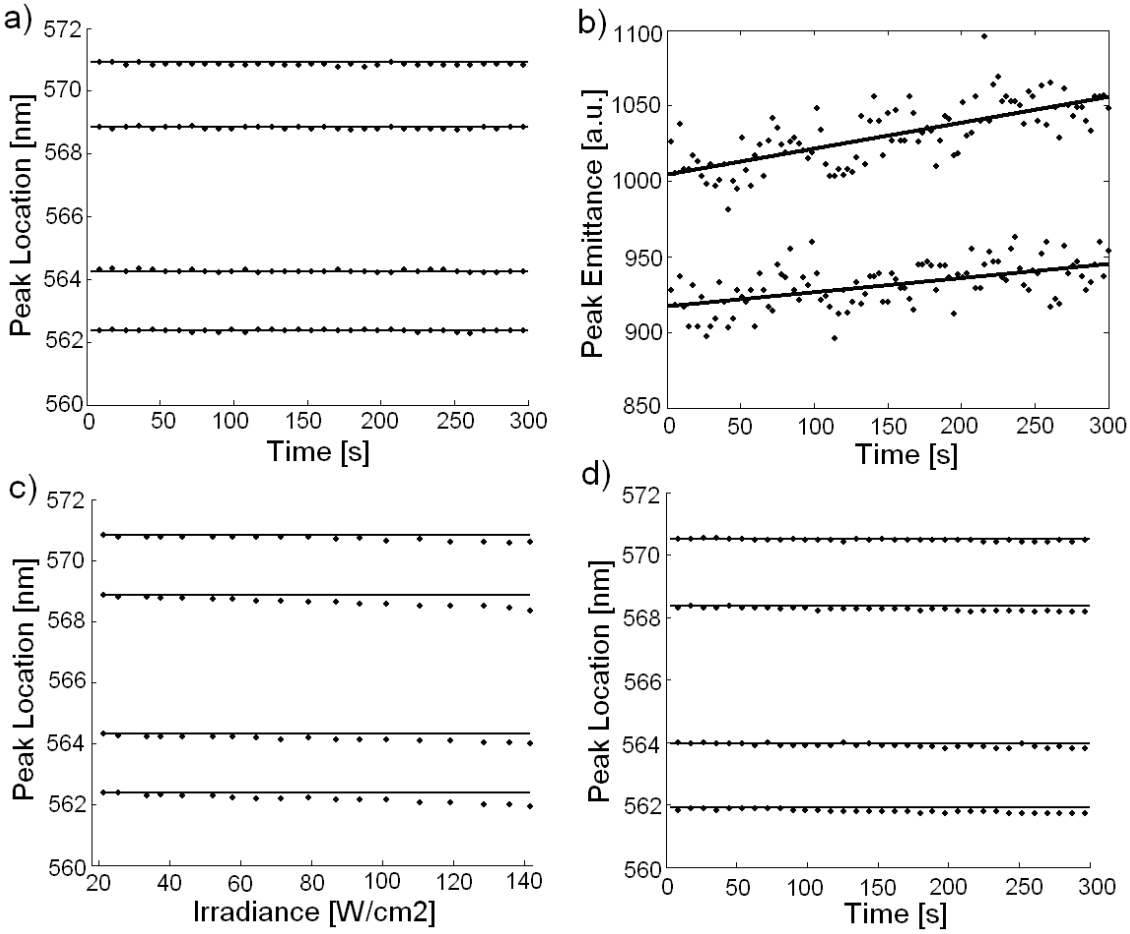

Figure 5.2: WGM Stability. WGM stability over time and with increasing laser power. A) Peak location verses time for continuous excitation at 20 W/cm^2 for 5 min. B) Peak intensity versus time for three characteristic peaks using continuous excitation at 20 W/cm^2 for 5 min. C) Peak location as a dependence on excitation irradiance. D) Peak location versus time for continuous excitation at 140 W/cm^2 for 5 min.

Response to Bulk Index Changes

Since the formulation of QD/microspheres was changed to account for the increased background luminescence due to CW excitation, the sensitivity of the new microspheres had to be established. To characterize the refractrometric sensitivity and repeatability of these WGM sensors, we examined the perturbation of the WGM spectra in response to bulk changes in refractive index. Six different weight ratios of ethanol to water were flowed through the flow cell. Mixtures were added in a non-sequential order to ensure the observed shifts were not a secondary effect based on direction of refractive index change. Additionally, the shifts for each of the concentrations were obtained on two separate occasions and were averaged for each WGM, to further demonstrate sensor reversibility and sensitivity. This procedure was repeated on three individual microspheres.

As demonstrated in the inset of Figure 5.3, WGMs of the same mode number showed a red-shift with increasing refractive index. The modes are indicated as TM (solid, black arrow) and TE (dashed, red arrow), based on the mode spacing obtained from Equations 1 and 2. The shifts of these modes from their original position in pure water is plotted in Figure 5.3. Sensitivity calculated from experimental results is ~100 nm/RIU (refractive index unit). As expected, each mode has a slightly different sensitivity to RI changes. By linearly fitting the shift of multiple WGMs independently, the accuracy of the estimation may be improved over monitoring a single WGM shift.

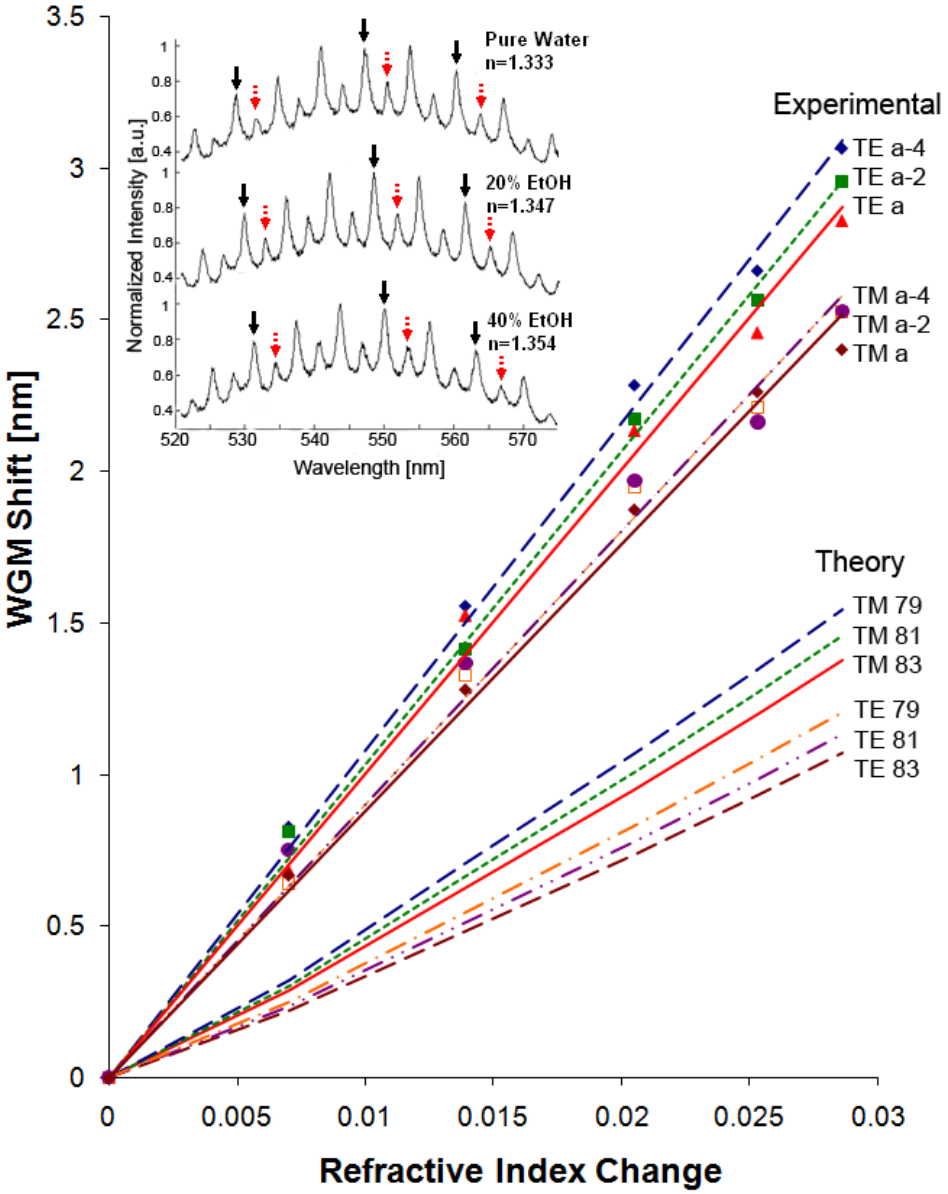

Figure 5.3: Experimental and Theoretical Refractive Index Sensitivity. Comparison between the experimental and theoretical WGM shift in response to refractive index change. Each line represents a linear fit for an individual mode. Sensitivities are on average 96.8 nm/RIU for the experimental results and an average of 45.4 nm/RIU for the theoretical results. Theoretical results were obtained using Mie scattering theory for the average size microsphere. Inset: WGM spectra from a microsphere for different weight ratios of ethanol in water. A red shift in the spectra can be clearly seen as the refractive index increases. The solid black arrows indicate TM modes; dashed red arrows indicate TE modes.

The linear fit of each WGM shift, along with each measured wavelength shift, was used to calculate the refractive index change for each ethanol-water concentration. Fitted refractive index calculations for the mixtures are 0.00755, 0.0146, 0.0213, 0.0246, and 0.028 RIU shifts for the 10, 20, 30, 40 and 50 weight % ethanol in water mixtures, respectively. Standard deviations for the calculations ranged from 3.08 X 10^{-4} to 5.66 X 10^{-4}, which is comparable to our estimated minimum detectable refractive index change for this sensitivity of 4 X 10^{-4} RIU, using a wavelength pitch of 0.04 nm. Thus, the current limiting factor for the sensitivity of our microspheres is the resolution of our spectrometer.

Determination of the Enhancement of the Sensitivity

To determine the enhancement in sensitivity for our microspheres, these WGM shifts are compared experimentally to the theoretical model described in Chapter III. Our theoretical approximation assumed homogeneous 4.6, 4.8 and 5.0 μm radius microspheres with an index of refraction of 1.591. The bulk refractive index sensitivities as well as the spacing between the TM and TE modes and between pairs of modes are given in Table 5.1 for both the experimental and theoretical results. The refractive index sensitivities were calculated by linearly fitting the average of the WGMs shifts for each concentration of ethanol in water for the WGM resonances between 535 and 560 nm. Mode spacing is calculated as the average spacing for the resonances between these wavelengths. Since the spacing between TM and TE modes and pairs of modes varied

from the theoretical models, it was difficult to fit the size of the microspheres to an exact size. Thus, the average size of our batch of microspheres, 4.8 µm, was used to compare the enhancement in sensitivity for these microspheres with the theoretical model for a homogeneous microsphere. The enhancement between the three observed microspheres is relatively consistent; differences are believed to be due to slight difference in microsphere size and depth and concentration of embedded QDs.

TABLE 5.1: Bulk Refractive Index Sensitivity for Three Microspheres

	Average TM Shift [nm/RIU]	Average TE Shift [nm/RIU]	TM-TE Spacing [nm]	TM-TM Spacing [nm]	Enhancement over 4.8 µm Model
Sphere A	86.61	111.88	2.60	6.41	2.16
Sphere B	91.30	103.76	3.07	6.36	2.12
Sphere C	89.33	100.78	2.37	6.03	2.07
4.6 µm Model	54.02	42.11	2.69	6.70	
4.8 µm Model	51.69	40.27	2.64	6.42	
5.0 µm Model	48.78	37.98	2.57	6.16	

Similar to our group's previous two-photon work, the enhancement in RIU sensitivity with our QD/microspheres is believed to be due to the thin QD layer at the periphery.[95] Recent theoretical work indicates that a thin, high refractive index layer can move the confinement of WGM energy closer to the surface and make the system more sensitive to changes in refractive index.[77, 78, 95] The observed enhancement in these experiments was slightly smaller than in our previous work: ~2.1X compared to ~5X. It should be noted that the previous work used an asymptotic approximation of the

resonance conditions to calculate the expected WGM shifts. When this approximation is used for our current data, we calculate our enhancement to be ~2.9X, indicating the calculated enhancement for the previous work was slightly inflated. The asymptotic approximation is valid for microspheres much larger than the wavelength of light.[103] Since our 9.6 μm diameter microspheres are at the smaller ended of this limitation, and the theory used here is not limited by microsphere size, our current calculations are more accurate.

In our earlier work, the polystyrene microspheres were swollen in a higher concentration of chloroform in butanol for up to several days instead of only 20 minutes as in these experiments. The longer incubation time is believed to allow the QDs to diffuse deeper into the polystyrene matrix, possibly creating a larger and higher index layer of embedded QDs. The QD/microsphere formulation was altered to limit background luminescence in the current CW excitation experiment; the necessity for which is demonstrated in Figure 5.1. It should also be noted that our experimental results indicated a greater shift of the TE modes, in contrast to the theoretical greater shift of the TM modes for a homogeneous microsphere. Recent theoretical work has indicated that for higher index layers of increasing refractive index, the TM-to-TE shift ratio decreases below 1 when the high index layer is on the order of 10 to 100 nm.[78] We believe this is the case for our QD/microsphere system, and work continues to fully understand the role of the embedded QD layer and optimize the increased sensitivity.

Excitation Power

It is worth noting that the experiments were conducted using an irradiance of <50 W/cm^2. This irradiance compares favorably to other dye approaches,[22] and previous QD/microsphere work using laser tweezing was employed[42] in which the irradiance is up to 3 orders of magnitude higher. By taking advantage of the high quantum yield of the QDs, the required irradiance was greatly decreased, ensuring a uniform distribution across the microsphere and enabling the simultaneous use of multiple microspheres. The low irradiance also introduces the potential to work in turbid environments in which the delivered light is attenuated and/or diffuse. Lower irradiance also decreases the photobleaching rate and increases the viable lifetime of the sensor.

Conclusions

We have demonstrated a remote, refractometric sensor based on the spectral shift of WGMs within QD-embedded polystyrene microspheres using continuous wave excitation. WGM spectra appear to be stable over time if the laser irradiance is limited, highly visible, and perturbed by changes in the refractive index of the surrounding media. WGM shifts due to changing refractive index are sensitive, reversible and show an enhancement over basic theoretical calculations. These sensors show great potential as highly-sensitive, micro-scale sensors for biological applications.

To better understand the enhancement in sensitivity we observe from these microspheres, these empirical results will be used in the next chapter to understand the role of the embedded QD layer. Enhancement of the sensitivity as well as dependence of the WGMs spectra on the QD layer will be examined to lead to a further investigation into the ability to detect biological analytes, both in bulk solution and when bound to surface chemistry.

CHAPTER VI

MODELING THE WHISPERING GALLERY MODES IN QUANTUM DOT EMBEDDED MICROSPHERES

Introduction

Previously, we have examined the sensitivity of WGM QD-embedded polystyrene microspheres due to both bulk index changes and changes due to adsorption of protein on the microsphere surface.[95, 104] We have demonstrated an approximate 2X enhancement in sensitivity of the microspheres due to these changes in refractive index over a homogeneous polystyrene microsphere. Thus far, we have speculated that the increase in sensitivity was due to the layer of embedded QDs in effect creating a high index outer layer. In this work, we will examine the thin, high index layer to more accurately model the WGM resonances from our experimentally obtained spectra. Second, we will establish a more accurate understanding of the effects of an embedded QD layer or other high index outer layer on the WGM resonance location and sensitivity for future low-Q WGM applications.

Experimental Methods

Confocal images of the microspheres show the QDs are confined to the outer edges of the microsphere but the penetration depth is below the resolution of

microscope; thus, the penetration depth is believed to be less than 122 nm into the polystyrene.[95] Studies by Gao and Nie have also found that the QD penetration depth in polystyrene microspheres swollen with 5% chloroform is limited to 10-20 nm below the surface.[92] A TEM image of a micro-tomed section of the microsphere confirming that the QDs are confined to the outer edges of the microsphere is included as Figure 6.1.

WGM resonance theory was discussed in Chapter III. Using this theory, resonance conditions and expected sensitivity for each case of microsphere are solved numerically, bounded by $k = \frac{l + 1/2}{m_1 a}$ and $k = \frac{l + 1/2}{a}$.[27] C++ code used for these calculations is included in Appendices C, D and E. For most calculations, our polystyrene microspheres are assumed to have a 4.8 μm average radius and refractive index of 1.587 at 550 nm.[105] As the model results for the WGMs will be compared to the spectra obtained experimentally as a function of wavelength, we have chosen to display most results as a function of wavelength rather than wavevector. In the cases where the size of the microsphere changes, the mode numbers have been adjusted to provide resonance modes around our QD emission peak of 550 nm for consistency in comparison to the experimental results.

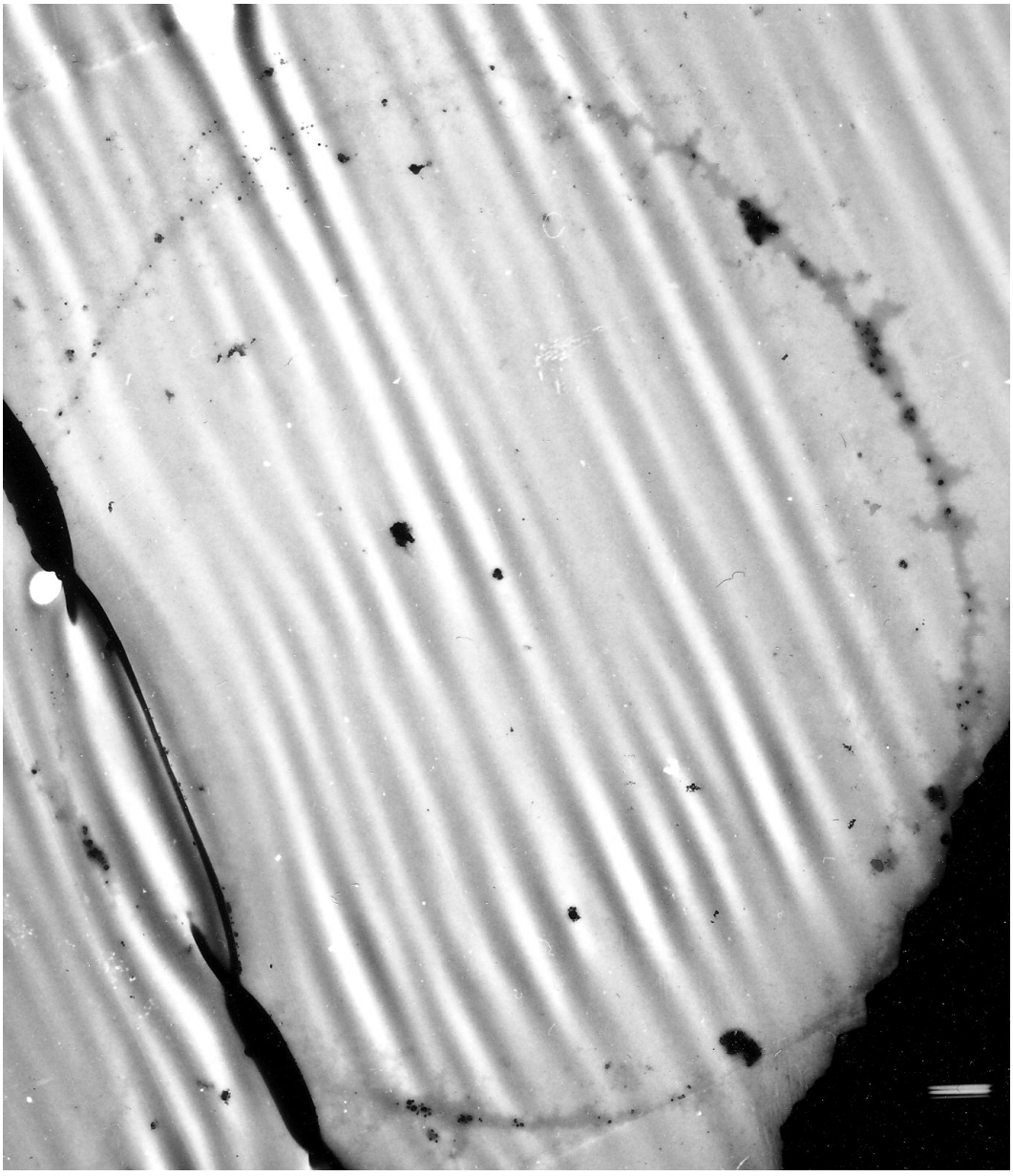

Figure 6.1: TEM Image of a Micro-Tomed Section of a Microsphere. TEM image of a micro-tomed section of an QD-embedded microsphere demonstrating that the QDs are confined to the outer layer of the microsphere. The white bar in the bottom right corner is ~ 2 µm.

Modeling the Experimental WGM Locations

Representative WGM spectra obtained from the same batch of sulfate microspheres (radius 4.8 μm with a standard deviation of 0.35 μm) are shown versus wavelength in Figure 6.2. The microspheres used in these samples are all from the same original sulfate microsphere batch and have been embedded with QDs using the same procedure. The only variations between the samples were the concentration of QDs and/or the amount of time the spheres set in water after being embedded with QDs. Microspheres producing the spectra a) and d) were from the same embedding sample. However, d) was used immediately after embedding and subsequent transfer to water, while a) remained in water for one week. Microspheres b) and c) were exposed to 75% of the QD concentration of a) and d). Microsphere c) was used within a few hours after embedding, while b) remained in water two days.

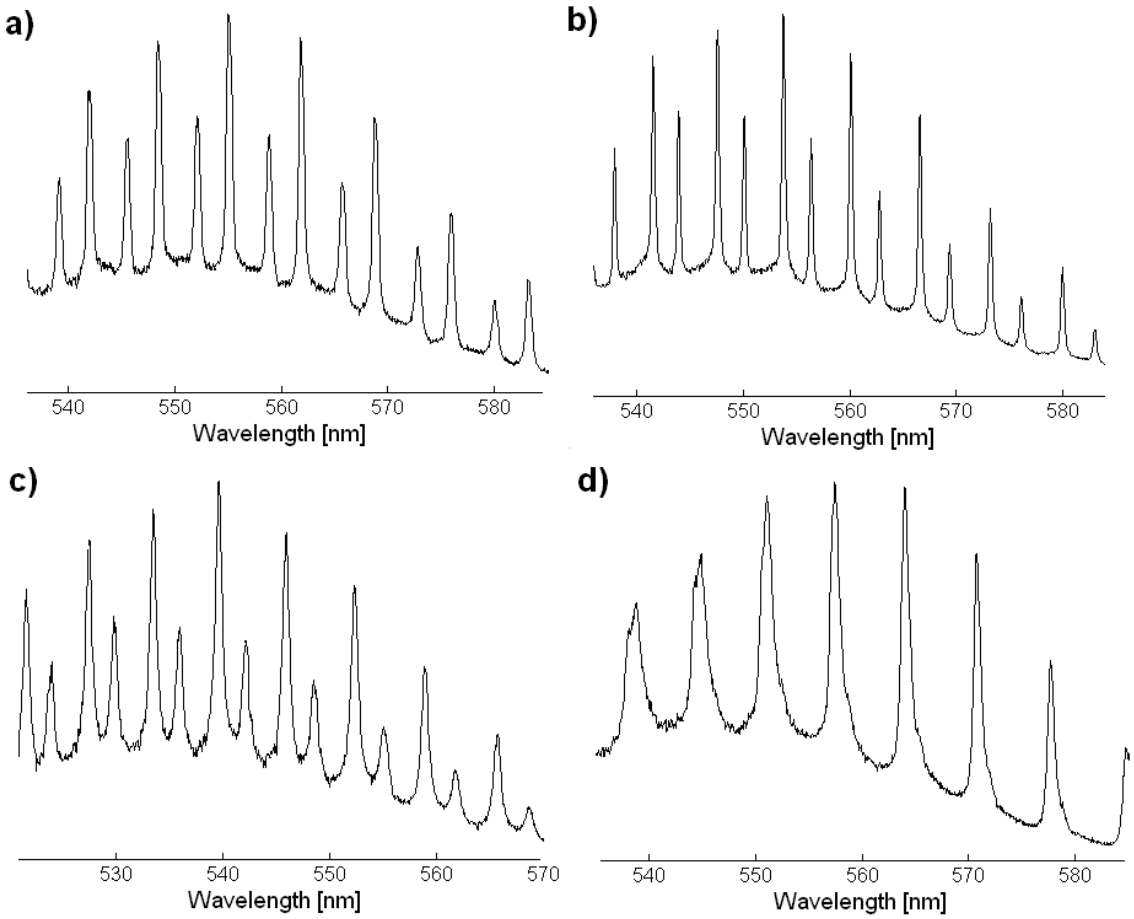

Figure 6.2: Various WGM Spectra from the Same Batch of Microspheres. Various WGM spectra from a 4.8 µm batch of QD-embedded polystyrene microspheres demonstrating different spacing of TE and TM resonances. The TE peaks are indentified as the larger in the pair of modes. In spectrum d), the TE-TM modes are overlapped to produce one single peak.

The position of the WGM modes differ significantly between microspheres. In the majority of the spectra, pairs of first order TE-TM modes are visible as expected. In Mie scattering, TE modes typically have higher Q-factors; this assumption was verified by calculating the linewidth from the Mie coefficients. Thus, the peaks having the largest Q (typically the higher intensity) are considered the TE mode. When the angular mode numbers are equal, the TE modes are at slightly lower frequencies (longer wavelength) than the TM modes. In spectrum a) the spacing between TM and TE modes with the same angular mode number is closer than the spacing between the neighboring mode pairs, as would be expected from Mie theory for these sized microspheres. In spectrum b) the spacing of the modes is shifted so that the TE modes are now closer to the TM modes of lower angular mode number than those of the same number. This trend continues in spectrum c) until by spectrum d), the typical pair of TE and TM peaks is not visible and only one peak appears. It is believed that this single peak is due to an almost complete overlap in the resonance position of the TE and TM modes for these particular spheres. It can also be seen that the peaks in this spectrum broaden significantly at shorter wavelengths, demonstrating the likelihood of two separate peaks moving out of complete overlap.

Polystyrene microspheres are polydisperse (4.8 ± 0.35 μm) making it difficult to determine the exact size of an individual microsphere. Thus, we must first determine that the variation in these spectra are not due to differences in microsphere size alone. WGM resonance locations are directly related to the Mie scattering of a homogeneous microsphere; thus, the locations of the modes without the high index layer should be

roughly equivalent to the resonances in the spectra for Mie scattering efficiency. Figure 6.3 shows the theoretical Mie scattering for the average and one standard deviation above and below the average sized polystyrene microspheres in water. As shown in these spectra, the spacing between the modes overall decreases as is expected with an increase in microsphere size, along with an increase in Q-factor of the modes. There is however, no significant shift in the relative spacing within TE-TM pairs of modes and between neighboring pairs. Thus, these spectra also indicate that it is unlikely that the changes we saw in mode spacing for our QD-embedded microspheres are due to size changes alone.

Additionally, it is unlikely that the differences observed in these spectra for our microspheres is due to flattening or distortion of the shapes of the microspheres. For spherical microspheres, modes of different azimuthal index, or inclination from the equator, are assumed to be degenerate. If the microspheres were elliptical, the various azimuthal modes would appear as nondegenerate modes around the spherical resonance position. We believe we have seen the results of this effect as broadening of the linewidths of the modes in other WGM spectra (not shown). However, we do not believe these distortions to have caused all the differences in spectra, in Figure 6.2, as the Q-factors remain fairly consistent between spectra, despite the resonance location.

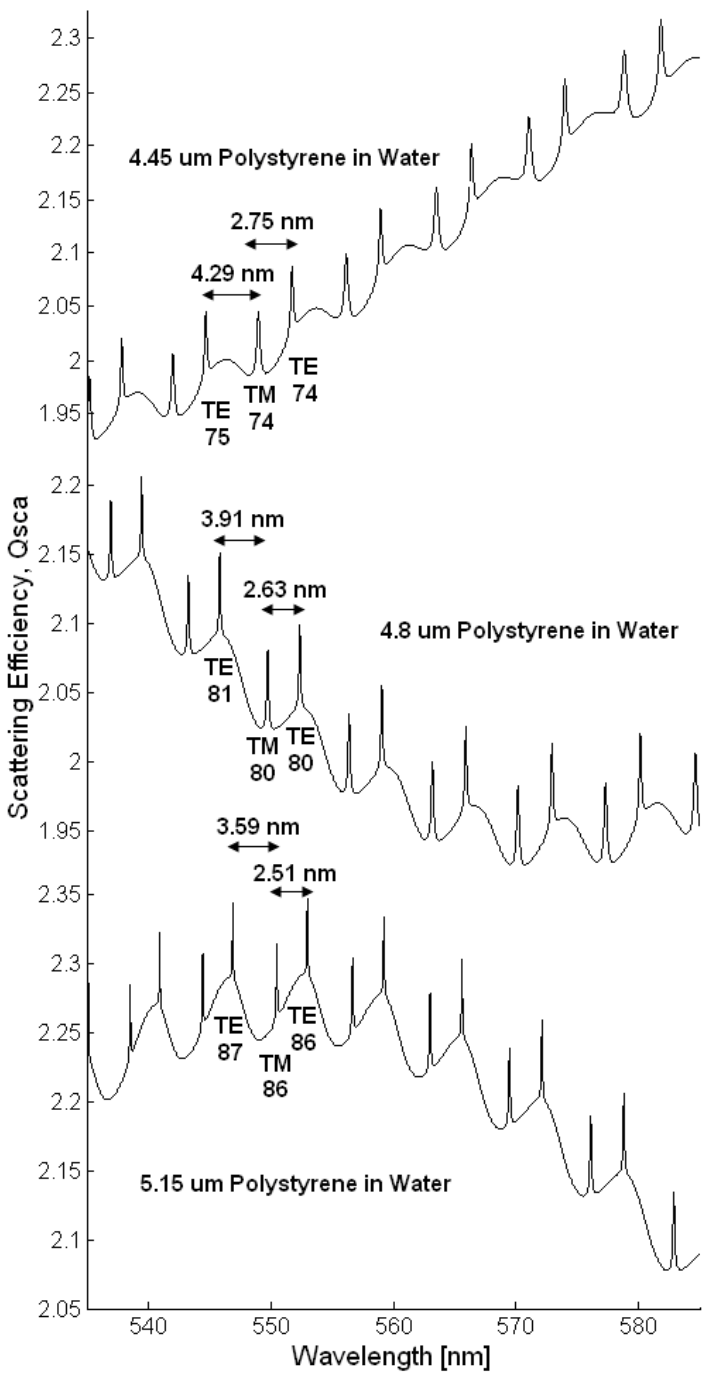

Figure 6.3: Mie Scattering Efficiency for Micropsheres Spanning our Distribution. Mie scattering efficiency for polystyrene microspheres in water spanning one standard deviation above and below the average microsphere size. The spacing within and between pairs of mode decreases with increasing microsphere size.

Single High Density Layer

Confocal[95] and TEM[92] images have demonstrated that the QDs are embedded in the periphery of the microspheres to a depth of <100 nm. Thus, we believe that the QD layer may act as a single high index outer layer on the microsphere. CdSe has an RI of ~2.8 at 550 nm.[106] The refractive index in the high index layer will vary with the density of the QDs embedded in the polystyrene. Thus, a range of possible refractive indicies are examined; for comparison purposes a refractive index of 1.9 (~25% QDs) will be used. Teraoka et al. have explored the effect of a high index layer on the locations and sensitivity of WGMs; however, the calculations involved a much larger (100 μm radius) microsphere with generally much thicker layers for polymer coatings lower than our estimated refractive index for an embedded layer of QDs.[77, 78] Thus, it is necessary to explore this phenomena in order to gain a full understanding of the QD/microsphere system.

Figure 6.4 demonstrates the radial distribution of the TE electric field energy of angular mode l = 80 for a homogeneous microsphere as compared to a microsphere with a 30 nm outer layer consisting of ~25% QDs. As previously mentioned, the addition of the high index layer on the outside of the microsphere pushes the electric field closer to the edge of the microspheres, intensifying the evanescent field. Additionally, this shift in energy closer to the edge of the microspheres essentially increases the pathlength of the mode, thus increasing the resonant wavelength for the same mode number.

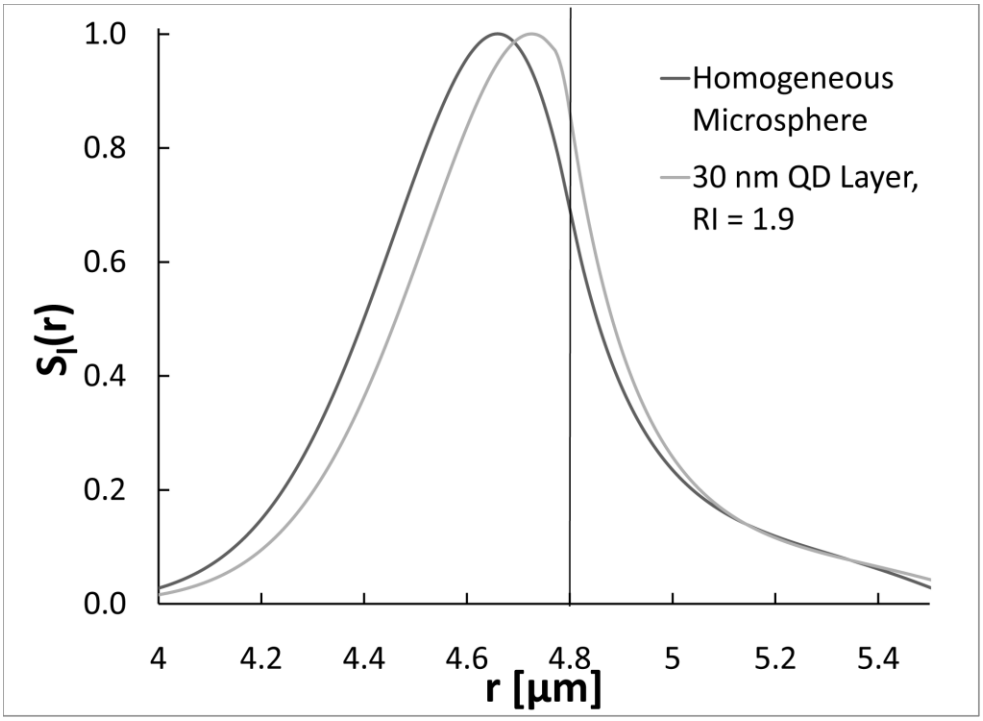

Figure 6.4: TE Radial Function with and without the QD Layer. TE radial function for a 4.8 µm radius homogenous polystyrene microsphere and a 4.8 µm radius polystyrene microsphere embedded with a 30 nm QD outer layer consisting of approximately 25% QDs. The high index outer layer pushes the radial function closer to the microsphere surface, intensifying the evanescent field. Additionally the effective pathlength is lengthened, which increases the resonant wavelength for the same mode number.

The degree of this shift in mode location is demonstrated in Figure 6.5 as a function of QD layer thickness for various possible refractive indices for the QD layer. It is easily seen that the tangentially polarized TE modes display a greater sensitivity in terms of mode location on the addition of the high index layer than the radially polarized TM modes. Teraoka and Arnold have theorized that the differences in the shift of the wavevectors for TE and TM modes with the addition of a high index outer layer is due to

the differences in boundary conditions.[78] For TE modes, the boundary conditions require continuity of $S_l(r)$ and $S_l'(r)$ at each interface; however, for TM modes $T_l(r)$ and $T_l'(r)/[m(r)]^2$ must be continuous. Thus, a larger layer thickness is required to push the TM mode as close to the microsphere surface as the TE mode.

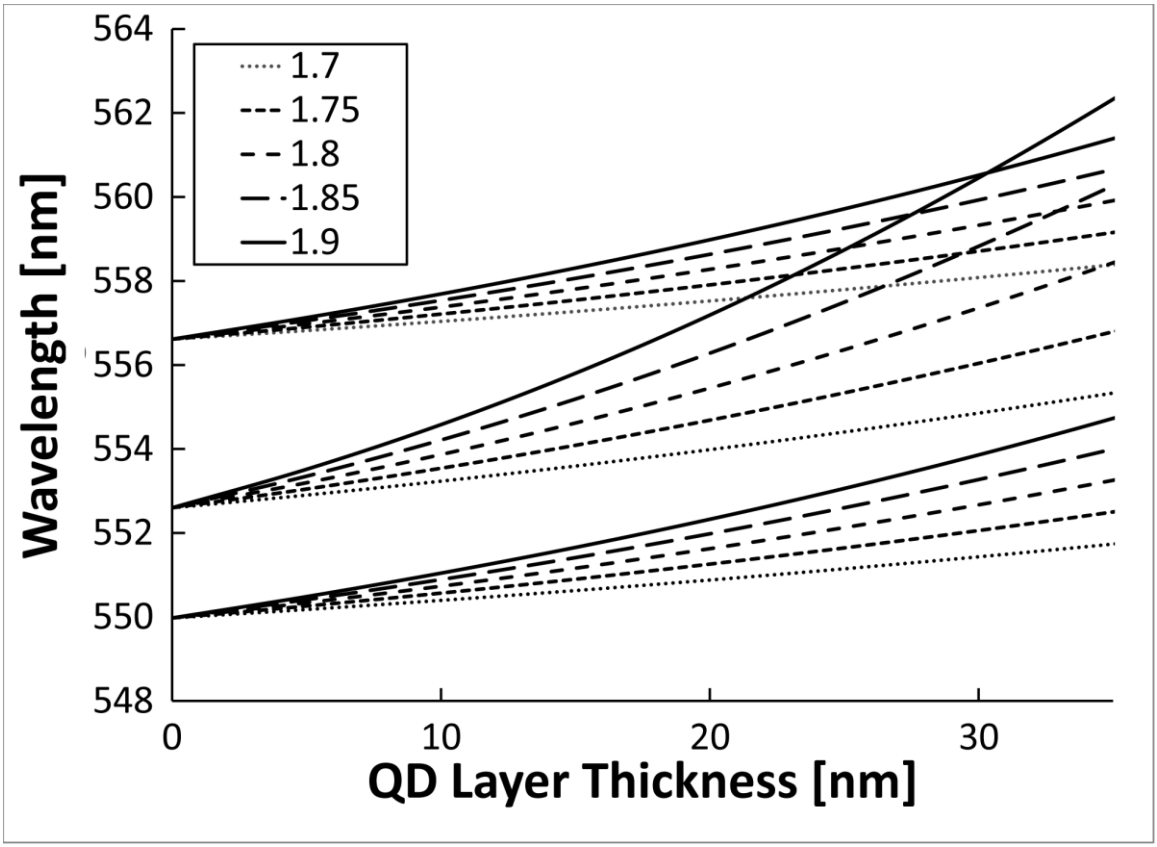

Figure 6.5: WGM Locations with Various QD Layer Thicknesses and Refractive Indices WGM resonance variation with various QD layer thicknesses and refractive indices for a 4.8 μm polystyrene microsphere in water. The positions of the TE modes are much more sensitive to the high index outer layer than the TM modes, thus pushing the TE modes closer to the TM modes of lower mode number. If the QD layer refractive index and thickness are high enough, two modes may actually overlap.

The difference in frequency shift with the higher refractive index outside layer by the TE modes shifts these modes closer to the lower energy TM modes than to the complementary TM modes of the same mode number. At higher layer thickness and refractive indices, the TE modes begin to overlap in wavelength with the lower mode number TM modes. Figure 6.6 shows the values of QD layer refractive index and corresponding thickness that will produce overlapping TE_l and TM_{l-1} modes (spectrum a) for microspheres within our size distribution. For the different sized microspheres, the mode numbers have been adjusted to produce modes at the same general resonant wavelengths (~550 nm). The relationship between QD layer thicknesses and refractive indices producing the same WGM spectra is altered only slightly by varying the radius of the microsphere. This effect indicates the spectra are more dependent on the number of QDs embedded and their penetration depth than the actual microsphere size. These theoretical values fall within our initial estimates of QD penetration depths (<100 nm) and concentration (<~25% or m_3=1.9). The required combinations of refractive index and thickness necessary to produce an overlapping of TE and TM modes can be compared with the parameters capable of producing the mode spacing in Figure 6.6b). In this spectrum, both the TE and TM modes are clearly visible.

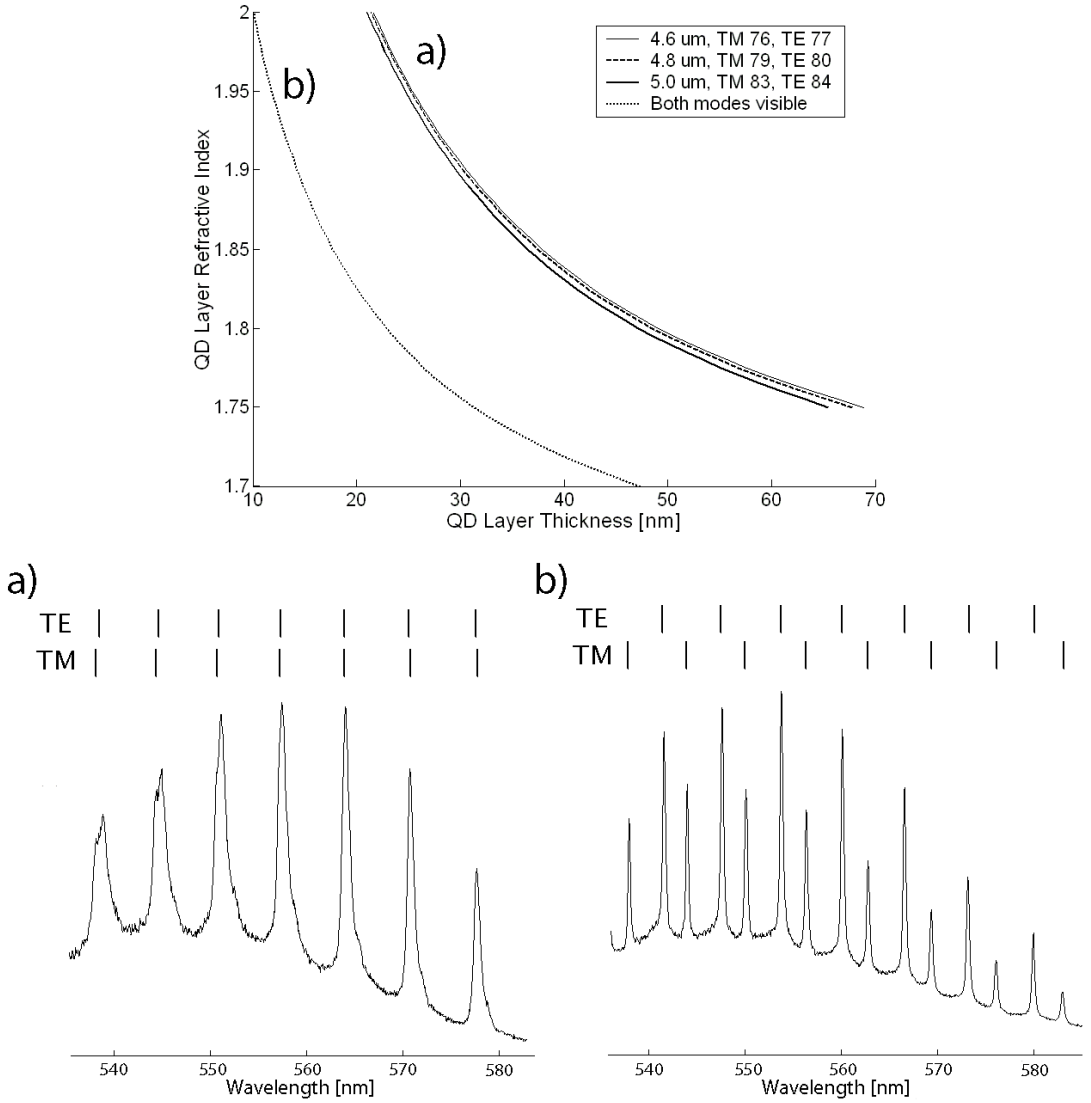

Figure 6.6: Possible QD Layer Refractive Indices and Thicknesses and the Theoretical Fit of the Spectra. Top: Possible combinations of QD layer refractive indices and thickness to produce the indicated spectra. For spectrum a), the size of the microsphere is varied from 4.6, 4.8 and 5.0 μm to demonstrate the limited dependence on layer thickness and refractive index on overall microsphere size for our range of microsphere sizes. Angular mode number was adjusted for these microspheres to produce resonances at the same approximate wavelength. For spectrum b) the microsphere size was 4.8 μm with angular mode numbers of 79 and 80 for TM and TE modes, respectively. Bottom: WGM spectra with the mode positions obtained from the high refractive index model indicated. For a), r = 4.825 μm, m3 = 1.85, t = 37.5 nm. For b), r = 5.01 μm, m3 = 1.7, t = 41.5 nm.

These two microspheres are further fit to specific values for the radius, QD layer refractive index and layer thickness. The spacing between TE-TE or TM-TM modes is first used to obtain a best fit for the radius of the microsphere. This value is then used to determine the possible refractive index and thickness combinations to obtain the TE-TM mode spacing. Finally, these combinations are fit to the experimental WGM positions. The theoretical mode positions obtained from this procedure are indicated above each spectrum. The best fit values for 6.6a), a = 4.825 μm, m_3 = 1.85, and t = 37.5 nm, and for b), a = 5.01 μm, m_3 = 1.7, and t = 41.5 nm. These values fall well within both the specified values for the microsphere radius and our approximations for the QD-layer refractive index and thickness. The theoretically obtained positions also fit the empirically obtained positions within 100 pm across the entire modal spectrum. For the overlapping spectrum, the modes are closely overlapped near the center of the spectrum but begin to separate at higher and lower wavelengths, matching our hypothesis about the observed mode broadening at lower wavelengths.

The specific microspheres used to obtain these analyzed spectra were from the same batch of QD embedded microspheres. However, after embedding, the microspheres demonstrating non-overlapping TE and TM were allowed to set in water for several days, while the microspheres with overlapping modes were used almost immediately. We believe that the tri-*n*-octylphosphine oxide (TOPO) capped QDs should prefer the hydrophobic environment of the polystyrene microspheres and remain embedded indefinitely and we have observed WGMs from embedded microspheres sitting in water for weeks at a time. However, it is likely that a number of the QDs were

loosely confined within the polystyrene matrix and leached out over time. This possibility is supported by the modeling results for the three-parameter system. While the QD layer thickness remains a consistent 0.8% of the total microsphere radius, the refractive index decreases substantially from 1.85 to 1.7. It should be noted that there is a visible decrease in the apparent orange color of the embedded microsphere pellet just after embedding and after sitting in water for a few days.

Refractive Index Sensitivity

Our previous experimental results have shown these QD-embedded microspheres to have a refractive index sensitivity for WGMs around 550 nm of ~100 nm/RIU (refractive index unit) for microspheres developed for continuous wave excitation, approximately 2X the sensitivity predicted for a homogeneous microsphere.[104] Using our QD-layer model, we examined the possible enhancements in sensitivity. Because the sensitivity varies with angular mode number (longer wavelength), the angular mode numbers have been adjusted to provide WGM resonances near 550 nm.

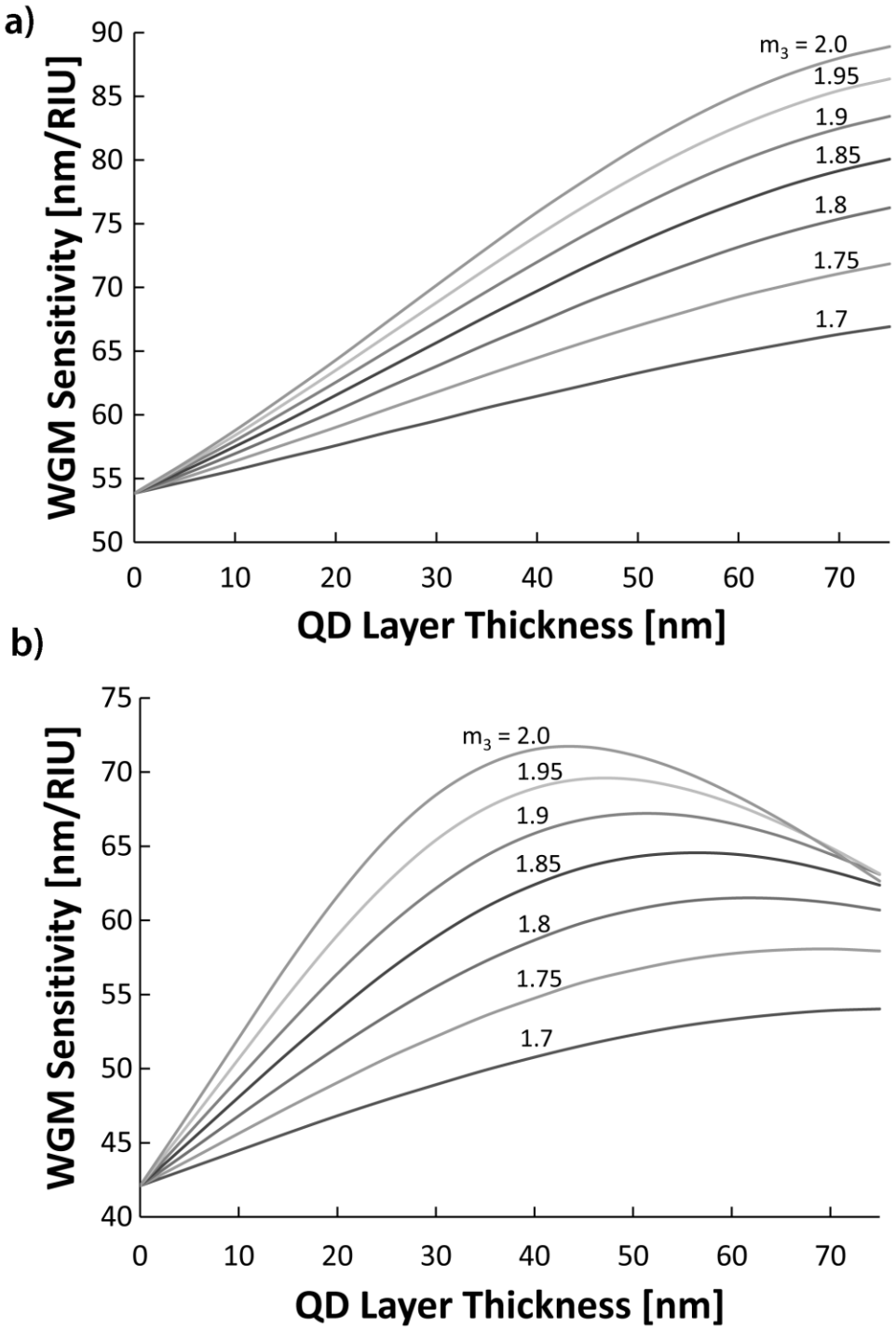

Figure 6.7: Possible Refractive Index Sensitivities. Possible refractive index sensitivities for (a) TM modes and (b) TE modes from 4.8 μm radius polystyrene microspheres with possible combinations of QD layer refractive indices and thicknesses.

Figure 6.7 demonstrates the sensitivity of the QD-embedded microspheres in terms of nm/RIU. The shift in resonance was calculated at slightly higher refractive indices, up to m_2=1.3616 equal to 50% ethanol, and the shift from the resonance at water was determined. TM modes have a higher sensitivity than TE modes and also do not display the same decrease in sensitivity at the higher ends of our thickness range as seen with the TE modes. As the radial function of the TE modes more easily enters into the high index layer it begins to sense the refractive index of this layer at smaller thicknesses than the TM modes. The higher refractive index effectively decreases the phase velocity of the mode, causing the microsphere to appear larger, thus decreasing the refractive index sensitivity at these higher QD layer thicknesses.

The maximum enhancement in sensitivity is below two fold for these microspheres, and far below the approximate eight fold reported for large silica microspheres.[79] However, the microspheres modeled here involved embedding the actual polystyrene microsphere with the QDs. The sensitivity could be further enhanced by coating the microspheres with a separate thin high index layer with QDs embedded in it to bring the effective layer refractive index to an even higher value. Additionally, even with only a maximum two-fold enhancement in sensitivity, the refractive index sensitivity for these 4.8 μm radius microspheres is still higher than the shift demonstrated with an 8.4X enhancement for a 183 μm radius microsphere, although the Q-factors are significantly higher for the larger microspheres.[79]

Using average QD layer refractive index and thickness values of 1.775 and 40 nm to produce modes similar to the ones obtained in the experiments, we obtain

calculated sensitivities of ~66 and ~57 nm/RIU (r = 4.8 μm) for TM and TE modes respectively. This result falls below our previously observed sensitivity of ~100 nm/RIU. There are a few possible explanations for this discrepancy. Although, the refractive index was also based measured polystyrene microsphere refractive index at 550 nm, the refractive index for our particular microspheres could be different.[105] It is possible to get closer to our experimental results by decreasing the size of the microsphere to one standard deviation below the reported average (4.45 μm) and decreasing the refractive index within values found in literature, to 1.56. Using these values, we obtain shifts of ~88 and ~77 nm/RIU for the TM and TE modes, although these quantities do not fit the modal spectra well. A second explanation for the difference between the model and experimental data lies with the choice of solvents. Polystyrene microspheres are not believed to swell in ethanol; however, they do swell in less polar solvents such as chloroform and octanol. By increasing the radius of the microsphere by just 10 nm for the 50% ethanol in water refractive index (1.3616), we obtain a shift equivalent to ~100 nm/RIU, close to our experimental results.

Conclusions

We have demonstrated that an embedded QD layer in polystyrene microspheres may be modeled as a high refractive index outer layer for the purpose of determining the locations of the WGMs and estimating the sensitivity. These results may be useful for other low-Q WGM approaches involving a high index coating for the purpose of

sensitivity enhancement. QDs may also be embedded in the high index outer layer for the dual purpose of increasing the effective refractive index of the layer and serving as a local light source for excitation of the WGMs.

CHAPTER VII

DETECTION OF PROTEIN ADSORPTION WITH WHISPERING GALLERY MODES IN QUANTUM DOT EMBEDDED MICROSPHERES*

Introduction

It has been demonstrated that the WGMs in QD-embedded polystyrene microspheres are sensitive to refractive index changes both internally and in the surrounding medium. A model including the QDs as a higher index shell explained the observed WGM spectral differences and accounted for the increase in sensitivity of our QD-doped microsphere over a homogenous microsphere model. To demonstrate the possibility of using these QD-embedded microspheres for biological sensing, we explore the potential for protein detection through adsorption of the protein to the surface. We postulate that accumulation of protein (through adsorption or antibody-mediated binding) on the outer surface of the microsphere will increase the local index change resulting in a measureable spectral shift. This hypothesis was explored using bovine serum albumin and thrombin as generic model proteins that will absorb to polymer surfaces naturally depending on the pH of the surrounding media. In addition, a two-

---

* Part of this chapter is reprinted from "Whispering Gallery Mode Biosensors Consisting of Quantum Dot-Embedded Microspheres" Beier, H.T., Coté, G.L., Meissner, K.E., 2009, *Annals of Biomedical Engineering* (2009). 37(10), 1974-1983, 2009, with kind permission of Springer Science and Business Media.

layer model was generated to predict the spectral shift and validate the empirical observations.

Response to Protein Adsorption

Bovine serum albumin (BSA) and thrombin were chosen as surrogate proteins due to their different in isoelectric points (pI). BSA has a pI of ~4.8, so it is negatively charged at neutral pH. Thus, we anticipate low adsorption on the negatively charged sulfate microspheres, especially in the presence of the positively charged PEI coating on the coverslip. On the other hand, thrombin has a pI of ~7.1 and is thus positively charged at neutral pH. Here, we anticipate efficient adsorption on the microspheres.

Figure 7.1 shows the average WGM shift in response to the addition of 1 mg/mL solutions of BSA and thrombin to the WGM sensors for representative TE and TM modes. The shift in the WGM can be clearly seen after addition of thrombin as demonstrated in Figure 7.2; the location of these modes quickly level out to $\Delta\lambda_{TM} = 0.4593 \pm 0.0311$ nm, $\Delta\lambda_{TE} = 0.4533 \pm 0.0311$ nm. The BSA modes red-shift only slightly by $\Delta\lambda = 0.0718 \pm 0.0273$ nm. After 15 minutes in each case, a 10 mg/ml solution of the specific protein was added to the flow cell. No significant additional peak shift occurred indicating that the system was saturated. Diffusion kinetics were not examined in this experiment, but it may be possible the microspheres experience increased mass transport per unit area as compared to analyte diffusion to planar surfaces, due to radial (convergent) diffusion to the microsphere surface.[107]

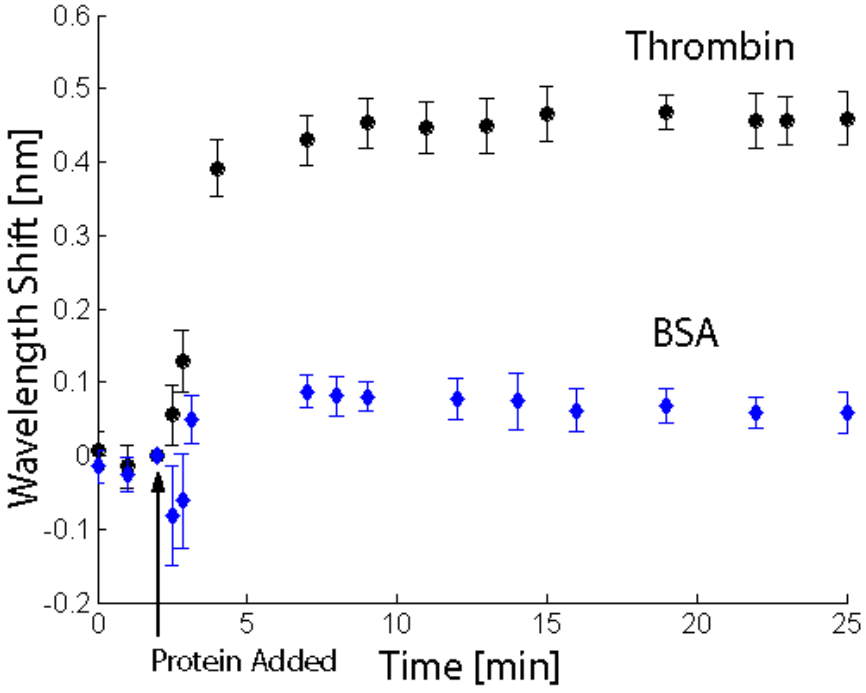

Figure 7.1: WGM Response to Thrombin and BSA. The proteins were added at 2 minutes in each case. All modes were averaged to obtain the shift at each time point; error bars indicate the standard deviation.

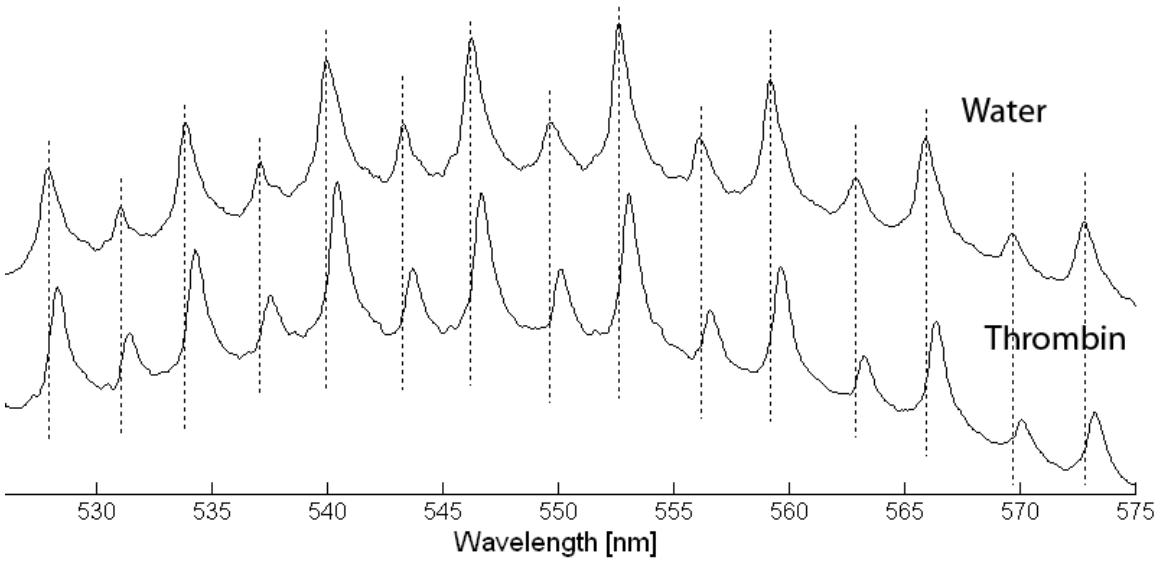

Figure 7.2: WGM Shift with Thrombin. A red shift of an average of 0.4593 nm for each mode in the spectra can be clearly seen as a result of thrombin adsorbing on the microsphere surface.

Comparing the Sensitivity with a Homogeneous Microsphere

The QD/microsphere structure proved to be very sensitive to protein adsorption. The shift caused by the adsorption of protein molecules on the surface of QD/microsphere with a surface density of σ_s, has been calculated for homogeneous microspheres using:[31, 36]

$$\frac{\delta\lambda}{\lambda} \approx \frac{\alpha_{ex}\sigma_s}{\varepsilon_0(n_s^2 - n_m^2)R} \qquad (7.1)$$

where n_s is the refractive index of the microsphere, n_m is the refractive index of the surrounding media, R is the microsphere radius, and α_{ex} is the excess polarizability of the protein. For BSA, α_{ex} has been reported as $\alpha_{ex}=4\pi\varepsilon_0(3.85 \text{ X } 10^{-21} \text{ cm}^3)$ in water.[31, 36]

Using the equation $\frac{\alpha_{ex}}{4\pi\varepsilon_0} = \frac{n_m}{2\pi}\left(\frac{dn}{dc}\right)m$, where $\frac{dn}{dc}$ is the differential refractive index of a solution of protein in water, ~0.184 cm^3/g, and m is the mass of a single protein molecule, the excess polarizability for thrombin can be estimated from previous work as $\alpha_{ex}=4\pi\varepsilon_0(2.09 \text{ X } 10^{-21} \text{ cm}^3)$.[31] Surface densities of BSA proteins on silica microspheres have been experimentally estimated as $\sigma_s = 2.9 \text{ X } 10^{12} \text{ cm}^{-2}$.[36] Thrombin has been estimated to occupy an approximate area of 20 nm^2/molecule, for an estimated surface density of $\sigma_s = 5 \text{ X } 10^{12} \text{ cm}^{-2}$.[33] These values have been reported to closely estimate the shift of BSA adsorbed on dye-labeled polystyrene microspheres.[35] For our approach, these estimations give a calculated WGM shift of $\delta\lambda = 0.19$ nm for thrombin, assuming full surface coverage and a 5 μm radius microsphere.

The average observed shift from adsorption of thrombin of 0.4563 nm gives an enhancement of ~2.4X over the theoretical approximation, and equates to a 0.0047 change in refractive index using the sensitivity obtained from our bulk index experiments. This enhancement in sensitivity is similar to the enhancement of ~2.1X we found during the ethanol-water experiments. Differences in the theoretical enhancements between the two approaches may result from the assumption that the microsphere was fully covered with only a monolayer of protein and minor differences between individual microspheres. Additionally, reduction of the bulk index response from dilution of the higher percentages of ethanol with the existing solutions in the flow cell may have attenuated the calculated bulk enhancement. Using our approximate thrombin density of $\sigma_s = 5 \text{ X } 10^{12} \text{ cm}^{-2}$, and wavelength pitch of 0.04 nm, we estimate

the minimum detection limit of our QD/microsphere sensors to be 260 pg/mm^2 for a minimum detectable mass of ~80 fg protein.

By comparing the bulk refractive index changes for protein in bulk solution versus adsorbed to the surface of the microspheres, we find that the bulk index changes are calculated to be ~1.2 X 10^{-4} RIU for an approximate 0.012 nm shift, given the average of 97 nm/RIU sensitivity we found from the bulk index experiments. With a wavelength pitch of 0.04 nm, such a shift in refractive index is below the detection limit of our spectrometer. However, when thrombin adsorbed to the microsphere surface, the shift was 0.4563 nm, an enhancement of nearly 40X. This concept is further illustrated by the small shift observed for BSA, which was not expected to bind as efficiently to the microspheres. As the addition of molecules in bulk solution results in imperceptible WGM shifts, it is likely any observed shift will be due to binding to the surface. Thus, by functionalizing the surface of the microspheres with antibodies, aptamers, or other targets for specific analytes, the sensor can maintain specificity for the target analyte.

Modeling the WGM Shifts from Protein Adsorption Using a Two Layer Model

Multiple Layer Theory

Our results from bulk absorption of proteins to the microsphere surface have demonstrated that the WGMs are sensitive to the adsorption and display a similar increase in sensitivity as with bulk index changes. As the equations used for calculating

expected shift due to protein binding/adsorption are only valid for homogeneous microspheres, we feel it is useful to develop a means of incorporating the high index QD layer into the model. Teraoka and Arnold have previously used a perturbation approach for determining the shift of the WGM resonance by small particles of low density by considering the perturbation in energy over the energy of the WGM.[78, 80] As an alternative, we have chosen to explore the quantum mechanical approach by considering the proteins on the surface as a thin index layer with an effective index of refraction slightly higher than the surrounding medium. Using this approach, we can consider the effective increase in microsphere size the adsorbed layer will have on the microsphere by increasing the radius of the microspheres by the thickness of the layer.

The same method used to calculate the resonances for a single high index layer can be extended for of higher numbers of outer layers. The innermost layer is indicated by a subscript I, the outer layer is indicated by subscript O, and each additional layer is indicated as L. As with the single layer, the radial distribution is described by linear combinations of the Riccatti-Bessel and Riccatti-Neumann functions:

$$S(r)=\begin{cases} A\psi(m_1 kr) & r < a-t \\ C_1\psi(m_I kr)+D_1\chi(m_I kr) & a-t < r < a-t_I \\ \ldots & \ldots \\ C_L\psi(m_L kr)+D_L\chi(m_L kr) & a-t_L < r < a-t_{L+1} \\ \ldots & \ldots \\ C_O\psi(m_3 kr)+D_O\chi(m_3 kr) & a-t_O < r < a \\ B\chi(m_2 kr) & a < r \end{cases} \qquad (7.2)$$

Using the TE boundary conditions require that $S_l(r)$ and $S_l'(r)$ be continuous across each boundary, therefore the coefficients for the innermost layer for the TE modes are calculated as:

$$\frac{C_1}{D_1} = \frac{m_1\psi(m_1k(a-t))\chi'(m_1k(a-t)) - m_1\psi'(m_1k(a-t))\chi(m_1k(a-t))}{-m_1\psi(m_1k(a-t))\psi'(m_1k(a-t)) + m_1\psi'(m_1k(a-t))\psi(m_1k(a-t))} \quad (7.3)$$

With coefficients for each subsequent layer indicated by:

$$z_L = (m_Lk(a-t_L)) \quad z_{L-1} = (m_{L-1}k(a-t_L)) \quad (7.4)$$

$$\frac{C_L}{D_L} = \frac{m_L\chi'(z_L)[C_{L-1}\psi(z_{L-1}) + D_{L-1}\chi(z_{L-1})] - m_{L-1}\chi(z_L)[C_{L-1}\psi'(z_{L-1}) + D_{L-1}\chi'(z_{L-1})]}{m_{L-1}\psi(z_L)[C_{L-1}\psi'(z_{L-1}) + D_{L-1}\chi'(z_{L-1})] - m_L\psi'(z_L)[C_{L-1}\psi(z_{L-1}) + D_{L-1}\chi(z_{L-1})]}$$

Using the above coefficients, the resonance condition can then be calculated by using the following equation:

$$\frac{m_2}{m_3}\frac{\chi'(m_2ka)}{\chi(m_2ka)} = \frac{(C_O/D_O)\psi'(m_3ka) + \chi'(m_3ka)}{(C_O/D_O)\psi(m_3ka) + \chi(m_3ka)} \quad (7.5)$$

These equations were implemented into the C++ program given in Appendix F to solve for the resonance frequency for any number of layers. To demonstrate the effect multiple layers would have on the microspheres, the normalized radial distributions for a homogenous microsphere and several gradients of layers containing a total of 25% QDs for a total thickness of 50 nm are shown in Figure 7.3.

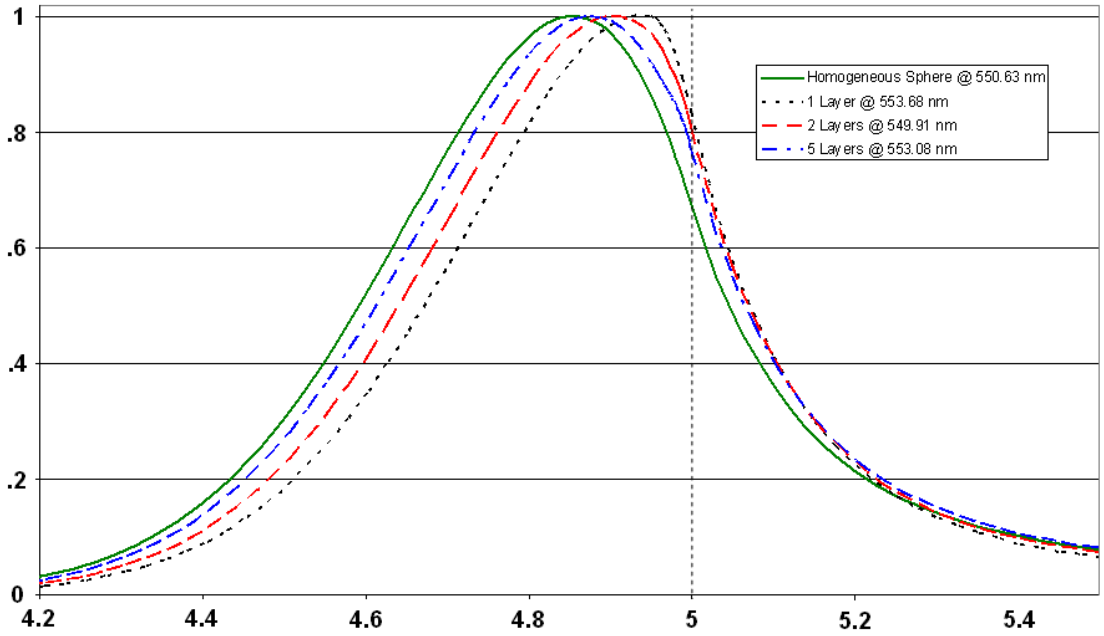

Figure 7.3: Normalized Multilayer Radial Functions. Normalized radial functions comparing a homogeneous microsphere with gradients of layers totally 50 nm and 25% QDs.

Comparison to Experimental Results

The multiple-layer model can be used to calculate the expected shifts due to protein adsorption for our microspheres, given an estimate of the QD layer thickness of 40 nm and refractive index of 1.775 obtained for our previous WGM spectra. Protein refractive index is dependent on its concentration and therefore its density. If the dimensions of the protein molecule and its approximate surface density or related average occupied area per molecule (parking area) are known, the refractive index of and thickness of a monolayer of protein can be estimated from the differential refractive index coefficient.

We empirically obtained an average shift of 0.4563 nm for a saturated layer of thrombin on the microsphere surface. The size of a thrombin molecule is ~4 nm and it occupies approximately 20 nm^2 of area on the microsphere surface, although a more dense packing of ~18 nm^2 has been experimentally obtained.[33] Given the microsphere size and molecular weight of thrombin, the total mass of the thrombin forming a monolayer can be estimated. By assuming that the diameter of thrombin of ~4 nm is equal to the thickness of the layer, the total volume of the thrombin layer can calculated. These results give a total thrombin concentration of 0.75 g/cm^3. The effective refractive index of the thrombin layer is calculated using the differential refractive index, $\frac{dn}{dC}$, for a protein in buffer of 0.182 cm^3/g and equation 7.6.

$$n_p = n_s + \frac{dn}{dC} C_p \qquad (7.6)$$

In this equation, n_p is the calculated refractive index of the protein, n_s if the refractive index of the solvent (1.335 for PBS) and C_p is the concentration of the protein in g/cm^3.

The refractive index of a monolayer of thrombin is then ~1.486. Using this value and the layer thickness of 4 nm, along with the approximate QD layer values of 1.775 and 40 nm, we obtain an estimated shift of 0.385 nm (r = 4.8 μm, l = 80). While this estimate is below our measured shift of 0.458 nm it is much closer than the estimate of 0.19 nm for a homogeneous microsphere. This discrepancy may result from thrombin being more densely packed on the microsphere surface than we estimated, the microspheres being slightly smaller than the average of 4.8 μm or the microspheres having a lower refractive index. If the average area occupied by a thrombin molecule is

lowered to 18 nm^2 as experimentally observed by Zhu et. al,[33] the calculated shift becomes 0.454 nm, essentially identical to our average observed shift.

Additionally in our empirical work, we observed no significant shift due to BSA. We first assumed that this result may have been due the low pI of the BSA limiting its binding to the surface at neutral pH. Additional literature investigations have found studies demonstrating that the binding of BSA on a surface is highly pH dependent.[108, 109] Freeman et. al have theorized that the binding conformations of BSA may be similar to those depicted in Figure 7.4. At pH 7, they found that adsorbed BSA had spread on the surface to produce an 1.1 nm thick layer with an average area of 231 nm^2 per molecule.

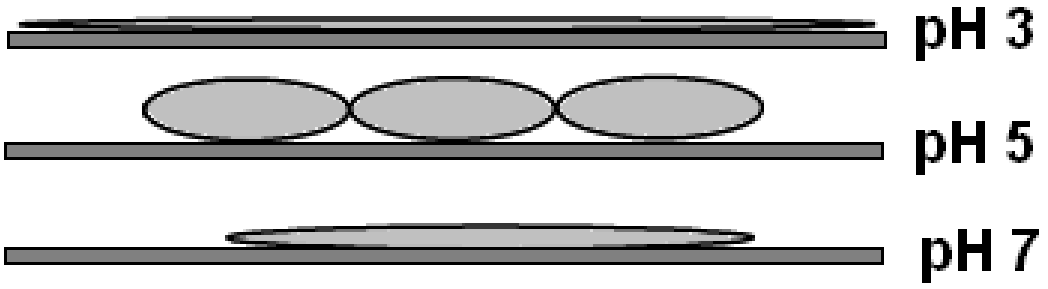

Figure 7.4: Possible BSA Conformations. Possible BSA conformations when adsorbed on a surface at various pH. (adapted from [109]).

We can use these results to estimate the binding for this conformation of BSA. Given the same sensor parameters as used for the thrombin model, we find that the estimated shift for BSA is 0.066 nm, reasonably close to our observed shift of 0.072 nm. These results are summarized in Table 7.1.

Table 7.1: Comparison of Observed and Modeled Shifts for BSA and Thrombin

	Parking Area	Density	Thickness	Refractive Index	Calculated Shift	Observed Shift
	nm^2	g/cm3	Nm		nm	nm
Thrombin	20	0.75	4	1.486	0.385	0.456
Thrombin	18	0.83	4	1.5	0.454	0.456
BSA (pH 7)	231	0.45	1.1	1.43	0.066	0.072

Conclusions

We have successfully observed WGM shifts due to protein adsorption on the surfaces of our microsphere sensors. By using two proteins with different pIs and binding conformations on the surface, we have shown the ability to detect different conformations or thicknesses of proteins. By comparing our empirical results to a model for a homogeneous microsphere, we obtained similar enhancements in sensitivity as obtained from the bulk index experiments. By modeling the QD-embedded microspheres as a high index layer and the protein adsorption as a second layer on the microsphere we obtain theoretically shifts that very closely match the empirical results.

CHAPTER VIII

SPECIFIC PROTEIN DETECTION WITH WHISPERING GALLERY MODES IN QUANTUM DOT EMBEDDED MICROSPHERES

Introduction

With simple adsorption of protein it may be impossible to determine whether the material causing the perturbation in the location of the WGMs is the target analyte. As a solution, we intended to functionalize the microsphere surface with antibodies specific to our target of interest and determine the ability to detect that analyte. Specificity should be demonstrated by exposing the microspheres to proteins with structures similar to the target analytes and general proteins such as albumin, which may nonspecifically bind to the microspheres. In this chapter, preliminary data showing the feasibility of this work will be given and the problems that must be over come will be discussed.

Myoglobin

Myoglobin has been chosen as a model protein to demonstrate specific protein detection by our microspheres. A heme protein found in cardiac and sketelal muscle, myoglobin is indicative of muscle damage and is the first protein found in blood after myocardial infarction, but is not specific to cardiac damage.[110, 111] However, while

creatine kinase (CK-MB) and cardiac troponins I and T (cTnI, cTnT) are more specific to cardiac damage, these markers do not demonstrate an elevation in levels until 4-6 hours after symptom onset, with a peak in levels from 12 to 24 hours. Thus, the ability to monitor myoglobin, may aid in providing a more accurate diagnosis of acute coronary syndrome[110-113] Reported cut-offs for normal myoglobin values used to differentiate acute myocardial infarction from minor injury are 100-200 ng/mL.[114]

Biosite Diagnositics Triage Cardiac Panel, one of the more successful commercial biosensing devices used to detect myoglobin concentration, is based on detection of a fluorescent signal.[115-117] This device is a point-of-care system for diagnosing acute coronary syndromes. Detection of the analyte uses a two-site sandwich assay approach in which a capture and detecting antibody bind to different epitopes on the analyte.[118] In this device, blood from the patient (2-3 mL) is separated from the whole blood by a filter. Then the plasma is then driven by capillary force through a reaction chamber where the analytes bind to fluorescent antibody conjugates. The bound analytes are then captured in specific locations in the device by immobilized antibodies. The concentration of each analyte is measured as a function of the fluorescent signal. The fluorescent dyes are a fluorescence resonance energy transfer (FRET) pair incorporated into latex particles; one dye has an excitation of 670 nm and the acceptor has an emission at 760 nm.[117]

The Triage Cardiac Panel compares the fluorescent signal to a calibration curve but seems to typically produce a binary response indicating whether the analyte is over a certain threshold (0.4 ng/mL for cardiac troponin I (cTnI), 4.3 ng/mL for creatine kinase

(CK-MB), and 107 ng/mL for myoglobin). The lowest detectable limits for these analytes have been reported as 2.7 ng/mL for myoglobin, 0.75 ng/mL for CK-MB and 0.19 ng/mL for cTnI.[116] Thus, assuming these concentrations are based on the initial volume of blood, the mass detection is limited to 100s of pg.

More quantitative detection is likely limited in this device. Dyed latex particles are likely used to provide more fluorescent dye molecules per antibody than direct labeling of the antibodies with the dye would provide. Thus, the intensity fluorescent signal is dependent on the concentration and the concentration ratio of the two dyes within the particles, the FRET efficiency between the dye pair, spatial locations of the dyes and possibly inter-filter effects that may occur at higher dye concentrations. As an intensity-based measurement, the signal is dependent on any intensity fluctuations from the source, slight changes in pathlength and any differences in the absorbance or scatter in the plasma. Additionally, the size of the latex particles is not reported, but it is possible that the size of the particle may limit the number of antibodies capable of being detected in a given area.

Modifications to the Optical System

As the WGM mode shift we found in the previous chapter were within only a few pixels of our baseline, the resolution of our previous optical set-up had to be improved. The spectral resolution of a CCD-based spectrometer is determined by its focal length, the pitch of the grating and the pixel pitch of the CCD array. Of these, the

most viable option was to change the grating. The highest groove density of our original system was 1200 g/mm with a pixel pitch of 0.046 nm. Thus, we added a 2400 g/mm grating (holographic VIS optimized) with a pixel pitch of 0.016 nm to our spectrometer.

While this change was successful in improving the resolution of our system, as demonstrated by the spectra in Figure 8.1, it did introduce some challenges. As previously discussed, we have observed some blue shifting in the location of the modes as excitation irradiance increases or over time with higher irradiance levels. We had been controlling this issue by minimizing the power or maximizing the spot size at the sample, while still obtaining sufficient signal-to-noise to clearly observe the WGMs. However, with the higher resolution grating, the modes are now dispersed over 2.875 times the number of pixels as compared to the 1200 g/mm grating. (Dispersion of 1200 g/mm = 2.3 nm/mm, 2400 g/mm = 0.8 nm/mm, CCD pixel pitch = 20 μm.) Additionally, the average efficiency of the new grating is only 60% of aluminum, as compared to close to 90% with the 1200 g/mm grating. Thus, we found that we had to increase the excitation irradiance and integration time in order to obtain a high enough signal to clearly distinguish the modes.

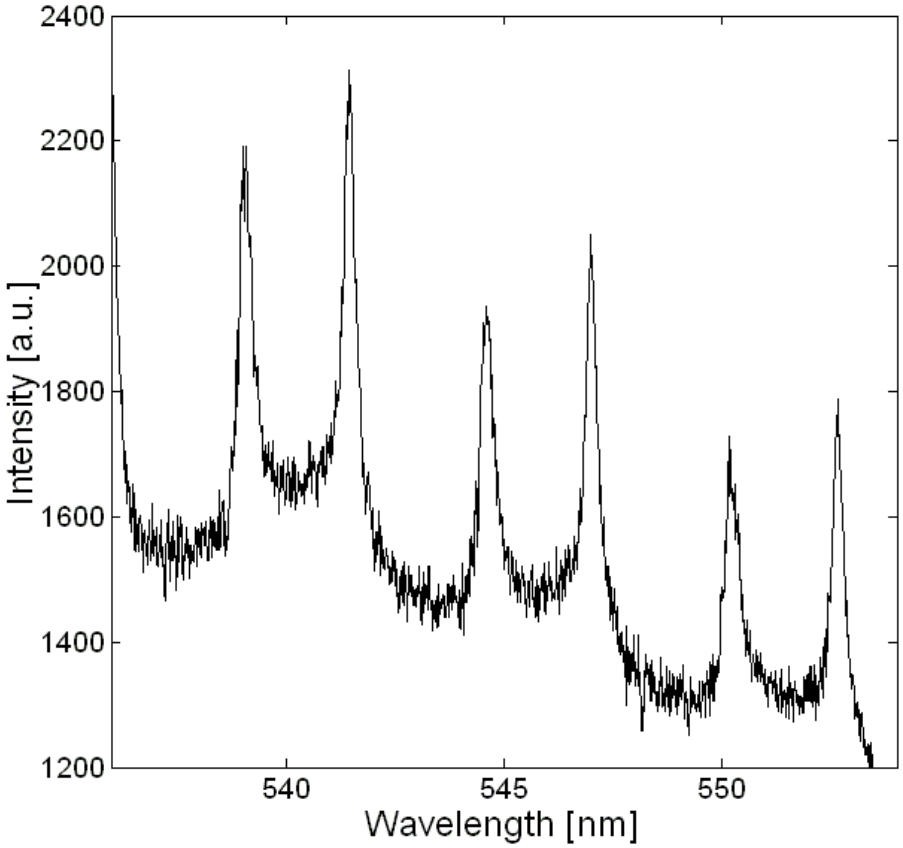

Figure 8.1 WGM Spectra from the High Resolution Grating.

The problem with noise was partially overcome by fitting each individual WGM to a Lorentzian distribution. The probability distribution function for this distribution is given as:

$$P(x) = \frac{1}{\pi} \frac{b}{(x-m)^2 + b^2} \qquad (8.1)$$

In this equation, b is the half width at half max and m is the median. Individual peaks are fit to this distribution by multiplying the function by the total peak area. First, the center position of the each WGM peaks is found by using the custom peak finding program in Appendix G. This value is used as the starting point for the median of the distribution. The peak and surrounding background are selected from the data and baseline corrected. The peak is then integrated to obtain a starting value for the area. These two calculated values, along with an estimate of 0.1 for the half the linewidth, are used as starting points for fitting the data to the distribution using a least squares method. An example WGM peak from the high resolution grating fit to this distribution is given in Figure 8.2. The resulting coefficients of this distribution best-fit approximation of the spectral location of the WGM (m), the mode linewidth (2*b) and the peak area. This method may also improve the resolution of the system and minimum detectable shift by allowing for a more accurate calculation of the peak positions than obtainable from the pixel pitch alone.

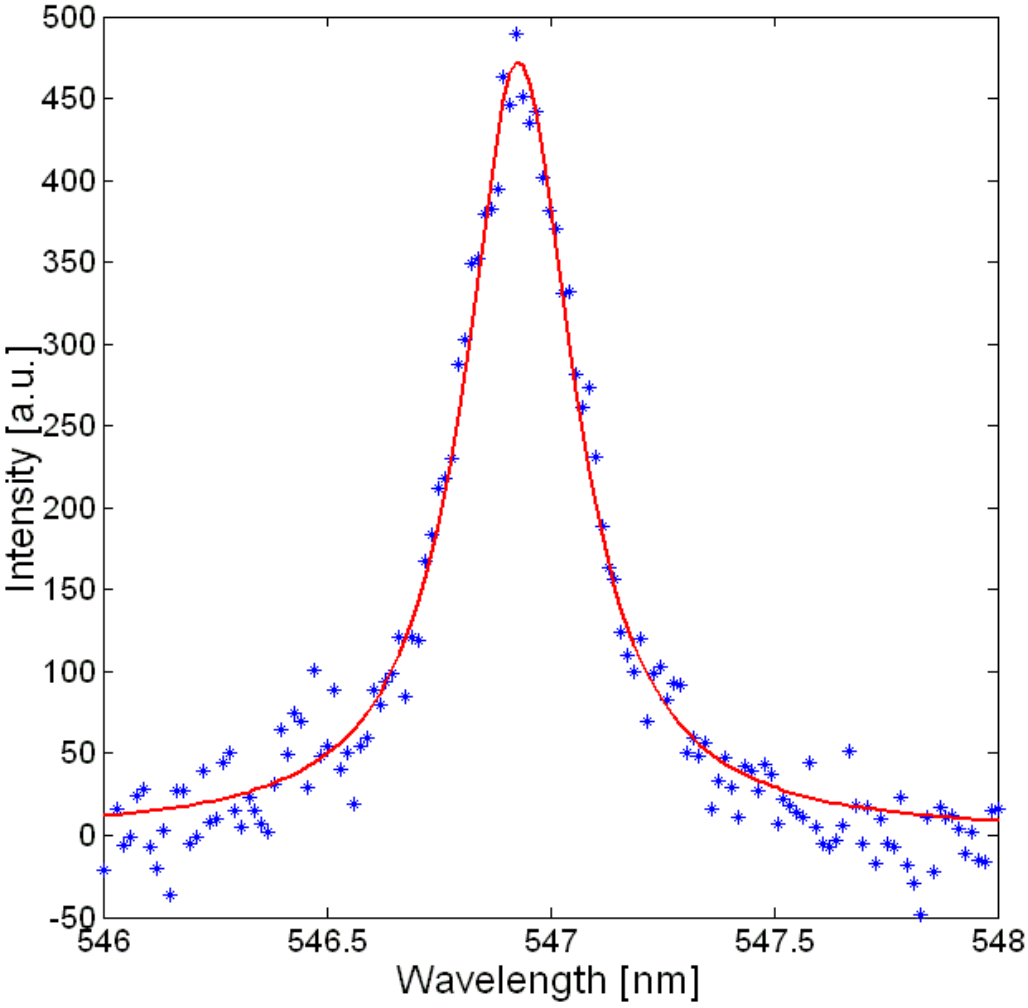

Figure 8.2: Lorentzian Distribution Fit of a WGM Peak. Lorentzian distribution fit of a WGM peak obtained on the high resolution grating.

Despite this improvement in peak identification, we were still hampered by blue shifting of the modes over the course of our experiments. It is quite possible that these problems existed during our initial studies but due to the lower spectral resolution were not detected or simply attributed to pixel noise. Polystyrene has a negative thermal-optical coefficient, meaning its refractive index decreases with increasing temperature. Thus, we believe heating of the microspheres may play a large role in this problem.

As a solution, we further modified the optical system to use a Ti:Sapphire femtosecond laser as our excitation source instead of the previous continuous wave argon laser. After pulse picking at 5 MHz, the beam was frequency doubled by a tunable SHG crystal to wavelengths ranging from 400 to 450 nm. It is postulated that the low duty cycle of the femtosecond excitation will give allow the microsphere to cool between excitations. While this change in excitation did diminish the shifting problem, it did not completely eliminate it.

It was however, discovered that by pre-exposing the microsphere to a higher laser intensity for several minutes and then lowering the excitation power that the blue shifting in the modes is diminished. Figure 8.3 demonstrates the differences in WGM mode shift for microspheres excited with the same irradiance (~8 W/cm^2), with and without pre-exposure. The bottom plot corresponds to a microsphere pre-exposed to a 50% increase in laser fluence (~12 W/cm^2) for 5 minutes. The top plot corresponds to a microsphere that was not pre-exposed and demonstrates an over 2X increase in shift. The mechanism for this phenomenon is not currently understood. More studies need to be performed to fully characterize the effect and optimize the exposed power and/or

duration to further reduce the blue-shifting. The blue-shifting problem may additionally be improved by using a laser source with a higher repetition rate or longer pulse width. This change will maintain a low duty cycle but decrease the potentially damaging peak power of each pulse while keeping the average power constant.

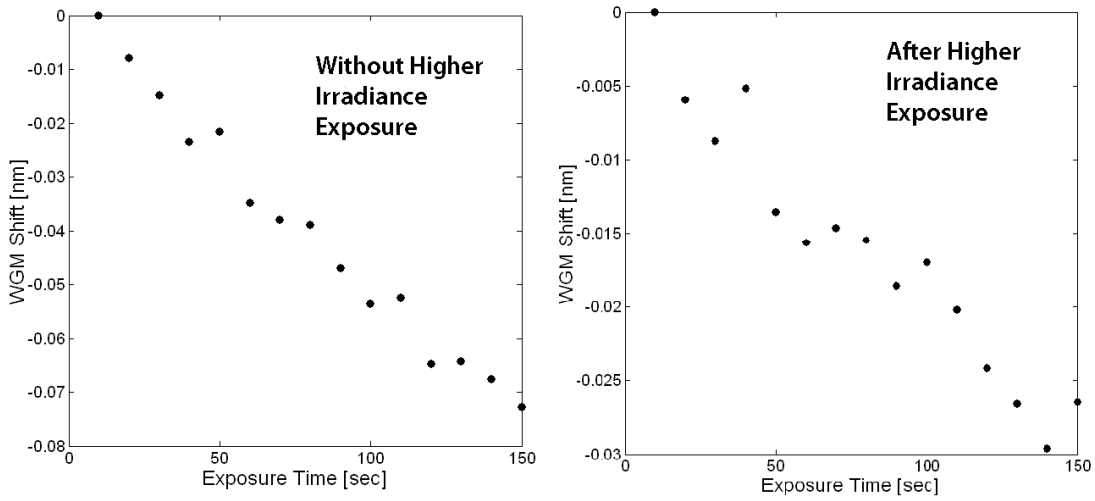

Figure 8.3: Difference in WGM mode shift for microspheres excited with the same irradiance. The bottom plot corresponds to a microsphere pre-exposed to a 50% increase in laser irradiance for 5 minutes. The top plot corresponds to a microsphere that was not pre-exposed.

Antibody Binding to the Microspheres

After it was discovered that by pre-exposing the microsphere to higher laser power that much of the blue-shifting could be eliminated, microsphere functionalization with antibodies could then be characterized. In previous attempts to examine antibody functionalization of microspheres, red shifts were observed but greatly hindered by the competing blue shift. Figure 8.4 demonstrates preliminary results for antibody functionalization of the microspheres. The microspheres were pre-exposed to ~9 W/cm^2; spectra were recorded at ~3 W/cm^2. The carboxyl surface groups on the microspheres had been activated with EDC for 20 minutes before rinsing with PBS (point 0). Polyclonal anti-human antibodies to myoglobin were added in increasing concentrations at the indicated times. Spectra were recorded only every 5 minutes to limit blue-shifting with the excitation beam blocked between scans.

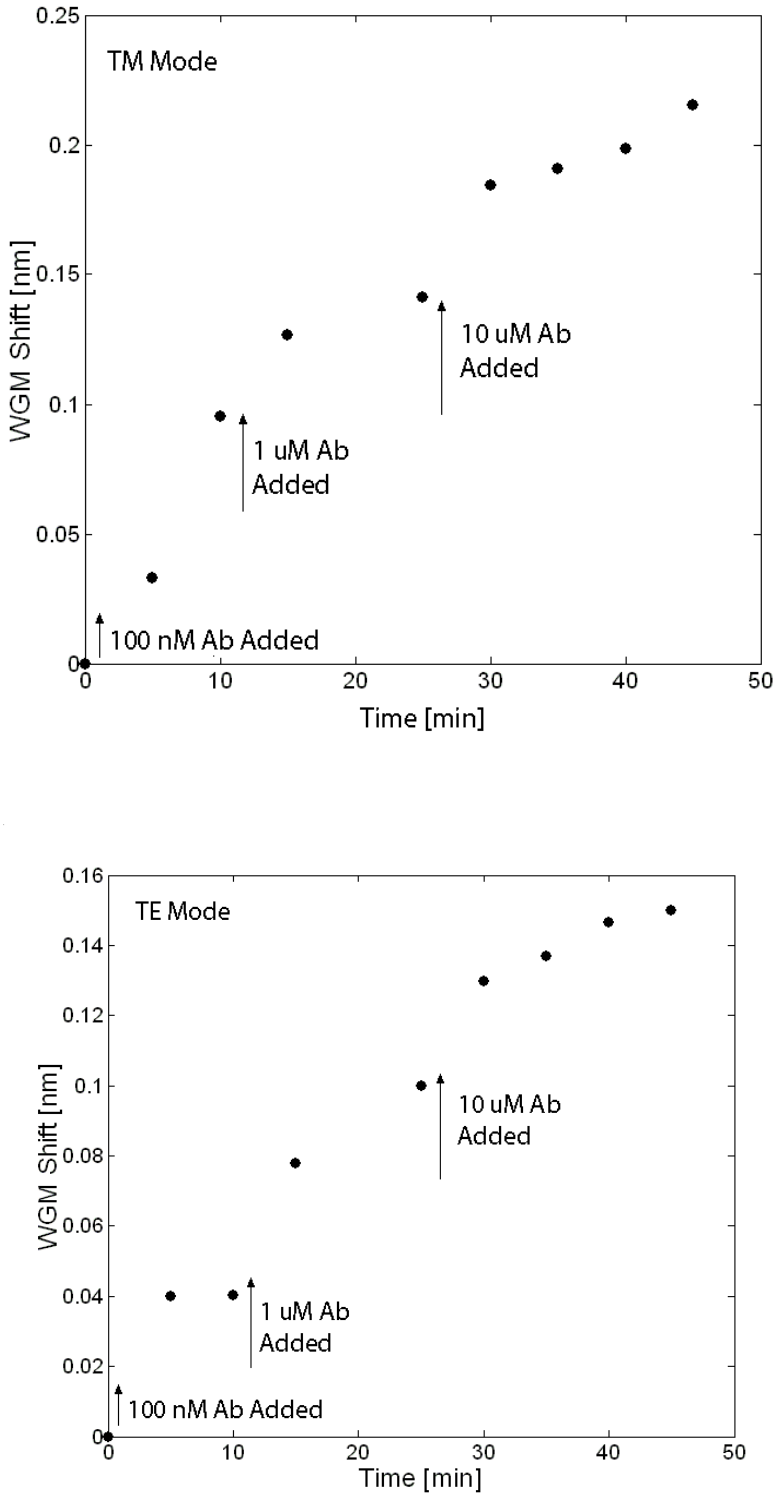

Figure 8.4: WGM Shift from a Titration of Anti-Myoglobin. WGM shift as a function of time for a titration of anti-myoglobin antibodies.

The discrepancy between the empirical and theoretical results have a number of explanations. First, some blue-shifting is likely still being observed, decreasing magnitude of the overall net red-shift. The pre-exposure procedure and the pulse width or repetition rate should be optimized to limit the blue-shifting. Second, the theoretical shift assumes full surface coverage. The WGMs displayed a relatively large wavelength shift after each addition of a higher concentration of antibody; thus, the antibody concentrations may initially be too low. The concentrations may need to be increased or higher concentrations of antibodies may need to be added earlier, when more NHS-esters are still active on microsphere surface, to covalently bind the antibodies and prevent de-adsorption. Additionally, the WGM shift was still increasing at the final data points. Future functionalization procedures may need to be run for longer periods to ensure completion.

Finally, the theoretical shift assumes that the IgG is oriented with its F_c portion toward the surface. This orientation has been confirmed for polystyrene particles;[119] however, any proteins bound with their sides oriented toward the surface would decrease the total number of bound proteins and overall layer thickness. Both of these alterations would decrease the WGM shift. A more likely explanation may lie with our buffer pH. Surface coverage has been shown to be optimal for IgG when the pH of the buffer is close to the pI of the antibody. At this point, the protein has a total net charge of zero and repulsion forces between the molecules are limited. While antibody pIs are typically around neutral, they vary from molecule to molecule and may be as low as 5.8.[119] It may be necessary to determine the pI of our specific antibody to optimize surface

coverage. Future studies may consider lowering the buffer pH slightly to determine the effect on the WGM shifts.

Next Steps

Once antibody functionalization of the surface has been successfully demonstrated, sensitivity to myoglobin as well as specificity should be tested. Low (fM-nM) concentrations of the protein should be flowed across the microspheres and the shift in the WGM should be monitored at each concentration. The sensors will then be tested for sensitivity for hemoglobin, a protein similar in structure to myoglobin, and albumin, a common plasma protein. If non-specific binding is found to be a problem, the sensors may be pre-treated with albumin to block the surface before any binding to myoglobin or other bio-molecules.

Conclusions

Specific protein detection using the QD-embedded polystyrene microspheres with myoglobin as a model analyte has been attempted. Demonstration of this detection was however hindered by blue-shifting of the WGMs during exposure, likely due to temperature affects within the polystyrene microspheres. Curve fitting techniques and the switch to pulse-source excitation helped this problem but did not eliminate the issue. Pre-exposure of the microspheres to higher laser irradiance was additionally used to

further correct the issue. This treatment allowed the observation of WGM shifts from the antibody functionalization; however, it is not believed that functionalization was complete. Future studies should focus on eliminating the blue-shifting issue and optimization the surface functionalization of the microspheres. Once these issue are resolved, specific detection can then be explored.

CHAPTER IX

SUMMARY AND FUTURE WORK

Summary

This work served the purpose of exploring the use of QD-embedded polystyrene microspheres for use in sensitive WGM-based sensing applications. A continuous wave optical system was developed to provide overall excitation of single or multiple microspheres and obtain images and WGM spectra from these microspheres. The excitation and emission paths were de-coupled to allow for obliquely-incident, defocused excitation light of the entire microspheres, while still allowing for focused collection of the WGM emission.

The mode characteristics and bulk sensitivity of these microspheres were examined. Refractive index sensitivity was found to exceed that of a homogeneous microsphere. A theory modeling the embedded QDs as a high refractive index layer on the exterior of the microsphere was used to explain the empirical results. This theory was shown to explain the wide variety of WGM spectra observed from the microspheres and provide some explanation of the enhancement in sensitivity.

Molecular sensitivity was then explored through the absorption of two different proteins, thrombin and BSA. These proteins demonstration very different binding characteristics at pH and the differences between the two WGM shifts due to their adsorption was shown. The enhancement in sensitivity was first characterized using an

equation for protein adsorption based on a homogeneous microsphere. The enhancement in sensitivity was found to be similar to the enhancement found for bulk index changes. Since this equation did not sufficiently model our microspheres, the model of the embedded QDs as a high index layer was again employed. A multi-layer microsphere model was used, modeling the QDs as one layer and the adsorbed proteins as a second layer, increasing the size of the microsphere. Using known values for protein distribution on solid surfaces the estimated refractive indices and thickness of the adsorbed protein layer were calculated. These values were used to obtain a theoretical shift for our microspheres that very closely matched the empirical results.

The mass sensitivity of the microspheres for thrombin, using the 0.04 wavelength pitch for the original 1200 g/mm grating, was found to be ~260 pg/mm^2 for a minimum detection of ~ 80 fg. This sensitivity is improved with the addition of the 2400 g/mm^2 grating to ~100 g/mm^2 and 30 fg for a 0.016 nm pitch. Improvement of the resolution of detection system or fitting of the individual peaks could potentially increase the mass sensitivity even further. While the current mass sensitivity per area does not currently approach the sensitivity of WGMs in the larger silica microspheres, the absolute mass sensitivity is much lower. A sensitivity of 6 pg/mm^2 have been reported for silica microspheres.[30] However, the microspheres used in this study were 400 μm in diameter, producing a minimum detectable mass of 3 pg.

The sensitivity of our microsphere is approaching, but not yet equivalent to current SPR sensors, with typical mass sensitivities of 10 pg/mm^2 and a potential mass sensitivity of 6.3 fg.[35] However, these sensors require evanescent coupling from a prism

or grating, limiting their potential applications. The remote sensing version of this technology, LSPR, has been shown to have similar sensitivities as SPR, probe areas as large as 5 mm^2 limit the mass sensitivity to ~250 pg.[17, 35] Sensitivity for this approach may be improved by using a single nanometer-scale particle, but this approach suffers greatly from signal-to-noise issues. Sensitivity for a individual particle has been shown to be ~200 nm/RIU,[17] 2-3 times the refractive index sensitivity of our current microspheres. However, minimum detectable shift for this approach is limited by the broad linewidth for the LSPR extinctions of ~50 nm, as compared to the 0.2 nm linewidth of our WGMs.

Specific biosensing was also attempted but suffered greatly from blue-shifting of the WGMs during exposure. This effect is likely due to temperature induced changes in the polystyrene refractive index so a pulsed laser system was employed. Pre-exposure of the microspheres to higher laser irradiance was additionally found to further correct the issue, but has not fully eliminated it. WGM shifts from the antibody functionalization were observed; however, it is not believed that functionalization was complete.

Future Work

Future studies should focus on eliminating the blue-shifting issue and optimizing the surface functionalization of the microspheres. Once these issues are resolved, specific detection can then be explored. Other materials for the WGM sensors may also be explored. Less temperature sensitive materials would help eliminate the blue-shifting

issue observed with our current microspheres. Higher index materials would also all for a reduction in the microsphere size while maintaining the ability to observe the WGMs. This reduction could further increase the refractive index sensitivity of the sensors. Additionally, coating the microspheres with high refractive index layers embedded with QDs, to further increase the effective refractive index might also be considered to increase the sensor sensitivity.

REFERENCES

1. M. M. C. Cheng, G. Cuda, Y. L. Bunimovich, M. Gaspari, J. R. Heath, H. D. Hill, C. A. Mirkin, A. J. Nijdam, R. Terracciano, T. Thundat, and M. Ferrari, "Nanotechnologies for biomolecular detection and medical diagnostics," Current Opinion in Chemical Biology **10**(1), 11-19 (2006).
2. D. Erickson, S. Mandal, A. H. J. Yang, and B. Cordovez, "Nanobiosensors: Optofluidic, electrical and mechanical approaches to biomolecular detection at the nanoscale," Microfluidics and Nanofluidics **4**(1-2), 33-52 (2008).
3. L. Hood, J. R. Heath, M. E. Phelps, and B. Y. Lin, "Systems biology and new technologies enable predictive and preventative medicine," Science **306**(5696), 640-643 (2004).
4. K. K. Jain, "The role of nanobiotechnology in drug discovery," Drug Discovery Today **10**(21), 1435-1442 (2005).
5. J. Wang, "Electrochemical biosensors: Towards point-of-care cancer diagnostics," Biosensors & Bioelectronics **21**(10), 1887-1892 (2006).
6. X. D. Fan, I. M. White, S. I. Shopoua, H. Y. Zhu, J. D. Suter, and Y. Z. Sun, "Sensitive optical biosensors for unlabeled targets: A review," Analytica Chimica Acta **620**(1-2), 8-26 (2008).
7. A. Q. Liu, H. J. Huang, L. K. Chin, Y. F. Yu, and X. C. Li, "Label-free detection with micro optical fluidic systems (MOFS): A review," Analytical and Bioanalytical Chemistry **391**(7), 2443-2452 (2008).

8. C. C. Wang, R. P. Huang, M. Sommer, H. Lisoukov, R. C. Huang, Y. Lin, T. Miller, and J. Burke, "Array-based multiplexed screening and quantitation of human cytokines and chemokines," Journal of Proteome Research **1**(4), 337-343 (2002).

9. X. D. Hoa, A. G. Kirk, and M. Tabrizian, "Towards integrated and sensitive surface plasmon resonance biosensors: A review of recent progress," Biosensors & Bioelectronics **23**, 151-160 (2007).

10. D. R. Shankaran, K. V. A. Gobi, and N. Miura, "Recent advancements in surface plasmon resonance immunosensors for detection of small molecules of biomedical, food and environmental interest," Sensors and Actuators B-Chemical **121**(1), 158-177 (2007).

11. C. R. Yonzon, D. A. Stuart, X. Y. Zhang, A. D. McFarland, C. L. Haynes, and R. P. Van Duyne, "Towards advanced chemical and biological nanosensors: An overview," Talanta **67**(3), 438-448 (2005).

12. X. D. Hoa, A. G. Kirk, and M. Tabrizian, "Towards integrated and sensitive surface plasmon resonance biosensors: A review of recent progress," Biosensors & Bioelectronics **23**(2), 151-160 (2007).

13. J. Homola, "Present and future of surface plasmon resonance biosensors," Analytical and Bioanalytical Chemistry **377**(3), 528-539 (2003).

14. J. Homola, "Surface plasmon resonance sensors for detection of chemical and biological species," Chemical Reviews **108**(2), 462-493 (2008).

15. J. Homola, S. S. Yee, and G. Gauglitz, "Surface plasmon resonance sensors: review," Sensors and Actuators B-Chemical **54**(1-2), 3-15 (1999).

16. J. S. Shumaker-Parry, M. H. Zareie, R. Aebersold, and C. T. Campbell, "Microspotting streptavidin and double-stranded DNA Arrays on gold for high-throughput studies of protein-DNA interactions by surface plasmon resonance microscopy," Analytical Chemistry **76**(4), 918-929 (2004).

17. A. J. Haes and R. P. Van Duyne, "A unified view of propagating and localized surface plasmon resonance biosensors," Analytical and Bioanalytical Chemistry **379**, 920-930 (2004).

18. R. G. Heideman, R. P. H. Kooyman, and J. Greve, "Performance of a highly sensitive optical wave-guide Mach-Zehnder interferometer immunosensor," Sensors and Actuators B-Chemical **10**(3), 209-217 (1993).

19. J. Ingenhoff, B. Drapp, and G. Gauglitz, "Biosensors using integrated optical-devices," Fresenius Journal of Analytical Chemistry **346**(6-9), 580-583 (1993).

20. G. Gauglitz and J. Ingenhoff, "Design of new integrated optical substrates for immuno-analytical applications," Fresenius Journal of Analytical Chemistry **349**(5), 355-359 (1994).

21. A. Brandenburg and R. Henninger, "Integrated optical young interferometer," Applied Optics **33**(25), 5941-5947 (1994).

22. A. Brandenburg, "Differential refractometry by an integrated-optical Young interferometer," Sensors and Actuators B: Chemical **39**(1-3), 266-271 (1997).

23. V. S. Y. Lin, K. Motesharei, K. P. S. Dancil, M. J. Sailor, and M. R. Ghadiri, "A porous silicon-based optical interferometric biosensor," Science **278**(5339), 840-843 (1997).

24. M. Weisser, G. Tovar, S. Mittler-Neher, W. Knoll, F. Brosinger, H. Freimuth, M. Lacher, and W. Ehrfeld, "Specific bio-recognition reactions observed with an integrated Mach-Zehnder interferometer," Biosensors & Bioelectronics **14**(4), 405-411 (1999).

25. F. Vollmer and S. Arnold, "Whispering-gallery-mode biosensing: Label-free detection down to single molecules," Nature Methods **5**(7), 591-596 (2008).

26. J. W. S. Rayleigh, "The problem of the whispering gallery," Philosophical Magazine **20**, 1001-1004 (1910).

27. B. R. Johnson, "Theory of morphology-dependent resonances - shape resonances and width formulas," Journal of the Optical Society of America A-Optics Image Science and Vision **10**(2), 343-352 (1993).

28. N. M. Hanumegowda, I. M. White, and X. D. Fan, "Aqueous mercuric ion detection with microsphere optical ring resonator sensors," Sensors and Actuators B-Chemical **120**(1), 207-212 (2006).

29. N. M. Hanumegowda, I. M. White, H. Oveys, and X. D. Fan, "Label-free protease sensors based on optical microsphere resonators," Sensor Letters **3**(4), 315-319 (2005).

30. F. Vollmer, S. Arnold, D. Braun, I. Teraoka, and A. Libchaber, "Multiplexed DNA quantification by spectroscopic shift of two microsphere cavities," Biophysical Journal **85**(3), 1974-1979 (2003).

31. F. Vollmer, D. Braun, A. Libchaber, M. Khoshsima, I. Teraoka, and S. Arnold, "Protein detection by optical shift of a resonant microcavity," Applied Physics Letters **80**(21), 4057-4059 (2002).

32. I. M. White, N. M. Hanumegowda, and X. D. Fan, "Subfemtomole detection of small molecules with microsphere sensors," Optics Letters **30**(23), 3189-3191 (2005).

33. H. Y. Zhu, J. D. Suter, I. M. White, and X. D. Fan, "Aptamer based microsphere biosensor for thrombin detection," Sensors **6**(8), 785-795 (2006).

34. A. Francois and M. Himmelhaus, "Optical biosensor based on whispering gallery mode excitations in clusters of microparticles," Applied Physics Letters **92**(14), 141107 (2008).

35. A. Weller, F. C. Liu, R. Dahint, and M. Himmelhaus, "Whispering gallery mode biosensors in the low-Q limit," Applied Physics B-Lasers and Optics **90**(3-4), 561-567 (2008).

36. S. Arnold, M. Khoshsima, I. Teraoka, S. Holler, and F. Vollmer, "Shift of whispering-gallery modes in microspheres by protein adsorption," Optics Letters **28**(4), 272-274 (2003).

37. W. C. W. Chan and S. M. Nie, "Quantum dot bioconjugates for ultrasensitive nonisotopic detection," Science **281**(5385), 2016-2018 (1998).

38. S. Arnold, S. Holler, N. L. Goddard, and G. Griffel, "Cavity-mode selection in spontaneous emission from oriented molecules in a microparticle," Optics Letters **22**(19), 1452-1454 (1997).

39. A. M. Armani, R. P. Kulkarni, S. E. Fraser, R. C. Flagan, and K. J. Vahala, "Label-free, single-molecule detection with optical microcavities," Science **317**(5839), 783-787 (2007).

40. A. M. Armani and K. J. Vahala, "Heavy water detection using ultra-high-Q microcavities," Optics Letters **31**(12), 1896-1898 (2006).

41. C. Y. Chao, W. Fung, and L. J. Guo, "Polymer microring resonators for biochemical sensing applications," IEEE Journal of Selected Topics in Quantum Electronics **12**(1), 134-142 (2006).

42. C. Y. Chao and L. J. Guo, "Biochemical sensors based on polymer microrings with sharp asymmetrical resonance," Applied Physics Letters **83**(8), 1527-1529 (2003).

43. C. Y. Chao and L. J. Guo, "Design and optimization of microring resonators in biochemical sensing applications," Journal of Lightwave Technology **24**(3), 1395-1402 (2006).

44. A. Yalcin, K. C. Popat, J. C. Aldridge, T. A. Desai, J. Hryniewicz, N. Chbouki, B. E. Little, O. King, V. Van, S. Chu, D. Gill, M. Anthes-Washburn, and M. S. Unlu, "Optical sensing of biomolecules using microring resonators," IEEE Journal of Selected Topics in Quantum Electronics **12**(1), 148-155 (2006).

45. A. Ksendzov, M. L. Homer, and A. M. Manfreda, "Integrated optics ring-resonator chemical sensor with polymer transduction layer," Electronics Letters **40**(1), 63-65 (2004).

46. A. Ksendzov and Y. Lin, "Integrated optics ring-resonator sensors for protein detection," Optics Letters **30**(24), 3344-3346 (2005).

47. A. Ramachandran, S. Wang, J. Clarke, S. J. Ja, D. Goad, L. Wald, E. M. Flood, E. Knobbe, J. V. Hryniewicz, S. T. Chu, D. Gill, W. Chen, O. King, and B. E. Little, "A universal biosensing platform based on optical micro-ring resonators," Biosensors & Bioelectronics **23**(7), 939-944 (2008).

48. E. Krioukov, J. Greve, and C. Otto, "Performance of integrated optical microcavities for refractive index and fluorescence sensing," Sensors and Actuators B: Chemical **90**(1-3), 58-67 (2003).

49. R. W. Boyd and J. E. Heebner, "Sensitive disk resonator photonic biosensor," Applied Optics **40**(31), 5742-5747 (2001).

50. S. Blair and Y. Chen, "Resonant-enhanced evanescent-wave fluorescence biosensing with cylindrical optical cavities," Applied Optics **40**(4), 570-582 (2001).

51. I. M. White, H. Oveys, and X. D. Fan, "Liquid-core optical ring-resonator sensors," Optics Letters **31**(9), 1319-1321 (2006).

52. I. M. White, H. Oveys, X. Fan, T. L. Smith, and J. Y. Zhang, "Integrated multiplexed biosensors based on liquid core optical ring resonators and antiresonant reflecting optical waveguides," Applied Physics Letters **89**(19), 191106 (2006).

53. I. M. White, H. Y. Zhu, J. D. Suter, N. M. Hanumegowda, H. Oveys, M. Zourob, and X. D. Fan, "Refractometric sensors for lab-on-a-chip based on optical ring resonators," IEEE Sensors Journal **7**(1-2), 28-35 (2007).

54. H. Y. Zhu, I. M. White, J. D. Suter, P. S. Dale, and X. D. Fan, "Analysis of biomolecule detection with optofluidic ring resonator sensors," Optics Express **15**(15), 9139-9146 (2007).

55. J. D. Suter, I. White, H. Y. Zhu, H. Shi, C. W. Caldwell, and X. Fan, "Label-free quantitative DNA detection using the liquid core optical ring resonator," Biosensors & Bioelectronics **23**, 1003-1009 (2008).

56. H. Y. Zhu, I. M. White, J. D. Suter, M. Zourob, and X. Fan, "Opto-fluidic micro-ring resonator for sensitive label-free viral detection," Analyst **132**, 356-360 (2008).

57. H. Y. Zhu, I. M. White, J. D. Suter, and X. D. Fan, "Phage-based label-free biomolecule detection in an opto-fluidic ring resonator," Biosensors & Bioelectronics **24**(3), 461-466 (2008).

58. Y. Z. Sun and X. D. Fan, "Analysis of ring resonators for chemical vapor sensor development," Optics Express **16**(14), 10254-10268 (2008).

59. Y. Sun, S. I. Shopova, G. Frye-Mason, and X. Fan, "Rapid chemical-vapor sensing using optofluidic ring resonators," Optics Letters **33**, 788-790 (2008).

60. Y. Sun, J. Liu, G. Frye-Mason, S. Ja, A. K. Thompson, and X. Fan, "Optofluidic ring resonator sensors for rapid DNT vapor detection," Analyst **134**, 1386-1391 (2009).

61. I. M. White, J. Gohring, Y. Sun, G. Yang, S. Lacey, and X. Fan, "Versatile waveguide-coupled optofluidic devices based on liquid core optical ring resonators," Applied Physics Letters **91**(24), 241104 (2007).

62. H. Y. Zhu, I. M. White, J. D. Suter, M. Zourob, and X. D. Fan, "Integrated refractive index optical ring resonator detector for capillary electrophoresis," Analytical Chemistry **79**(3), 930-937 (2007).

63. I. M. White, N. M. Hanumegowda, and X. Fan, "Subfemtomole detection of small molecules with microsphere sensors," Opt. Lett. **30**(23), 3189-3191 (2005).

64. M. Noto, M. Khoshsima, D. Keng, I. Teraoka, V. Kolchenko, and S. Arnold, "Molecular weight dependence of a whispering gallery mode biosensor," Applied Physics Letters **87**(22), 223901 (2005).

65. M. Noto, D. Keng, I. Teraoka, and S. Arnold, "Detection of protein orientation on the silica microsphere surface using transverse electric/transverse magnetic whispering gallery modes," Biophysical Journal **92**(12), 4466-4472 (2007).

66. H. C. Ren, F. Vollmer, S. Arnold, and A. Libchaber, "High-Q microsphere biosensor: Analysis for adsorption of rodlike bacteria," Optics Express **15**(25), 17410-17423 (2007).

67. G. Guan, S. Arnold, and M. V. Otugen, "Temperature measurements using a microoptical sensor based on whispering gallery modes," AIAA Journal **44**(10), 2385-2389 (2006).

68. D. Keng, S. R. McAnanama, I. Teraoka, and S. Arnold, "Resonance fluctuations of a whispering gallery mode biosensor by particles undergoing Brownian motion," Applied Physics Letters **91**(10), 103902 (2007).

69. S. Arnold, R. Ramjit, D. Keng, V. Kolchenko, and I. Teraoka, "MicroParticle photophysics illuminates viral bio-sensing," Faraday Discussions **137**, 65-83 (2008).

70. F. Vollmer, S. Arnold, and D. Keng, "Single virus detection from the reactive shift of a whispering-gallery mode," Proceedings of the National Academy of Sciences of the United States of America **105**(52), 20701-20704 (2008).

71. N. M. Hanumegowda, C. J. Stica, B. C. Patel, I. White, and X. D. Fan, "Refractometric sensors based on microsphere resonators," Applied Physics Letters **87**(20), 201107 (2005).

72. I. M. White, N. M. Hanumegowda, H. Oveys, and X. D. Fan, "Tuning whispering gallery modes in optical microspheres with chemical etching," Optics Express **13**(26), 10754-10759 (2005).

73. I. Teraoka, S. Arnold, and F. Vollmer, "Perturbation approach to resonance shifts of whispering-gallery modes in a dielectric microsphere as a probe of a surrounding medium," Journal of the Optical Society of America B-Optical Physics **20**(9), 1937-1946 (2003).

74. I. Teraoka and S. Arnold, "Theory of resonance shifts in TE and TM whispering gallery modes by nonradial perturbations for sensing applications," Journal of the Optical Society of America B-Optical Physics **23**(7), 1381-1389 (2006).

75. I. Teraoka and S. Arnold, "Dielectric property of particles at interface in random sequential adsorption and its application to whispering gallery mode resonance-shift sensors," Journal of Applied Physics **101**(2) 023505-023505-9 (2007).

76. I. Teraoka and S. Arnold, "Estimation of surface density of molecules adsorbed on a whispering gallery mode resonator: Utility of isotropic polarizability," Journal of Applied Physics **102**(7), 3 (2007).

77. I. Teraoka and S. Arnold, "Enhancing the sensitivity of a whispering-gallery mode microsphere sensor by a high-refractive-index surface layer," Journal of the Optical Society of America B-Optical Physics **23**(7), 1434-1441 (2006).

78. I. Teraoka and S. Arnold, "Whispering-gallery modes in a microsphere coated with a high-refractive index layer: Polarization-dependent sensitivity enhancement of the resonance-shift and TE-TM resonance matching," Journal of the Optical Society of America B-Optical Physics **24**(3), 653-659 (2007).

79. O. Gaathon, J. Culic-Viskota, M. Mihnev, I. Teraoka, and S. Arnold, "Enhancing sensitivity of a whispering gallery mode biosensor by subwavelength confinement," Applied Physics Letters **89**(22), 223901 (2006).

80. I. Teraoka and S. Arnold, "Coupled whispering gallery modes in a multilayer-coated microsphere," Optics Letters **32**(9), 1147-1149 (2007).

81. A. Francois and M. Himmelhaus, "Whispering gallery mode biosensor operated in the stimulated emission regime," Applied Physics Letters **94**(3), 031101 (2009).

82. R. E. Benner, P. W. Barber, J. F. Owen, and R. K. Chang, "Observation of structure resonance in the fluorescence-spectra from microspheres," Physical Review Letters **44**(7), 475-478 (1980).

83. M. Kuwata-Gonokami, K. Tekeda, H. Yasuda, and K. Ema, "Laser emission from dye-doped polystyrene microsphere," Japanese Journal of Applied Physics **31**, L99-L101 (1992).

84. P. G. Schiro and A. S. Kwok, "Cavity-enhanced emission from a dye-coated microsphere," Optics Express **12**(13), 2857-2863 (2004).

85. E. Nuhiji and P. Mulvaney, "Detection of unlabeled oligonucleotide targets using whispering gallery modes in single, fluorescent microspheres," Small **3**(8), 1408-1414 (2007).

86. A. P. Alivisatos, "Semiconductor clusters, nanocrystals, and quantum dots," Science **271**(5251), 933-937 (1996).

87. G. W. Bryant and G. S. Solomon, *Optics of Quantum Dots and Wires* (Artech House, Boston, 2005).

88. X. D. Fan, P. Palinginis, S. Lacey, H. L. Wang, and M. C. Lonergan, "Coupling semiconductor nanocrystals to a fused-silica microsphere: A quantum-dot microcavity with extremely high Q factors," Optics Letters **25**(21), 1600-1602 (2000).

89. Y. P. Rakovich, L. Yang, E. M. McCabe, J. F. Donegan, T. Perova, A. Moore, N. Gaponik, and A. Rogach, "Whispering gallery mode emission from a composite system of CdTe nanocrystals and a spherical microcavity," Semiconductor Science and Technology **18**(11), 914-918 (2003).

90. M. Y. Han, X. H. Gao, J. Z. Su, and S. Nie, "Quantum-dot-tagged microbeads for multiplexed optical coding of biomolecules," Nature Biotechnology **19**(7), 631-635 (2001).

91. V. Stsiapura, A. Sukhanova, M. Artemyev, M. Pluot, J. H. M. Cohen, A. V. Baranov, V. Oleinikov, and I. Nabiev, "Functionalized nanocrystal-tagged fluorescent polymer beads: Synthesis, physicochemical characterization, and immunolabeling application," Analytical Biochemistry **334**(2), 257-265 (2004).

92. X. H. Gao and S. M. Nie, "Quantum dot-encoded mesoporous beads with high brightness and uniformity: Rapid readout using flow cytometry," Analytical Chemistry **76**(8), 2406-2410 (2004).

93. M. Bradley, N. Bruno, and B. Vincent, "Distribution of CdSe quantum dots within swollen polystyrene microgel particles using confocal microscopy," Langmuir **21**(7), 2750-2753 (2005).

94. L. M. Zhang, Y. X. Wang, F. J. Zhang, and R. O. Claus, "Observation of whispering-gallery and directional resonant laser emission in ellipsoidal microcavities," Journal of the Optical Society of America B-Optical Physics **23**(9), 1793-1800 (2006).

95. S. Pang, R. E. Beckham, and K. E. Meissner, "Quantum dot-embedded microspheres for remote refractive index sensing," Applied Physics Letters **92**(22), 221108 (2008).

96. G. Mie, "Beitrage zur Optik truber Medien speziell kolloidaler Metallosungen," Ann. Phys. **25**, 377-445 (1908).

97. M. Born and E. Wolf, *Principles of Optics* (Pergamon, New York, 1980).

98. H. C. vandeHulst, *Light Scattering by Small Particles* (Wiley, New York, 1981).

99. C. F. Bohren and D. R. Huffman, *Absorption and scattering of light by small particles*, Wiley Professional Paperback ed., Wiley science paperback series (Wiley, New York, 1998), pp. xiv, 530 p.

100. J. R. Probertjones, "Resonance component of backscattering by large dielectric spheres," Journal of the Optical Society of America A-Optics Image Science and Vision **1**(8), 822-830 (1984).

101. Z. A. Peng and X. G. Peng, "Formation of high-quality CdTe, CdSe, and CdS nanocrystals using CdO as precursor," Journal of the American Chemical Society **123**(1), 183-184 (2001).

102. D. Morrish, X. S. Gan, and M. Gu, "Morphology-dependent resonance induced by two-photon excitation in a micro-sphere trapped by a femtosecond pulsed laser," Optics Express **12**(18), 4198-4202 (2004).

103. C. C. Lam, P. T. Leung, and K. Young, "Explicit asymptotic formulas for the positions, widths, and strengths of resonances in Mie scattering," Journal of the Optical Society of America B-Optical Physics **9**(9), 1585-1592 (1992).

104. H. T. Beier, G. L. Coté, and K. E. Meissner, "Whispering gallery mode biosensors consisting of quantum dot-embedded microspheres," Annals of Biomedical Engineering **37**(10), 1974-1983 (2009).

105. X. Y. Ma, J. Q. Lu, R. S. Brock, K. M. Jacobs, P. Yang, and X. H. Hu, "Determination of complex refractive index of polystyrene microspheres from 370 to 1610 nm," Physics in Medicine and Biology **48**(24), 4165-4172 (2003).

106. K. Suzuki and S. Adachi, "Optical constants of CdxZn1-xSe ternary alloys," Journal of Applied Physics **83**(2), 1018-1022 (1998).

107. X. J. Huang, O. Yarimaga, J. H. Kim, and Y. K. Choi, "Substrate surface roughness-dependent 3-D complex nanoarchitectures of gold particles from directed electrodeposition," Journal of Materials Chemistry **19**(4), 478-483 (2009).

108. T. J. Su, J. R. Lu, R. K. Thomas, and Z. F. Cui, "Effect of pH on the adsorption of bovine serum albumin at the silica water interface studied by neutron reflection," Journal of Physical Chemistry B **103**(18), 3727-3736 (1999).

109. N. J. Freeman, L. L. Peel, M. J. Swann, G. H. Cross, A. Reeves, S. Brand, and J. R. Lu, "Real time, high resolution studies of protein adsorption and structure at the solid-liquid interface using dual polarization interferometry," Journal of Physics: Condensed Matter **16**, S2493-S2496 (2004).

110. J. F. Masson, L. Obando, S. Beaudoin, and K. Booksh, "Sensitive and real-time fiber-optic-based surface plasmon resonance sensors for myoglobin and cardiac troponin I," Talanta **62**(5), 865-870 (2004).

111. A. L. Straface, J. H. Myers, H. J. Kirchick, and K. E. Blick, "A rapid point-of-care cardiac marker testing strategy facilitates the rapid diagnosis and management of chest pain patients in the emergency department," American Journal of Clinical Pathology **129**(5), 788-795 (2008).

112. J. Mair, N. Genser, D. Morandell, J. Maier, P. Mair, P. Lechleitner, C. Calzolari, C. Larue, E. Ambach, F. Dienstl, B. Pau, and B. Puschendorf, "Cardiac troponin I in the diagnosis of myocardial injury and infarction," Clinica Chimica Acta **245**(1), 19-38 (1996).

113. S. Eriksson, S. Wittfooth, and K. Pettersson, "Present and future biochemical markers for detection of acute coronary syndrome," Critical Reviews in Clinical Laboratory Sciences **43**(5-6), 427-495 (2006).

114. E. G. Matveeva, Z. Gryczynski, and J. R. Lakowicz, "Myoglobin immunoassay based on metal particle-enhanced fluorescence," Journal of Immunological Methods **302**(1-2), 26-35 (2005).

115. S. M. Ng, P. Krishnaswamy, R. Morissey, P. Clopton, R. Fitzgerald, and A. S. Maisel, "Ninety-minute accelerated critical pathway for chest pain evaluation," American Journal of Cardiology **88**(6), 611-617 (2001).

116. F. S. Apple, R. H. Christenson, R. Valdes, A. J. Andriak, A. Berg, S. H. Duh, Y. J. Feng, S. A. Jortani, N. A. Johnson, B. Koplen, K. Mascotti, and A. H. B. Wu, "Simultaneous rapid measurement of whole blood myoglobin, creatine kinase MB, and cardiac troponin I by the triage cardiac panel for detection of myocardial infarction," Clinical Chemistry **45**(2), 199-205 (1999).

117. K. F. Buechler, "Near-patient tests: The TRIAGE system," in *The Immunoassay Handbook*, D. Wild, ed. (Elsevier Ltd., Oxford, 2005), pp. 424-430.

118. C. Davies, "Introduction to immunoassay principles," in *The Immunoassay Handbook*, D. Wild, ed. (Elsevier Ltd., Oxford, 2005), pp. 3-40.

119. D. Song and D. Forciniti, "Effects of cosolvents and pH on protein adsorption on polystyrene latex: A dynamic light scattering study," Journal of Colloid and Interface Science **221**(1), 25-37 (2000).

APPENDIX A

Flow Chart for Solving for the Resonance Frequency

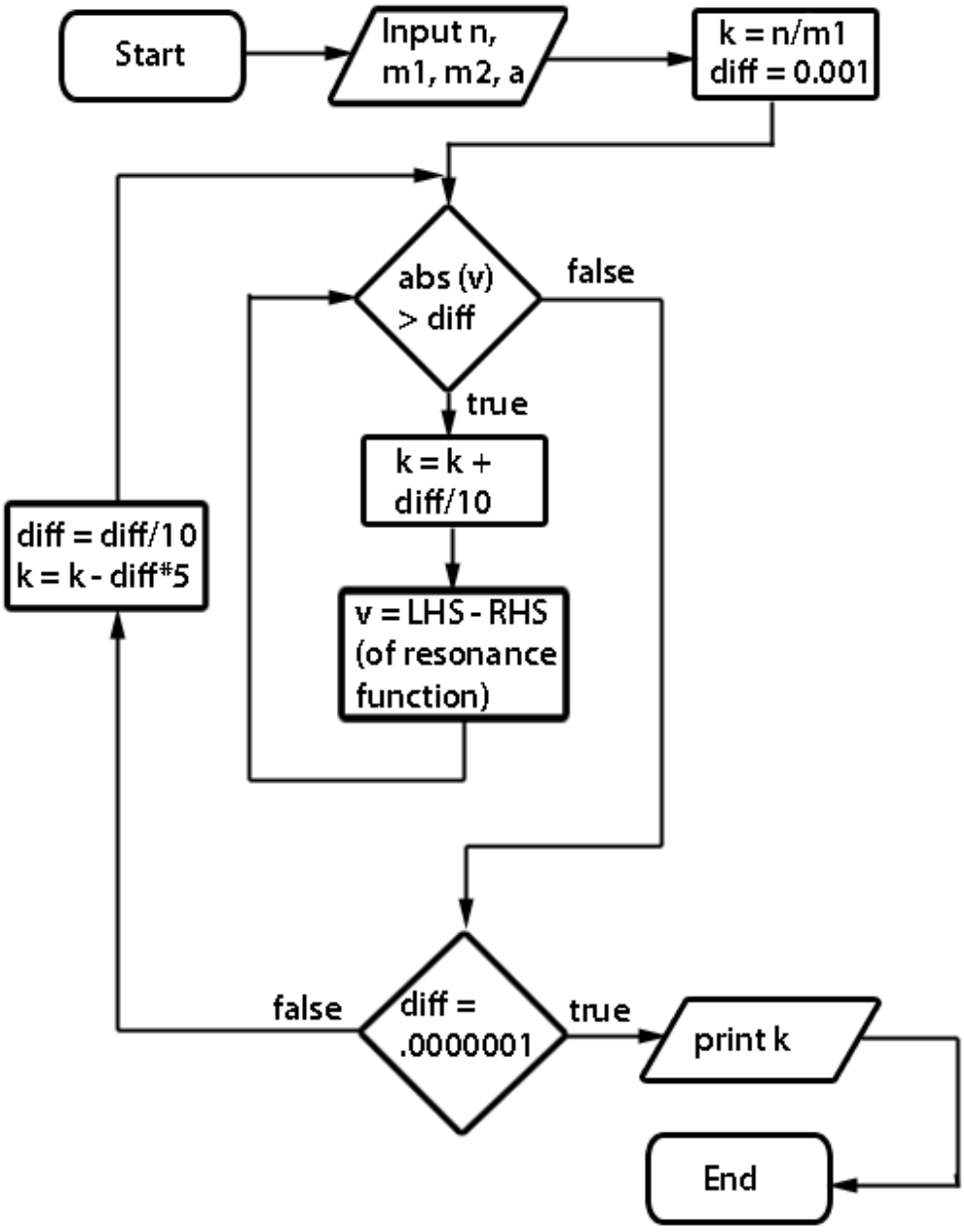

APPENDIX B

Example Changes in WGM Spectra and Sensitivity Due to Variation of Each Parameter

	Resonant Wavelength (TM 80) [nm]	Sensitivity (TM 80) [nm/RIU]	TM–TM Spacing [nm]	TE-TM Spacing [nm]
Increase Microsphere Radius by 0.1 μm	11.46	1.08	0.14	0.10
Increase Microsphere Radius by 0.1 μm and Normalize λ*	N/A	-3.11	-0.17	-0.05
Increase Microsphere Refractive Index by 0.01	2.83	-2.59	0.03	0.13
Increase QD Layer Thickness by 5 nm	0.49	5.87	0.00	-0.34
Increase QD Layer Refractive Index by 0.05	0.90	1.47	0.00	-1.06

* Angular mode number is increased by 2 to normalize the resonance wavelength for the larger microsphere to closer to the original wavelength.

Initial Values:
a = 4.8 μm
m_1 = 1.59
m_2 = 1.333
m_3 = 1.75
t = 40 nm

TM-TM Spacing: TM80 – TM81

TE-TM Spacing: TM80 – TE81

APPENDIX C

```
/* WGMResonanceTM.cpp : Code for solving for the resonance, linewidth, Q-
factor and radial function for a TM mode of a homogenous microsphere.*/

#include "stdafx.h"
#include <iostream>
#include <fstream>
#include <sstream>
#include <string>
#include <math.h>
#include <boost/math/special_functions/bessel.hpp>
#include <vector>

using namespace boost::math;
using namespace std;

//Functions
double xesolver(double, double, double, double, double, int, int, int);
double xupper(double, double, double, double, double, int, int, int);
double xlower(double, double, double, double, double, int, int, int);

int main()
{
        unsigned n;                     //azimuthal number
        double m1, m2;       //index of refraction inside and outside sphere

        cout << "Enter the angular mode number, n (ex. 84) ";
        cin >> n;
        cout << "Enter the refractive index of the sphere (ex. 1.591) ";
        cin >> m1;
        cout << "Enter the refractive index of the solvent (ex. 1.333) ";
        cin >> m2;
        double a;
        cout << "Enter the radius of the sphere (ex. 5) ";
        cin >> a;
        cout << "We'll see if I decide to give you the correct answer.  I'm an evil
        code. ";
        cout << "Results will appear in E-field.txt. " <<endl;

        unsigned nn;
        long double xe;                 //TE size parameter
        long double v;                  //difference value
        int i;                          //iteration counter
```

```
        int j;
        int h;
        double omega=0;

// Initialize variables
        nn=n-1;
        v=100;
        i=1;
        xe=n/m1;
        //xe=62;

/*******************Solve for xe***********************/
        double diff=0.001;
        xe=xesolver(v,xe,diff,m1,m2,n,nn,i);
        xe=xe-.0005;
        diff=0.00001;
        xe=xesolver(v,xe,diff,m1,m2,n,nn,i);
        diff=0.0000001;
        xe=xe-.000005;
        xe=xesolver(v,xe,diff,m1,m2,n,nn,i);

        cout << xe << endl;

/*************Calculate the Line Width******************/
/* First Calculate the point of lower x-value that corresponds to pn=qn*/

        double xl=xe;
        double xu=xe;
        diff=0.00000001;
        double vv=1;

        double xlow=xlower(vv,xu,diff,m1,m2,n,nn,i);
        vv=1;
        double xup=xupper(vv,xu,diff,m1,m2,n,nn,i);

        double wllow=2*3.14159/xlow*a;
        double wlhigh=2*3.14159/xup*a;

        double linewidth=wllow-wlhigh;

/*************Calculate the E-field*****************/

        double astart = .5*a;
        double aend = 1.5*a;
```

```
        int points = 100;  //number of point inside and outside the sphere
        double Rin[101];  //array length is one more than points
        double Rout[101];
        double k = xe/a;
        double Sin[101];
        double Sout[101];
        double sout[101];

//initize Rin and Rout;
        for (j=0; j<points; j++)
        {
                Rin[j]=astart+(a-astart)/(points-1)*j;
                Rout[j]=a+(aend-a)/(points-1)*j;

                double Px=k*m1*Rin[j]*sph_bessel(n,k*m1*Rin[j]);
                Sin[j]=Px;
                double Cx=k*m2*Rout[j]*sph_neumann(n,k*m2*Rout[j]);
                sout[j]=Cx;
        }
        for (h=0; h<points; h++)
        {
                int en=points-1;
                Sout[h]=Sin[en]/sout[0]*sout[h];
        }
/*****************************
******output to a text file****/
        double wl=2*3.14159/xe*a;
        double qf=wl/linewidth;
        cout << "Wavelength = " <<  wl*1000 << endl;
        cout << "Q-factor = " << qf << endl;
        cout << "Linewidth = " << linewidth*1000 << endl;

        ofstream f_out;
        f_out.open("E-field.txt");
        f_out << "n = " << n << endl;
        f_out << "m_sphere = " << m1 << endl;
        f_out << "m_solvent = " << m2 << endl;
        f_out << "Sphere Radius = " << a << endl;
        f_out << "xe = " << xe << endl;
        f_out << "xlow = " << xe-xlow << endl;
        f_out << "xup = " << xe-xup << endl;
        f_out << "wavelength = " << wl << endl;
        f_out << "Line Width = " << linewidth << endl;
        f_out << "Q-factor = " << qf << endl;
```

```
	f_out << "i = " << i << endl;
	f_out << "r"<< "\t";
	f_out << "I" << endl;

	for (j=0;j<points;j++)
	{
		f_out << Rin[j] << "\t";
		f_out << Sin[j] << endl;
	}
	for (j=1;j<points;j++)
	{
		f_out << Rout[j] << "\t";
		f_out << Sout[j] << endl;
	}
		f_out.close();
}



/*************Functions**************************/

double xesolver(double v, double xe, double diff, double m1, double m2, int n, int
nn, int i)
{
	while (abs(v) > diff)
	{
		xe = xe+diff/10;
		long double m1x = m1*xe;
		long double Pmx = m1*xe*sph_bessel(n,m1x);
		long double DPmx = m1*xe*sph_bessel(nn, m1x)-
		n*sph_bessel(n,m1x);
		long double A = 1/m1*DPmx/Pmx;

		long double m2x = m2*xe;
		long double Cmx = m2*xe*sph_neumann(n,m2x);
		long double DCmx = m2*xe*sph_neumann(nn,m2x)-
		n*sph_neumann(n,m2x);
		long double B = 1/m2*DCmx/Cmx;
		v = A-B;
		i=i+1;
	}
	return xe;
};
```

```
double xlower(double vv, double xl, double diff, double m1, double m2, int n, int
nn, int i)
{
	while (abs(vv) > .5)
	{
		xl=xl-diff;
		//double mm=m1/m2;
		double m1x=m1*xl;
		double m2x=m2*xl;
		double Psim2x=m2x*sph_bessel(n,m2x);
		double DPsim2x=m2x*sph_bessel(nn, m2x)-n*sph_bessel(n,m2x);
		double Psim1x=m1x*sph_bessel(n,m1x);
		double DPsim1x=m1x*sph_bessel(nn, m1x)-n*sph_bessel(n,m1x);
		double Chim2x=m2x*sph_neumann(n,m2x);
		double DChim2x=m2x*sph_neumann(nn,m2x)-
		n*sph_neumann(n,m2x);
		double pn=m2*Psim2x*DPsim1x-m1*Psim1x*DPsim2x;
		double qn=m2*Chim2x*DPsim1x-m1*Psim1x*DChim2x;
		vv=pn*pn/(pn*pn+qn*qn);
	}
	return xl;
};

double xupper(double vv, double xu, double diff, double m1, double m2, int n, int
nn, int i)
{
	while (abs(vv) > .5)
	{
		xu=xu+diff;
		double m1x=m1*xu;
		double m2x=m2*xu;
		double Psim2x=m2x*sph_bessel(n,m2x);
		double DPsim2x=m2x*sph_bessel(nn, m2x)-n*sph_bessel(n,m2x);
		double Psim1x=m1x*sph_bessel(n,m1x);
		double DPsim1x=m1x*sph_bessel(nn, m1x)-n*sph_bessel(n,m1x);
		double Chim2x=m2x*sph_neumann(n,m2x);
		double DChim2x=m2x*sph_neumann(nn,m2x)-
		n*sph_neumann(n,m2x);
		double pn=m2*Psim2x*DPsim1x-m1*Psim1x*DPsim2x;
		double qn=m2*Chim2x*DPsim1x-m1*Psim1x*DChim2x;
		vv=pn*pn/(pn*pn+qn*qn);
	}
	return xu;
};
```

APPENDIX D

```
/* WGMResonanceMLTM.cpp : Code for solving for the resonance, linewidth, Q-
factor and radial function for a TM mode of a microsphere with a high index
outer layer.*/


#include "stdafx.h"
#include <iostream>
#include <fstream>
#include <sstream>
#include <string>
#include <math.h>
#include <boost/math/special_functions/bessel.hpp>
#include <vector>

using namespace boost::math;
using namespace std;

//Functions
double kesolver(double, double, double, double, double, double, double, double,
int, int, int);

int main()
{
	unsigned n;			//azimuthal number
	double m1, m2, m3; //index of refraction inside and outside sphere
	cout << "Enter the angular mode number, n (ex. 80) ";
	cin >> n;
	cout << "Enter the refractive index of the sphere (ex. 1.587) ";
	cin >> m1;
	cout << "Enter the refractive index of the solvent (ex. 1.333) ";
	cin >> m2;
	cout << "Enter the refractive index of the layer (ex 1.8) ";
	cin >> m3;
	double a;
	cout << "Enter the radius of the sphere (ex. 4.8) ";
	cin >> a;
	double t;
	cout << "Enter the thickness of the layer (ex .02) ";
	cin >> t;
	cout << "Results will appear in E-field.txt. " <<endl;
	cout << "We'll see if I decide to give you the correct answer.  I'm an evil
	code. ";
```

```
        unsigned nn;
        //long double xe;               //TE size parameter
        long double ke;
        long double v;                  //difference value
        int i;                  //iteration counter
        int j;
        int h;


        // Initialize variables
        nn=n-1;
        v=100;
        i=1;
        ke=n/m1/a-2;

/*******************Solved for xe************************/
        double diff=0.01;
        ke=kesolver(v,ke,diff,m1,m2,m3,t,a,n,nn,i);
        v=100;
        ke=ke-.005;
        diff=0.001;
        ke=kesolver(v,ke,diff,m1,m2,m3,t,a,n,nn,i);
        v=100;
        ke=ke-.0005;
        diff=0.0001;
        ke=kesolver(v,ke,diff,m1,m2,m3,t,a,n,nn,i);
        v=100;
        ke=ke-.00005;
        diff=0.00001;
        ke=kesolver(v,ke,diff,m1,m2,m3,t,a,n,nn,i);
        v=100;
        ke=ke-.000005;
        diff=0.000001;
        ke=kesolver(v,ke,diff,m1,m2,m3,t,a,n,nn,i);

        long double z1 = m1*ke*(a-t);
        long double z3 = m3*ke*(a-t);
        long double Pz1 = z1*sph_bessel(n,z1);
        long double Cz3 = z3*sph_neumann(n,z3);
        long double Pz3 = z3*sph_bessel(n,z3);
        long double DPz1 = z1*sph_bessel(nn,z1)-n*Pz1/z1;
        long double DCz3 = z3*sph_neumann(nn,z3)-n*Cz3/z3;
        long double DPz3 = z3*sph_bessel(nn,z3)-n*Pz3/z3;
```

```
        long double C = m1*Pz1*DCz3 - m3*DPz1*Cz3;
        long double D = -m1*Pz1*DPz3 + m3*DPz1*Pz3;
        long double CD = C/D;

        long double m2x = m2*ke*a;
        long double m3x = m3*ke*a;
        long double Cm2 = m2x*sph_neumann(n,m2x);
        long double DCm2 = m2x*sph_neumann(nn,m2x)-n*Cm2/m2x;
        long double Left = m3/m2*DCm2/Cm2;

        long double Pm3 = m3x*sph_bessel(n,m3x);
        long double DPm3 = m3x*sph_bessel(nn,m3x)-n*Pm3/m3x;
        long double Cm3 = m3x*sph_neumann(n,m3x);
        long double DCm3 = m3x*sph_neumann(nn,m3x)-n*Cm3/m3x;

        long double RN = CD*DPm3+DCm3;
        long double RD = CD*Pm3+Cm3;
        long double Right = RN/RD;


        double lambda=2*3.14159/ke*1000;

        cout << lambda << endl;

/****************end of ke solve*********************/
        double astart = .5*a;
        double aend = 1.5*a;
        int points = 100;  //number of point inside and outside the sphere
        int laypoints = points/10;
        double Rin[101];  //array length is one more than points
        double Rout[101];
        double Rlay[101];
        double Sin[101];
        double Sout[101];
        double Slay[101];
        double sout[101];
        double sin[101];

        for (j=0; j<points; j++)
        {
                Rin[j]=0;
                Rout[j]=0;
                Rlay[j]=0;
                Sout[j]=0;
```

```
                Sin[j]=0;
                Slay[j]=0;
                sout[j]=0;
                sin[j]=0;
        }

//initize Rin and Rout;
        for (j=0; j<points; j++)
        {
                Rin[j]=astart+((a-t)-astart)/(points-1)*j;
                Rout[j]=a+(aend-a)/(points-1)*j;
                double Px=ke*m1*Rin[j]*sph_bessel(n,ke*m1*Rin[j]);
                sin[j]=Px;
                double Cx=ke*m2*Rout[j]*sph_neumann(n,ke*m2*Rout[j]);
                sout[j]=Cx;
        }

        for (h=0; h<laypoints; h++)
        {
                Rlay[h]=(a-t)+ t/(laypoints-1)*h;
                double L1 = C*m3*ke*Rlay[h]*sph_bessel(n,m3*ke*Rlay[h]);
                double L2 = D*m3*ke*Rlay[h]*sph_neumann(n,m3*ke*Rlay[h]);
                Slay[h]=L1+L2;
        }

        for (j=0; j<points; j++)
        {
                int en=points-1;
                int en2=laypoints-1;
                Sout[j]=Slay[en2]/sout[0]*sout[j];
                Sin[j]=Slay[0]/sin[en]*sin[j];
        }

/*******************************
******output to a text file****/

        ofstream f_out;
        f_out.open("E-field.txt");
        f_out << "n = " << n << endl;
        f_out << "m_sphere = " << m1 << endl;
        f_out << "m_solvent = " << m2 << endl;
        f_out << "m_qd-layer = " << m3 << endl;
        f_out << "Sphere Radius = " << a << endl;
        f_out << "Layer Thickness = " << t << endl;
```

```
	f_out << "Difference = " << v << endl;
	f_out << "ke = " << ke << endl;
	f_out << "i = " << i << endl;
	f_out << "r"<< "\t";
	f_out << "I" << endl;

	for (j=0;j<points;j++)
	{
		f_out << Rin[j] << "\t";
		f_out << Sin[j] << endl;
	}

	for (h=1;h<laypoints;h++)
	{
		f_out << Rlay[h] << "\t";
		f_out << Slay[h] << endl;
	}

	for (j=1;j<points;j++)
	{
		f_out << Rout[j] << "\t";
		f_out << Sout[j] << endl;
	}

	f_out.close();
}

double kesolver(double v, double ke, double diff, double m1, double m2, double
m3, double t, double a, int n, int nn, int i)
{
	while (abs(v) > diff && ke<15)
		{   ke = ke+diff/10;
		double vv=v;
		long double z1 = m1*ke*(a-t);
		long double z3 = m3*ke*(a-t);
		long double Pz1 = z1*sph_bessel(n,z1);
		long double Cz3 = z3*sph_neumann(n,z3);
		long double Pz3 = z3*sph_bessel(n,z3);
		long double DPz1 = z1*sph_bessel(nn,z1)-n*Pz1/z1;
		long double DCz3 = z3*sph_neumann(nn,z3)-n*Cz3/z3;
		long double DPz3 = z3*sph_bessel(nn,z3)-n*Pz3/z3;

		long double C = m1*Pz1*DCz3 - m3*DPz1*Cz3;
		long double D = -m1*Pz1*DPz3 + m3*DPz1*Pz3;
```

```
                long double CD = C/D;

                long double m2x = m2*ke*a;
                long double m3x = m3*ke*a;
                long double Cm2 = m2x*sph_neumann(n,m2x);
                long double DCm2 = m2x*sph_neumann(nn,m2x)-n*Cm2/m2x;
                long double Left = m3/m2*DCm2/Cm2;

                long double Pm3 = m3x*sph_bessel(n,m3x);
                long double DPm3 = m3x*sph_bessel(nn,m3x)-n*Pm3/m3x;
                long double Cm3 = m3x*sph_neumann(n,m3x);
                long double DCm3 = m3x*sph_neumann(nn,m3x)-n*Cm3/m3x;

                long double RN = CD*DPm3+DCm3;
                long double RD = CD*Pm3+Cm3;
                long double Right = RN/RD;

                v = Right-Left;
                i=i+1;

                if (abs(v)>abs(vv))
                {
                        ke=14;
                }
        }
        return ke;
};
```

APPENDIX E

```
/* SingleQDLayerTM_var.cpp : Code for simultaneously solving for TM mode
resonances as a function of multiple parameters for a microsphere with a high
index outer layer.*/

#include "stdafx.h"
#include <iostream>
#include <fstream>
#include <sstream>
#include <string>
#include <math.h>
#include <boost/math/special_functions/bessel.hpp>
#include <vector>

using namespace boost::math;
using namespace std;

//Functions
double kesolver(double, double, double, double, double, double, double, double,
int, int, int);


int main()
{
	//unsigned n;			//azimuthal number
	double m1, m2;		//index of refraction inside and outside sphere
	double a;
	//unsigned nn;
	long double ke;
	long double v;			//difference value
	int i;			//iteration counter

	//initilize usual variables

	double pi=3.14159265;
	int T=2; //number of layers
	double t;

//Arrays for the possible parameters
	double A[15];
	double NQD[15];
	double TL[15];
	double MM[15];
```

```
//Output Arrays
	long double KE[15][15][15];
	double Lambda[15][15][15];

//Number of Possibilities for Each Parameter
	int hh=15;
	int qq=1;
	int mm=7;

//Initialize the Output Arrays
	for (int m=0; m<mm; m++)
	{
		for (int h=0; h<hh; h++)
		{
			for (int q=0; q<qq; q++)
			{
				KE[q][h][m]=0;
				Lambda[q][h][m]=0;
			}
		}
	}

//Initialize the Various Parameters
	for (int h=0; h<hh; h++)
	{
		TL[h]=.005+.005*h;
		for (int q=0; q<qq; q++)
		 {
			NQD[q]=79;
		}
	}

	for (int m=0; m<mm; m++)
	{
		MM[m]=1.7+.05*m;
	}

//Alternative Parameters
	/*for (int q=0; q<qq; q++)
	{
		NQD[q]=90+q;
		//A[q]=4.4+.1*q;
	}
```

```
	/*MM[0]=1.85;
	TL[0]=.0134;
	MM[1]=1.75;
	MM[2]=1.8;
	MM[3]=1.85;
	MM[4]=1.9;
	TL[0]=.0415;
	TL[1]=.0142;
	TL[2]=.0103;
	TL[3]=.0078;
	TL[4]=.0062;*/

	// Initialize Constants
	m1=1.587;
	//t=.02;
	double m3;
	a=4.8;
	int n;
	int nn;
/*******************Solve for xe************************/
	// Initialize variables for each run
	for (int m=0; m<mm; m++)
	{
		m3=MM[m];

		for (int h=0; h<hh; h++)
		{
			t=TL[h];
			//m3=MM[h];
			for (int q=0; q<qq; q++)
			{
				n=NQD[q];
				nn=n-1;
				m2=1.333;
				v=100;
				i=1;
				ke=n/m1/a-6;

		// Call functions to determine ke
				double diff=0.01;
				ke=kesolver(v,ke,diff,m1,m2,m3,t,a,n,nn,i);
				v=100;
				ke=ke-.005;
```

```
                                diff=0.001;
                                ke=kesolver(v,ke,diff,m1,m2,m3,t,a,n,nn,i);
                                v=100;
                                ke=ke-.0005;
                                diff=0.0001;
                                ke=kesolver(v,ke,diff,m1,m2,m3,t,a,n,nn,i);
                                v=100;
                                ke=ke-.00005;
                                diff=0.00001;
                                ke=kesolver(v,ke,diff,m1,m2,m3,t,a,n,nn,i);
                                v=100;
                                ke=ke-.000005;
                                diff=0.000001;
                                ke=kesolver(v,ke,diff,m1,m2,m3,t,a,n,nn,i);

                                KE[q][h][m]=ke;
                                Lambda[q][h][m]=2*pi/ke*1000;

                        // Output to Indicate Progress
                                cout << m3 << "\t";
                                cout <<  t << "\t";
                                cout << n << endl;
                        }
                }
        }

//************************Output to a Text File******************
        ofstream f_out;
        f_out.open("tm79resonances.txt");
        f_out << "m_sphere = " << m1 << endl;
        f_out << "m_solvent = " << m2 << endl;
        f_out << "Thickness = " << t << endl;
        //f_out << "Sphere Radius = " << a << endl;
        //f_out << "n = " << n << endl;
        f_out << "N =" << "\t";
        f_out << "ke =" << endl;
        for (int q=0;q<qq;q++)
        {
                for (int h=0;h<hh;h++)
                {
                        f_out << TL[h] << "\t";

                        for (int m=0;m<mm;m++)
                        {
```

```
                        f_out << Lambda[q][h][m] << "\t";
                    }

                    f_out << endl;
                }
            }
            f_out.close();
}

//******************Function to solve for ke**************************************
double kesolver(double v, double ke, double diff, double m1, double m2, double
m3, double t, double a, int n, int nn, int i)
{
        while (abs(v) > diff && ke<15)
        {
                ke = ke+diff/10;
                double vv=v;
                long double z1 = m1*ke*(a-t);
                long double z3 = m3*ke*(a-t);
                long double Pz1 = z1*sph_bessel(n,z1);
                long double Cz3 = z3*sph_neumann(n,z3);
                long double Pz3 = z3*sph_bessel(n,z3);
                long double DPz1 = z1*sph_bessel(nn,z1)-n*Pz1/z1;
                long double DCz3 = z3*sph_neumann(nn,z3)-n*Cz3/z3;
                long double DPz3 = z3*sph_bessel(nn,z3)-n*Pz3/z3;

                long double C = m1*Pz1*DCz3 - m3*DPz1*Cz3;
                long double D = -m1*Pz1*DPz3 + m3*DPz1*Pz3;
                long double CD = C/D;

                long double m2x = m2*ke*a;
                long double m3x = m3*ke*a;
                long double Cm2 = m2x*sph_neumann(n,m2x);
                long double DCm2 = m2x*sph_neumann(nn,m2x)-n*Cm2/m2x;
                long double Left = m3/m2*DCm2/Cm2;

                long double Pm3 = m3x*sph_bessel(n,m3x);
                long double DPm3 = m3x*sph_bessel(nn,m3x)-n*Pm3/m3x;
                long double Cm3 = m3x*sph_neumann(n,m3x);
                long double DCm3 = m3x*sph_neumann(nn,m3x)-n*Cm3/m3x;

                long double RN = CD*DPm3+DCm3;
                long double RD = CD*Pm3+Cm3;
                long double Right = RN/RD;
```

```
                v = Right-Left;
                i=i+1;

                if (abs(v)>abs(vv))
                {
                        ke=14;
                }
        }
        return ke;
};
```

APPENDIX F

```
/* TwoLayersTE.cpp : Code for solving for TE mode resonances for a
microsphere with two outer layers.*/


#include "stdafx.h"
#include <iostream>
#include <fstream>
#include <sstream>
#include <string>
#include <math.h>
#include <boost/math/special_functions/bessel.hpp>
#include <vector>

using namespace boost::math;
using namespace std;

//Functions
double kesolver(double, double, double, double, double, double, double, double,
double, double, int, int, int);

int main()
{
	unsigned n;			//azimuthal number
	double m1, m2;		//index of refraction inside and outside sphere
	double a;
	unsigned nn;
	long double ke;
	long double v;			//difference value
	int i;			//iteration counter

	//initilize usual variables
	n=95;
	nn=n-1;
	double pi=3.14159265;
	m1=1.587;
	double ml1=1.8;
	m2=1.335;

	int T=2; //number of layers
	double m3=1.376; //RI of QD Layer
	double tL=.02; //thickness of the outmost layer
	double t=.04+tL; //thickness of all the layers
```

```
        a=5.5+tL; //radius of the microsphere plus the protein layer

/*******************Solve for xe************************/

        // Initialize variables
        v=100;
        i=1;
        ke=n/m1/a;

        double diff=0.01;
        ke=kesolver(v,ke,diff,m1,m2,m3,ml1,t,tL,a,n,nn,i);

        ke=ke-.005;
        diff=0.0001;
        ke=kesolver(v,ke,diff,m1,m2,m3,ml1,t,tL,a,n,nn,i);

        ke=ke-.00005;
        diff=0.000001;
        ke=kesolver(v,ke,diff,m1,m2,m3,ml1,t,tL,a,n,nn,i);

        ke=ke-.0000005;
        diff=0.00000001;
        ke=kesolver(v,ke,diff,m1,m2,m3,ml1,t,tL,a,n,nn,i);

        //initialize the coefficients
        double C[10];
        double D[10];
        C[0]=0;
        C[1]=0;
        D[0]=0;
        D[1]=0;

        //solve for the coefficients of the inner layer
        long double z1a = m1*ke*(a-t);
        long double z3a = ml1*ke*(a-t);
        long double Pz1a = z1a*sph_bessel(n,z1a);
        long double Cz3a = z3a*sph_neumann(n,z3a);
        long double Pz3a = z3a*sph_bessel(n,z3a);
        long double DPz1a = z1a*sph_bessel(nn,z1a)-n*Pz1a/z1a;
        long double DCz3a = z3a*sph_neumann(nn,z3a)-n*Cz3a/z3a;
        long double DPz3a = z3a*sph_bessel(nn,z3a)-n*Pz3a/z3a;

        C[0] = ml1*Pz1a*DCz3a - m1*DPz1a*Cz3a;
        D[0] = -ml1*Pz1a*DPz3a + m1*DPz1a*Pz3a;
```

```
        //solve for the coefficients of the other layers
        for (int L=1;L<2;L++)
        {
                int LL=L-1;
                double mL=m3;
                double mLL=ml1;

                long double zL=(mL*ke*(a-tL));
                long double zLL=(mLL*ke*(a-tL));

                long double PzL=zL*sph_bessel(n,zL);
                long double PzLL=zLL*sph_bessel(n,zLL);
                long double CzL=zL*sph_neumann(n,zL);
                long double CzLL=zLL*sph_neumann(n,zLL);
                long double DPzL=zL*sph_bessel(nn,zL)-n*PzL/zL;
                long double DPzLL=zLL*sph_bessel(nn,zLL)-n*PzLL/zLL;
                long double DCzL=zL*sph_neumann(nn,zL)-n*CzL/zL;
                long double DCzLL=zLL*sph_neumann(nn,zLL)-n*CzLL/zLL;

                C[L]=mL*DCzL*(C[LL]*PzLL+D[LL]*CzLL)-
                mLL*CzL*(C[LL]*DPzLL+D[LL]*DCzLL);
                D[L]=mLL*PzL*(C[LL]*DPzLL+D[LL]*DCzLL)-
                mL*DPzL*(C[LL]*PzLL+D[LL]*CzLL);

        }

        double wl=2*3.14159/ke*1000;
        cout <<  m3 << "\t" << ke << endl;
        cout << wl << endl;

/***************end of ke solve*********************/
        double astart = .5*a;
        double aend = 1.5*a;
        int points = 100;  //number of point inside and outside the sphere
        int laypoints = points/10;
        double Rin[101];  //array length is one more than points
        double Rout[101];
        double Rlayer[101][10];
        double Sin[101];
        double Sout[101];
        double Slayer[101][10];
        double sout[101];
        double sin[101];
```

```
	double slayer[101][10];

	for (int L=0; L<T; L++)
	{
		for (int j=0; j<points; j++)
		{
			Rin[j]=0;
			Rout[j]=0;
			Rlayer[j][L]=0;
			Sout[j]=0;
			Sin[j]=0;
			Slayer[j][L]=0;
			sout[j]=0;
			sin[j]=0;
			slayer[j][L]=0;
		}
	}

//initize Rin and Rout;
	for (int j=0; j<points; j++)
	{
		Rin[j]=astart+((a-t)-astart)/(points-1)*j;
		Rout[j]=a+(aend-a)/(points-1)*j;
		double Px=ke*m1*Rin[j]*sph_bessel(n,ke*m1*Rin[j]);
		sin[j]=Px;
		double Cx=ke*m2*Rout[j]*sph_neumann(n,ke*m2*Rout[j]);
		sout[j]=Cx;
	}

	double tlay;
	for (int h=0; h<laypoints; h++)
	{
		tlay=t-tL;
		Rlayer[h][0]=(a-t) + tlay/((double)laypoints-1)*(double)h;
		Rlayer[h][1]=(a-tL)+tL/(laypoints-1)*h;
	}

		double NL[2];
		NL[0]=ml1;
		NL[1]=m3;

	for (int L=0; L<T; L++)
	{
		for (int h=0; h<laypoints; h++)
```

```
                {
                        double Part1 = C[L]*NL[L]*ke*Rlayer[h][L]
                        *sph_bessel(n,NL[L]*ke*Rlayer[h][L]);
                        double Part2 = D[L]*NL[L]*ke*Rlayer[h][L]
                        *sph_neumann(n,NL[L]*ke*Rlayer[h][L]);
                        slayer[h][L]=Part1 + Part2;
                }
        }

        for (int j=0; j<points; j++)
        {
                int en=points-1;
                Sin[j]=slayer[0][0]/sin[en]*sin[j];
        }

        for (int k=0; k<laypoints;k++)
        {
                Slayer[k][0]=slayer[k][0];
        }

        for(int L=1;L<T;L++)
        {
                for (int k=0; k<laypoints; k++)
                {
                        int en2=laypoints-1;
                        int Lk=L-1;
                        Slayer[k][L]=Slayer[9][Lk]/slayer[0][L]*slayer[k][L];
                }
        }

        for (int j=0; j<points; j++)
        {
                Sout[j]=Slayer[9][T-1]/sout[0]*sout[j];
        }
/*****************************
******output to a text file****/

        ofstream f_out;
        f_out.open("ProteinLayer.txt");
        f_out << "n = " << n << endl;
        f_out << "m_sphere = " << m1 << endl;
        f_out << "m_solvent = " << m2 << endl;
        f_out << "Sphere Radius = " << a << endl;
        f_out << "Layer Thickness = " << t << endl;
```

```
	f_out << "Difference = " << v << endl;
	f_out << "ke = " << ke << endl;
	f_out << "i = " << i << endl;
	f_out << "r"<< "\t";
	f_out << "I" << endl;

	for (int j=0;j<points;j++)
	{
		f_out << Rin[j] << "\t";
		f_out << Sin[j] << endl;
	}


	for (int L=0;L<T;L++)
	{
		for (int h=0;h<laypoints;h++)
		{
			f_out << Rlayer[h][L] << "\t";
			f_out << Slayer[h][L] << endl;
		}
	}

	for (int j=0;j<points;j++)
	{
		f_out << Rout[j] << "\t";
		f_out << Sout[j] << endl;
	}

	f_out.close();
}

//******************Function to solve for
Ke*********************************************
double kesolver(double v, double ke, double diff, double m1, double m2, double
m3, double ml1, double t, double tL, double a, int n, int nn, int i)
{
	while (v > diff && ke<13)
	{
		ke = ke+diff/10;

		double C[10];
		double D[10];
		C[0]=0;
		C[1]=0;
```

```
        D[0]=0;
        D[1]=0;

        //solve for the coefficients of the inner layer
        long double z1a = m1*ke*(a-t);
        long double z3a = ml1*ke*(a-t);
        long double Pz1a = z1a*sph_bessel(n,z1a);
        long double Cz3a = z3a*sph_neumann(n,z3a);
        long double Pz3a = z3a*sph_bessel(n,z3a);
        long double DPz1a = z1a*sph_bessel(nn,z1a)-n*Pz1a/z1a;
        long double DCz3a = z3a*sph_neumann(nn,z3a)-n*Cz3a/z3a;
        long double DPz3a = z3a*sph_bessel(nn,z3a)-n*Pz3a/z3a;

        C[0] = ml1*Pz1a*DCz3a - m1*DPz1a*Cz3a;
        D[0] = -ml1*Pz1a*DPz3a + m1*DPz1a*Pz3a;

//solve for the coefficients of the other layers
        for (int L=1;L<2;L++)
        {
                int LL=L-1;
                double mL=m3;
                double mLL=ml1;

                long double zL=(mL*ke*(a-tL));
                long double zLL=(mLL*ke*(a-tL));

                long double PzL=zL*sph_bessel(n,zL);
                long double PzLL=zLL*sph_bessel(n,zLL);
                long double CzL=zL*sph_neumann(n,zL);
                long double CzLL=zLL*sph_neumann(n,zLL);
                long double DPzL=zL*sph_bessel(nn,zL)-n*PzL/zL;
                long double DPzLL=zLL*sph_bessel(nn,zLL)-n*PzLL/zLL;
                long double DCzL=zL*sph_neumann(nn,zL)-n*CzL/zL;
                long double DCzLL=zLL*sph_neumann(nn,zLL)-
                n*CzLL/zLL;

                C[L]=mL*DCzL*(C[LL]*PzLL+D[LL]*CzLL)-
                mLL*CzL*(C[LL]*DPzLL+D[LL]*DCzLL);
                D[L]=mLL*PzL*(C[LL]*DPzLL+D[LL]*DCzLL)-
                mL*DPzL*(C[LL]*PzLL+D[LL]*CzLL);
        }

//use the coefficients to solve for the resonance condition;
```

```
                int EL=2-1;
                long double CDend=C[EL]/D[EL];
                long double m2x = m2*ke*a;
                long double m3x = m3*ke*a;
                long double Cm2 = m2x*sph_neumann(n,m2x);
                long double DCm2 = m2x*sph_neumann(nn,m2x)-n*Cm2/m2x;
                long double Left = m2/m3*DCm2/Cm2;

                long double Pm3 = m3x*sph_bessel(n,m3x);
                long double DPm3 = m3x*sph_bessel(nn,m3x)-n*Pm3/m3x;
                long double Cm3 = m3x*sph_neumann(n,m3x);
                long double DCm3 = m3x*sph_neumann(nn,m3x)-n*Cm3/m3x;

                long double RN = CDend*DPm3+DCm3;
                long double RD = CDend*Pm3+Cm3;
                long double Right = RN/RD;

                v = Right-Left;
                i=i+1;
                if (v<0)
                {
                        ke=14;
                }
        }
        return ke;
};
```

APPENDIX G

Matlab Peak Solver Functions

1200 g/mm grating

```
function [Peak,PeakI,PeakWL] = peaks(Data,WL,n,shift)

lim=.5;
m=1;
for m = 1:n
        i=1; j=1; k=19;

        for j = 1:50
                 p = j*20+shift;
                M=mean(Data(p:p+k,m));
                [P,PI]=max(Data(p:p+k,m));
                Q=max(Data(p-k:p+k+k,m));

                if P==Q,
                        if P>lim*M
                                Peak(i,m)=P;
                                PeakI(i,m)=PI+p-1;
                                PeakWL(i,m)=WL(PI+p-1,1);
                                i=i+1;
                        end
                end
        end
end
```

2400 g/mm grating

```
function [Peak,PeakI,PeakWL] = peaks(Data,WL,n,shift)

lim=.95;
m=1;
for m = 1:n
        i=1; j=1; k=48;

        for j = 1:22
                p = j*50+shift;
                M=mean(Data(p:p+k,m));
                [P,PI]=max(Data(p:p+k,m));
                Q=max(Data(p-k:p+k+k,m));
```

```
                if P==Q,
                        if P>lim*M
                                Peak(i,m)=P;
                                PeakI(i,m)=PI+p-1;
                                PeakWL(i,m)=WL(PI+p-1,1);
                                i=i+1;
                        end
                end
        end
end
```

VITA

Name: Hope Thomas Beier

Address: 337 Zachry Engineering Center
3120 TAMU
College Station, TX 77843-3120

Email Address: hopebeier@gmail.com

Education: B.S. in Biomedical Engineering, Texas A&M University, 2004
Ph.D in Biomedical Engineering, Texas A&M University, 2009